PREDICTION OF THE PROLIFERATION CAPACITY OF ADIPOSE-DERIVED STROMAL CELLS *IN VITRO*

by

Karel Jacobus Frederik de Bruin

Submitted in partial fulfilment of the requirements for the degree
Master of Engineering (Computer Engineering)

in the

Department of Electrical, Electronic and Computer Engineering
Faculty of Engineering, Built Environment and Information Technology

UNIVERSITY OF PRETORIA

September 2018

SUMMARY

PREDICTION OF THE PROLIFERATION CAPACITY OF ADIPOSE-DERIVED STROMAL CELLS *IN VITRO*

by

Karel Jacobus Frederik de Bruin

Supervisor:	Prof. J.P. de Villiers
Co-supervisor:	Prof. M.S. Pepper
Department:	Electrical, Electronic and Computer Engineering
University:	University of Pretoria
Degree:	Master of Engineering (Computer Engineering)
Keywords:	adipose-derived stromal/stem cells, mathematical modelling, cellular automata

In this study, the proliferation of adipose-derived stromal cells was modelled and compared to experimental measurements. The fundamental characteristics of contact-inhibited proliferation were investigated by implementing a reductionist cellular automata model that assumed space-constraints as the only limiting factor of proliferation. The cellular automata were measured in terms of confluency and their mitotic fraction, which meant that the influence of various factors could be investigated independently of the cell count and simulated matrix size. The seeded confluency and the migration of cells were found to have important effects on the mitotic fraction, and it was discovered that this effect could be summarised by calculating a measure of spatial dispersion. While the cellular automata model is based on previously published models, the relationship that was discovered between the mitotic fraction, confluency and spatial dispersion is new.

A Markov population model that describes the number of cells as a function of cell cycles and the mitotic fraction was derived from first-principles. A population model with a time or cycle varying mitotic fraction has not previously been formally described in the literature. Two models for the variable mitotic fraction were derived from two well-known population equations: the Verhulst and generalised logistic equations. The Verhulst model provided reasonable approximations for the cellular automata simulations, but could not accurately describe very low or high seeding densities. The generalised logistic model included parameters that had no previously defined biological meaning. A relationship between spatial dispersion and the undefined parameters was discovered, and by including a measure of spatial dispersion, the generalised logistic model more accurately described the cellular automata simulations than the Verhulst model. The relationship between the undefined parameters in the generalised logistic model and confluency and spatial dispersion has not been previously described in the literature.

The population model was converted to a function of time to allow comparison to experimental measurements. The Verhulst and generalised logistic mitotic fraction models performed similarly when describing and predicting the experimental data, and no statistically significant difference was found between the root-mean-square error of each model. This could either indicate that spatial dispersion is not a causal predictor of adipose-derived stromal/stem cell (ASC) proliferation *in vitro*, or that the comparatively low spatial dispersion that was measured had a minimal effect on proliferation.

Cells from the same patient that were seeded at different densities were found to have different population limits. Confluency was quantified for the lower population limit, and it was found that a plateau was reached at less than 60% confluency. This indicates that space constraints may not the only limiting factor of proliferation, and that other factors, such as cell-to-cell interactions, may influence the proliferation of ASCs.

The population models were tested for their predictive capacity, but it was found that accurate estimates of the population limit required the inclusion of measurements of slowing growth. When considering that slowing growth usually occurs when a population approaches confluency, this limits the predictive utility of the models in a clinical setting.

LIST OF ABBREVIATIONS

ASC	adipose-derived stromal/stem cell
CO_2	carbon dioxide
CSFE	carboxyfluorescein succinimidyl ester
G0	gap 0
G1	gap 1
G2	gap 2
DAPI	4', 6-diamidino-2-phenylindole
DNA	deoxyribonucleic acid
DT	division time
FBS	foetal bovine serum
HEPES	4-(2-hydroxyethyl)-1-piperazineethanesulfonic acid
HSC	hematopoietic stem cell
IFATS	International Federation for Adipose Therapeutics and Science
ISCT	International Society for Cellular Therapy
M	mitosis
MSC	mesenchymal stem cell
pHPL	pooled human platelet lysate
PDT	population doubling time
PLA	processed lipoaspirate
RMSE	root-mean-square error
S	synthesis
SANBS	South African National Blood Service
SVF	stromal vascular fraction

TABLE OF CONTENTS

CHAPTER 1 INTRODUCTION

1.1 PROBLEM STATEMENT

1.1.1 Context of the problem

The United States Food and Drug Administration announced a regenerative medicine policy framework in 2017, and it stated that "We're at the beginning of a paradigm change in medicine with the promise of being able to facilitate regeneration of parts of the human body, where cells and tissues can be engineered … and adult stem cells can generate replacements for cells that are lost to injury or disease" [1].

Adipose tissue is a source of two important cell populations used in regenerative medicine: stromal vascular fraction (SVF) cells that are isolated from adipose tissue via collagenase digestion, and adipose-derived stromal/stem cells (ASCs), a plastic-adherent population that is isolated by culturing the SVF.

ASCs contain a sub-population of adult stem-like cells that have promising applications in cell-based therapy and regenerative medicine, and may be expanded to greater numbers *in vitro*, before use in treatments. There is substantial inter- and intra-patient variability in the *in vitro* proliferation characteristics of ASCs, which is likely to be due in part to the heterogeneity of the SVF.

In clinical practice, it is important to predict when ASCs will reach therapeutic numbers for many logistical reasons, such as scheduling patient appointments and allocating laboratory resources. Predictive proliferation models for ASCs also have applications in research laboratories, such as optimising culture conditions. In clinical applications, it is envisaged that a set of features can be measured from newly isolated ASCs, after which their

proliferation can be predicted. If additional accuracy is required, further measurements can periodically be carried out. A mathematical model that has a sufficient number of measurable features to define the ASC population at the beginning of culture is needed to predict cell proliferation.

1.1.2 Research gap

Predictive capability refers to how well a model can predict the proliferation characteristics of a population of ASCs with only a set of initial measurements. Importantly, prior characterisation of the cell population should not be required, i.e. the model should be applicable to new or *unseen* patients.

The model will need to be applied to primary cells, i.e. cells that have not been cultured before. Primary cells are more heterogeneous and are not typically used to validate mathematical models, which usually rely on established cell lines [2].

The parameters and features of existing stem cell proliferation models are compared in Table 1.1. A feature is synonymous with an independent or explanatory variable, while a parameter refers to a constant (which may still be measurable).

Table 1.1 A comparison of existing stem cell proliferation models

Model	Number of parameters and features	Measurable parameters and features	Requires prior characterisation
Modified Sherley equation [3]	4	2	Yes
Generalised logistic [4], [5]	6	2	Yes
Population balance equation [4]	14	4	Yes
H3 model [6]	5	0	Yes
Random walk algorithm [7]	5	0	Yes
Three-dimensional model [8]	22	0	Yes
Confluency curve fit [9]	2	0	No

As can be seen in Table 1.1, all existing models, except the confluency curve fit [17] require full prior characterisation of a cell population, before proliferation can be predicted for subsequent experiments. This approach is known as batch processing, which contrasts with so-called *online* methods that can incorporate new data as it becomes available. Although the confluency curve fit can be considered an online method, it only utilises a simple second-order curve fit that is then extrapolated. This implies that the model has no biological meaning; consequently, the predictive capability of the model has very limited practical use.

The generalised logistic and the population balance equation were tested for their predictive capability [18]; however, this was for a population of cells that was already fully characterised prior to expansion. Furthermore, only a single parameter (the initial seeding density) was varied to test predictive accuracy.

Considering the typically large inter- and intra-patient variability of extracted adipose tissue [15], the lack of features and parameters that would allow for prediction at the start of expansion, is a significant limitation of existing models.

1.2 RESEARCH OBJECTIVE AND QUESTIONS

Existing cell proliferation models have limited predictive capability, because they require a full set of observations before parameters can be estimated. Additionally, these models show poor generalisation; they do not incorporate enough measurable features to be applicable to different patients.

The following research questions will be answered:

- When given a measured set of *N* features, for time $t = 0 \ldots m$, what is the accuracy by which the proliferation of a population of ASCs can be predicted for $t = (m + 1)$ to h, where h is a time in the future.
- How is the accuracy of prediction affected when *N*, m and h are varied?
- Can cells in non-dividing states be modelled, and can this be used to more accurately predict proliferation?

1.3 APPROACH

If static and reproducible culture conditions are assumed, then the *in vitro* expansion of ASCs is a closed system. Hence, the variability in the system is only governed by the initial cell population (i.e. the initial state). It is reasonable to assume that a certain set of features can be measured at (or near) the start of the culture that will allow the prediction of stem cell growth *in vitro*. This hypothetical set of features will be investigated by performing simulations of individual cells. The interaction of the features with the underlying population's proliferation will then be described mathematically and will be compared to measured experimental data.

1.4 RESEARCH GOALS

The primary research goal is to develop a predictive model for the proliferation of ASCs *in vitro*. The secondary research goal is to apply the model in a way that could be feasible in clinical settings, by only observing cells *in situ* through measurements that are non-destructive and do not affect cell viability.

1.5 RESEARCH CONTRIBUTION

This research contributes two approaches to the modelling of ASC proliferation: a cellular automata model, and a population model. The cellular automata model was developed as an *in silico* simulation platform of ASCs, through which the fundamental characteristics of contact-inhibited cell proliferation could be investigated. It was found that confluency and spatial dispersion are important measurable features with predictive capability, which has not previously been described in the literature.

A discrete Markov population model was adapted from first principles as a function of cell cycles and converted to a function of time to allow comparison to experimental measurements. The Markov assumption required a model for the mitotic fraction, which was implemented using the Verhulst and generalised logistic equations. The Verhulst equation

was found to describe the mitotic fraction as only a function of confluency, while the generalised logistic equation included various parameters with no biological meaning. A relationship between the undefined parameters and spatial dispersion was discovered and described mathematically.

1.6 RESEARCH OUTPUTS

The following article was submitted to a peer-reviewed and ISI accredited journal.

- De Bruin, K.J.F, De Villiers, J.P, and Pepper, M.S. "A Measure of Spatial Dispersion Summarises the Effect of Migration and Seeding Density in an *In Silico* Agent-Based Model of Contact-Inhibited Adherent Cells", submitted for publication.

1.7 OVERVIEW OF STUDY

A literature study in Chapter 2 introduces the most important concepts related to ASCs and the modelling of ASCs. It was found that ASCs are a highly heterogeneous population, and that inter- and intra-patient variability of growth kinetics have been observed. The limitations of existing models and approaches for prediction in a clinical setting are discussed.

A reductionist cellular automata model is presented in Chapter 3 that considers space-constraints as the only factor that determines whether a cell would remain within the cell cycle and divide. Within this framework, it was found that the initial seeding density and migration strongly influence the resulting growth characteristics. The combined effect of the seeding density and migration were summarised by measuring spatial dispersion.

A population model is presented in Chapter 4 that was derived from first principles. The effect of spatial dispersion on growth kinetics is modelled mathematically and is compared the simulated results of Chapter 3.

In vitro measurement techniques and the results of experiments are described and presented in Chapter 5. The descriptive and predictive ability of the population model is compared to

in vitro measurements in Chapter 6. Concluding remarks and recommendations for future work are presented in Chapter 7.

CHAPTER 2 LITERATURE STUDY

2.1 CHAPTER OBJECTIVES

A survey of the relevant literature is presented in this chapter. The objectives of the survey are to present ASC research within the broader context of clinical stem cell research, list the defining characteristics of ASCs that could be important for modelling, and discuss existing approaches to stem cell modelling.

2.2 STEM CELLS

Stem cells are broadly characterised by their ability to self-renew (i.e. divide to create additional stem cells) and to differentiate (i.e. become more specialised cells). These two characteristics, collectively referred to as *stemness* [10], make stem cells a promising clinical tool.

The two main types of stem cells are embryonic, obtained from embryos, and non-embryonic, which comprise of mostly adult stem cells [11]. Embryonic stem cells are associated with numerous ethical and legal concerns, while adult stem cells, such as those found in bone-marrow, adipose tissue, and peripheral blood, circumvent many of these concerns [12].

Transplantation of hematopoietic stem cells (HSCs) from bone marrow, peripheral blood, and cord blood is perhaps the most well-known and clinically-proven stem cell therapy, as illustrated by the one millionth transplant performed in 2013 [13] and the continued growth in the number of annual transplants [14]. Other clinical applications of stem cells remain mostly nascent and experimental [15].

The most abundant and accessible source of adult stem cells is adipose tissue [16]. Even though bone marrow is an important source of adult stem cells, adipose tissue harvesting via liposuction is safer, easier, and cheaper when compared to aspiration from bone marrow [17], [18].

2.3 ADIPOSE-DERIVED STROMAL/STEM CELLS

Adipose tissue was historically considered an inert energy store [19]. It has however also been shown to provide important endocrine functions and is an active participant in immune responses [20], [21]. Adipose tissue consists primarily of adipocytes, but also contains a variety of other cell types that are collectively referred to as the SVF [22].

The SVF was first isolated in 1966 [23], but a distinct population cells within the SVF that could be expanded *ex vivo* was only isolated in 2001, known as processed lipoaspirate (PLA) [24]. A year later, the stem-like characteristics of a subset of cells from PLA was demonstrated, and these cells were called adipose-derived stem cells [25].

2.3.1 Nomenclature

Bone marrow is most frequently used as a source of HSCs, but it also contains a population of multipotent mesenchymal stem cells (MSCs) [26]. The population of stem-like cells isolated from adipose tissue initially seemed very similar to MSCs, and both were frequently referred to as MSCs [27]–[30].

The International Society for Cellular Therapy (ISCT), in a 2006 paper, defined MSCs by their ability to adhere to plastic, express specific surface antigens, and differentiate into multiple lineages [31]. This definition included cells from adipose origin, which were referred to as adipose-derived MSCs.

A revised position was published in 2013 by the ISCT and the International Federation for Adipose Therapeutics and Science (IFATS), in which adipose-derived stromal/stem cells (ASCs) were defined as being distinct from MSCs [22]. Isolated ASCs are defined as

adipose-derived stromal cells, until self-renewal and multi-potency is proved, after which that they could potentially be referred to as adipose-derived *stem* cells [22].

2.3.2 Isolation procedure

Once harvested, adipose tissue is washed and digested (with an enzyme such as collagenase) to release the individual cell components, and then centrifugation is used to isolate the SVF, which forms a pellet at the bottom of the centrifugation tube [15], [22]. Various commercial systems have been developed to isolate the SVF with minimal manual intervention [19], [32]. The SVF can then be cultured *in vitro* in a suitable growth medium to isolate the plastic-adherent ASCs. This process can also be automated using commercially-available systems [33].

2.3.3 Therapeutic ability and methods of treatment

ASCs have demonstrated regenerative properties similar to other sources of adult stem cells and are also immunomodulatory [34]–[37]. These characteristics have underlined ASCs as a potentially useful therapy for treating various injuries, diseases and disorders [38]–[42].

The SVF is frequently transplanted directly into patients, especially for orthopaedic therapies, since it was initially considered a "minimally manipulated" treatment that would be safer and required less regulatory scrutiny [32], [43]. However, the number of ASCs contained in the SVF is generally not considered sufficient for use in therapy [43], and the inclusion of an uncharacterised mix of cells contained in SVF in addition to stem cells could be potentially detrimental to treatment outcomes [44]. Therefore, before using ASCs in treatments, the cells are isolated and expanded to therapeutic numbers in a process known as serial passaging [45], which is described in Figure 2.1**.**

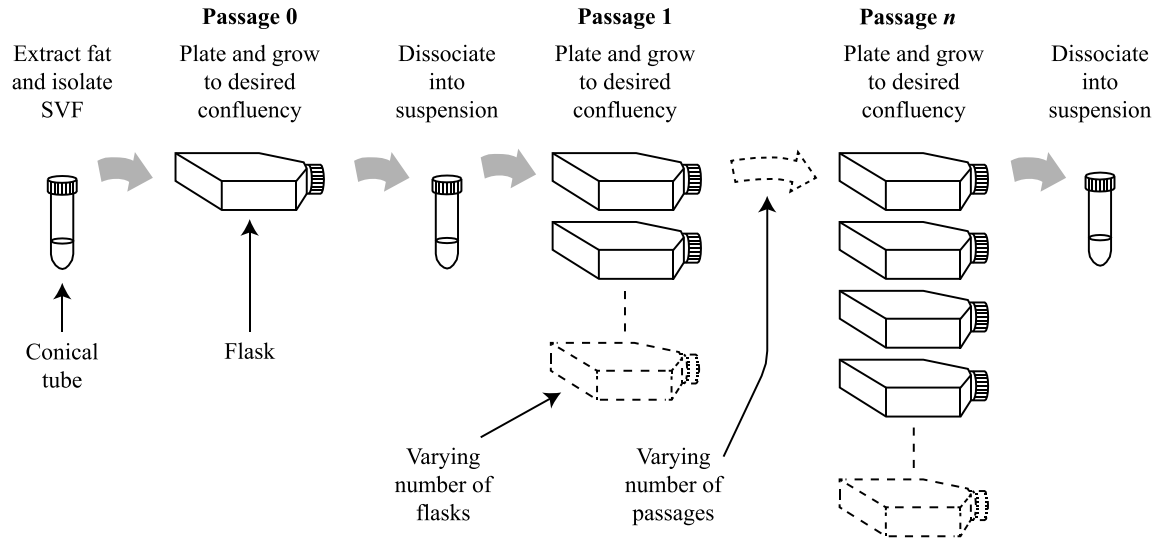

Figure 2.1. The process of producing therapeutic numbers of ASCs via serial passaging, adapted from the description of the process in [46]. Each passage entails plating cells into flasks, a period of growth to allow the cells to reach a certain confluency, followed by dissociation of the cells into a suspension. The dashed symbols indicate that the number of flasks can vary depending on the cell yield, and that various numbers of passages can be performed.

Once transplanted into a patient, various mechanisms though which ASCs affect diseased cells and tissues have been proposed [47], [48].

- ASCs are multipotent, and they differentiate and replace damaged cells *in vivo*,
- ASCs act through the release of growth factors that stimulate tissue repair, and/or
- ASCs secrete immunomodulatory factors to suppress immune and inflammatory responses, thereby enhancing recovery.

Clinical trials that apply ASC treatments to a wide array of diseases and disorders are still in progress [49], and the efficacy of ASCs in the clinic is still largely unproven. Encouraging results have been reported in reconstructive surgery, where cultured ASCs improved the viability of fat grafts [50].

The exact mechanism by which ASCs provide a clinical benefit may be important to consider when optimising an ASC yield for a specific treatment for future therapy [51], yet at this

nascent stage it is sufficient to note that ASCs have promising applications, and it is likely that ASCs will continue to be expanded *ex vivo* before use.

2.3.4 Serum

Several consumables are used in the process of isolating and expanding ASCs, and many of these are animal-derived [52]. ASCs are typically expanded in foetal bovine serum (FBS), which carries the risk of transmitting zoonotic diseases, or causing immune reactions when cells are transplanted into a patient [53].

In order to circumvent this, ASCs need to be expanded using human alternatives for serum, such as pooled human platelet lysate (pHPL) [53], [54]. Different sera used during expansion affect the characteristics of ASCs such as proliferation [55]. Thus, when compared to those expanded in FBS, a significant increase in cell viability and proliferation rate was reported when ASCs were expanded in pHPL [56].

2.4 CHARACTERISTICS OF ADIPOSE-DERIVED STROMAL CELLS

2.4.1 Proliferation

Most human cells from solid tissues are adherent when grown *in vitro*, and expand as a single layer on the culture flask substrate [46].

ASCs are in a suspension when seeded, but adhere to the substrate and spread via their cytoskeleton onto the surface before they enter the cell cycle [57]. The period during which this occurs is characterised by low or no proliferation.

Once attached to the substrate *in vitro*, ASC proliferation occurs according to the same cell cycle as all eukaryotic cells. The cell cycle, and the states outside of the cell cycle, are shown in Figure 2.2.

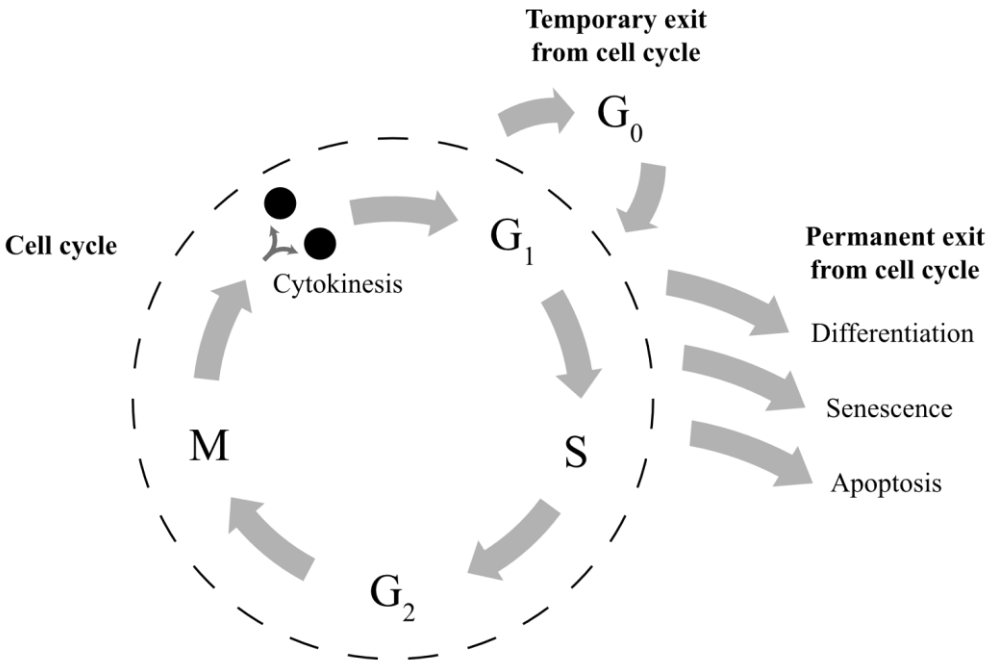

Figure 2.2. The ASC cell cycle, and states outside the cell cycle, adapted from [46], with permission. Additional annotations were adapted from [3]. The cell cycle consists of the gap 1 (G1), synthesis (S), gap 2 (G2), and mitosis (M) phases. At the end of the M phase, a cell divides into two daughter cells through cytokinesis. Quiescence or Gap 0 (G0) refers to a temporary exit from the cell cycle, while differentiation, senescence and apoptosis result in a permanent exit from the cell cycle.

Mitotically active (i.e. dividing) cells are considered as being within the cell cycle, and iterate through phases G1 to M, when the cell divides into two daughter cells through cytokinesis. One or both of the resulting cells can then either re-enter the cell cycle, or exit the cell cycle temporarily into a quiescent (G0) state, or permanently into a differentiated, senescent, or apoptotic state [3].

Quiescence refers to the state of cells that have temporarily stopped proliferating, while differentiation refers to a process through which cells have differentiated into more specialised cells and subsequently lost their proliferative ability. Both these fates are generally determined during G1 at so-called restriction points [46]. Apoptosis refers to cell death when the cell cycle is halted as a result of the integrity of DNA, specifically during checkpoints in the S and G2 phases [46]. Senescence refers to cells that have permanently

lost the ability to divide as a result of a genetic limit to the number of divisions that have occurred [46]. ASCs expanded in FBS reached senescence after a mean of 179 days and 22 doublings; and after a mean of 94.8 days and 43 doublings when expanded in pHPL [58]. Therefore, the authors noted that long term culture of ASCs is only minimally affected by senescence [58].

2.4.2 Contact inhibition and population limits

Adherent cells that are cultured *in vitro* are usually seeded at relatively low densities, which leaves the edges of cells free. This allows spreading of the cytoskeleton, and permits entry into the cell cycle [46]. As cells reach higher densities, proliferation is inhibited though contact with other cells, until confluence is reached (i.e. all available space is utilised). At this point, a certain culture area will reach a population limit where the number of additional cells added over time approaches zero. In general, the proportion of space utilised can be expressed as a percentage of confluency.

ASCs are characterised as plastic-adherent and contact-inhibited when expanded *in vitro* [15], [17], and remain so when expanded in pHPL [55], [58], [59]. Therefore, when grown in a two-dimensional flask, contact-inhibition implies that an ASC population limit exists where cells cease to divide owing to space constraints. This was confirmed by a gene expression study, where ASCs at low densities highly expressed proliferation-related genes, while ASCs at high densities did not [60]. Zhu *et al*. reported ASC proliferation that did not seem to reach confluency, although slowing growth was observed after 20 days [34].

2.4.3 Population growth kinetics

Adherent cell proliferation can be described by a succession of three phases [46], which is often referred to as growth kinetics. The three phases are shown in Figure 2.3. The first phase is known as the lag phase, during which cells attach to the substrate and virtually no increase in cell number is observed. This is followed by a log phase where cells expand exponentially at a rate that is frequently referred to as the doubling time. As cells become more confluent, they reach the saturation phase, when the growth rate approaches zero [46], [61].

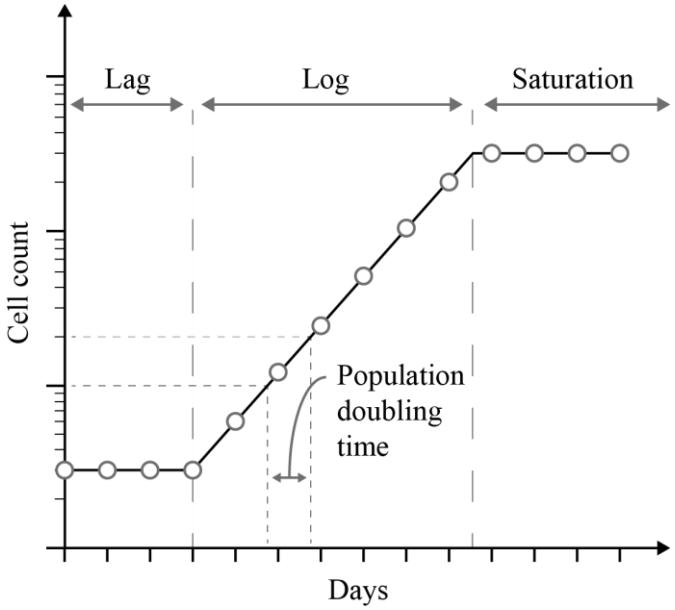

Figure 2.3. An example of the growth kinetics of adherent cell proliferation with the three phases that are typically observed in culture, adapted from [61], with permission. The vertical axis is logarithmic. An example of the population doubling time is depicted during the log phase.

Growth kinetics are typically quantified using proliferation assays [46] that measure cell counts daily. The counts are usually displayed on a semi-logarithmic plot, which aids in visually identifying the different phases.

ASCs expanded in FBS were reported by Kølle *et al*. [55] to have approximately no lag phase, a log phase of 16 days, and a saturation phase for the remaining time (measurements were taken up to 43 days) [55]. In the same study, ASCs that were expanded in pHPL exhibited no lag phase, a much shorter log phase of 6 days, and a saturation phase from day 7 up to the last daily measurement on the 43rd day [55].

Another proliferation assay of ASCs, performed by Zhu *et al*., identified a lag phase of 3 days and a log phase between days 4 and 7 [34]. Multiple logarithmic phases were reported in the following days; however, the counts exhibited high variability and could instead be interpreted as a single logarithmic phase until day 16. The 3rd reported logarithmic phase presented steadily increasing doubling times that could indicate a plateau.

2.4.4 Division time and population doubling time

Division can be broadly characterised by two different measures: the cell cycle time (also known as division time) and the population doubling time (PDT). The cell cycle time [46] can be calculated as the time it takes from a certain point in the cell cycle, until the same point in the cell cycle is reached by a cell's progeny. Similarly, the division time [62] of a cell refers to the time elapsed between the cell originating as a daughter cell, until the cell itself divides again. This can be measured per cell using live cell imaging, and results in a distribution of division times for a population of cells.

Using live cell imaging, two distinct populations of MSCs were identified that manifested in a bi-modal distribution of division times: a slow-dividing population with a median division time of 16.8 hours, and a faster-dividing population with a median division time of 12.8 hours [62].

The second measure, PDT, is frequently used to characterise the log phase of a population of cells, and is defined as [46]

$$PDT = (\mathrm{t}_2 - t_1) \log_{\frac{N_2}{N_1}} 2. \tag{2.1}$$

The PDT is calculated between two time points, t_1 and t_2, using the cell numbers at those time points, N_1 and N_2. An example of the population doubling time on a graph, when the cell count is represented on a logarithmic axis, is shown in Figure 2.3. This is equal to the average division time of the individual cells that comprise the population, if it is assumed that *all* cells in the population are mitotically active. If this assumption is not accurate, then the PDT will be prone to underestimate the average division time, since it includes non-dividing cells during that period [34], [46].

It has been reported that ASCs expanded in FBS have a PDT of 123.9 hours, while those expanded in pHPL have a much shorter PDT of 29.6 hours [55]. Rogulska et al. reported FBS-expanded PDTs with a mean of 89.2 hours, and pHPL-expanded PDTs with a mean of 42 hours [56]. Agostini et al. reported similar findings, where ASCs (at passage 0) expanded in pHPL had doubling times between 34 and 39 hours [63].

ASCs expanded in FBS have PDTs that appear to be dependent on passage number, where a doubling time of 36 hours reported at passage 3 increased to 96 hours at passage 25 [34]. Cryopreservation does not appear to have a significant effect on ASC PDT [56].

2.4.5 Migration

Many adherent cells in culture can migrate across the substrate [46]. The distance travelled by cells in a certain period is known as motility. The amount of motility seems to depend on the confluency of the cells, with a lower density of cells associated with higher motility [46]. Motility can be quantified using live cell tracking [46], [62].

2.4.6 Heterogeneity and influencing factors

Different adipose tissue harvesting procedures [64], methods of isolation [18], initial seeding densities [60], and the composition of cell culture media [65] significantly affect the characteristics of the resulting isolated ASC population. In addition to this variability, the defining criteria of isolated ASCs are not considered to be sufficiently specific [52], and have been frequently revised [31], [66].

Compounding the variability in technical procedures, there is substantial inter- and intra-patient variability in the yield of cells obtained [67], as well as the proliferation characteristics of ASCs, even with precisely-regulated culture conditions [68]. This may likely be a consequence of the heterogeneity of the SVF [69]–[72].

2.5 MODELLING STEM CELL PROLIFERATION

The majority of existing approaches to modelling stem cell proliferation have been *ad hoc* curve fitting [6], [9], while biologically meaningful models have required full characterisation of a specific population of cells prior to modelling them in subsequent expansions [3], [73].

Biological population growth is often modelled with an exponential function that considers the entire population as perpetually mitotically active; however, adherent stem cell growth

in vitro does not conform to this simplified assumption [3]. This can be attributed to proliferation constraints, such as limited space and exhaustion of nutrients in growth medium. Because of these constraints, certain cells in the population enter non-dividing growth states outside of the cell cycle. These heterogeneous cell populations can be incorporated into growth models by modelling the size of the mitotically active population [3], where any cell within the cell cycle is seen as being mitotically active, while cells that exit the cell cycle do not contribute to proliferation. As discussed in Section 1.4.2, ASCs are adherent when expanded *in vitro*, and demonstrate contact-inhibition. Therefore, in a limited area (such as a plate or flask), there is a limitation on the maximum population size.

One of the first models to incorporate a limiting factor to population growth, the Verhulst logistic equation, slows the population growth rate as the population increases towards a limit (often referred to as the carrying capacity) [74]. The Verhulst equation is widely applicable, and is still frequently utilised to model population growth; recent examples include modelling the population growth of aquatic macrophytes [75], [76], and myoblasts [77]. The Verhulst equation has also been extended with additional parameters as the Richards equation [78], and other so-called generalised logistic equations [79].

Other strategies of modelling population dynamics have attempted to model the interaction of individual cells. Cellular automata are computational models of cells in a grid of multiple dimensions that follow certain rules [80], and are useful representations of non-linear dynamics [81]. When the rules that each cellular automaton follow are probabilistic, they can be used as simplified models of biological phenomena, and have been used to model stem cell proliferation [7], [29].

The proliferation of endothelial cells, which are also adherent and contact-inhibited like ASCs, has been modelled using cellular automata [82]. Cell lines (which are characterised by repeatable results) were expanded, yet it was observed that the lag time (as described in Section 2.4.3) varied considerably between cells. After accounting for the lag time, and when provided with measurements of the cell line (such as motility data and cell division times), the model could accurately predict the means of normalised cell counts. However, the accuracy was not quantified, and more problematically, only a single realisation of each

predicted growth curve was shown. Therefore, the variability of the model was not quantified, nor displayed on validation graphs.

Cellular automata have been used in the context of ASC research by Cholewa *et al.*; however, their simulations were only used to garner insights, and no validation using experimental data was attempted [58]. Other limitations of this study were that only the number of doublings were modelled (not cell counts), and that simulations were only performed for long-term culture (longer than 60 days). The model highlighted the effects of seeding density and migration: a lower seeding density resulted in higher variation in doublings, while migration resulted in less contact inhibition and more doublings. The same model was used in a separate study to model ASC colony-forming units; however, only *ad hoc* experimental validation was performed, and it was arbitrarily assumed that cells had 12 hour division times and a total absence of migration [29].

2.6 CHAPTER SUMMARY

In this chapter a description of ASCs has been provided in the context of stem cells and clinical applications. In Section 2.2 the concept of a stem cell was introduced, and a brief description of the clinical landscape was presented. In Section 2.3 a historical perspective of ASCs was provided and the change in nomenclature was listed. The basic principles of the ASC isolation procedure and therapeutic ability were discussed, and the importance of clinical-grade serum such as pHPL was emphasised. Characteristics of ASCs that may be relevant to modelling were highlighted in Section 2.4, such as growth kinetics and typical division and population doubling times. Section 2.5 provided existing approaches to mathematical modelling of stem cells and ASCs, and insights and limitations of these studies were identified. This chapter provided a theoretical foundation on which new models can be based, and the characteristics that were described could guide the assumptions of these models.

CHAPTER 3 CELLULAR AUTOMATA

3.1 CHAPTER OBJECTIVES

Complex phenomena can be investigated by simulating the interaction of various entities that each follow certain rules. This is often referred to as agent-based modelling.

The objective of this chapter is to develop an *in silico* agent-based model to gain insights about the fundamental characteristics of ASC proliferation. The simulation model should assess the effects on population dynamics, while emphasising variables and parameters that can be measured experimentally.

3.2 INTRODUCTION

ASCs are characterised as adherent and contact-inhibited; this implies that as the number of cells increase in a constrained area, proliferation slows as more cells come into contact with adjacent cells. A reductionist model of ASCs can be implemented by considering space-constraints as the only factor that determines whether a cell will cease to divide. Furthermore, the following assumptions are made:

- on a simulated substrate, a static, limited surface area is available,
- each cell occupies an equal surface area,
- the same area cannot be occupied by more than one cell, and
- symmetric cell division occurs, i.e. two identical daughter cells are produced when a cell divides, and both retain the ability to divide if space is available.

In probabilistic cellular automata models [7], a certain cell in a simulated matrix will duplicate itself to any open adjacent space with equal probability. Adjacent spaces are defined as either within the Moore or Von Neumann neighbourhoods, as seen in Figure 3.1.

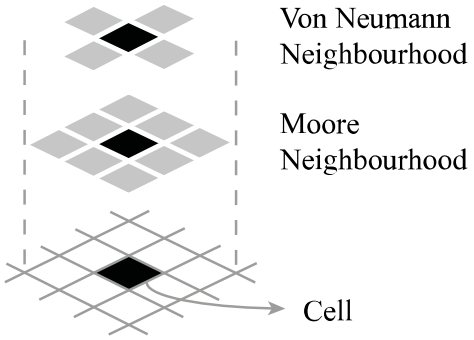

Figure 3.1. Each cell on the simulated substrate has a neighbourhood of adjacent spaces that can be defined by either the Von Neumann or Moore neighbourhoods.

Let an $m \times n$ matrix $\bar{A}$ of binary elements represent the existence of cells on a two-dimensional substrate

$$\bar{A} = \begin{bmatrix} a_{11} & \cdots & a_{1n} \\ \vdots & \ddots & \vdots \\ a_{m1} & \cdots & a_{mn} \end{bmatrix} \in \{0, 1\}. \tag{3.1}$$

At a certain epoch, x, the number of cells on the substrate is given by

$$N_x = \sum_{i=1}^{m} \sum_{j=1}^{n} a_{ij}. \tag{3.2}$$

Each element has a Von Neumann neighbourhood of 4 adjacent elements that comprise the set within unity Manhattan distance

$$V(a_{ij}) = \{a_{i+1,j}, a_{i,j+1}, a_{i-1,j}, a_{i,j-1}\}. \tag{3.3}$$

A cell will then divide in epoch $x + 1$ into any open adjacent space with equal probability

$$\frac{1}{\sum(1 - a)}, \tag{3.4}$$

for each a in the set V.

The divisor in (3.4) denotes the number of adjacent spaces that are open (i.e. that do not contain cells) in the defined neighbourhood. If at least one empty adjacent space exists, then a cell is certain to divide.

A set of 8 elements that comprise a Moore neighbourhood of cells within unity Chebyshev distance can be similarly defined as

$$M(a_{ij}) = \{a_{i+1,j}, a_{i+1,j+1}, a_{i,j+1}, a_{i-1,j+1}, a_{i-1,j}, a_{i-1,j-1}, a_{i,j-1}, a_{i+1,j-1}\}. \quad (3.5)$$

A cell undergoing simulated mitosis is considered for various scenarios of available adjacent spaces in Figure 3.2, with arrows indicating the possible locations of the divided daughter cell. There are 16 permutations of adjacent cell locations in a Von Neumann neighbourhood, of which 5 are considered in Figure 3.2.

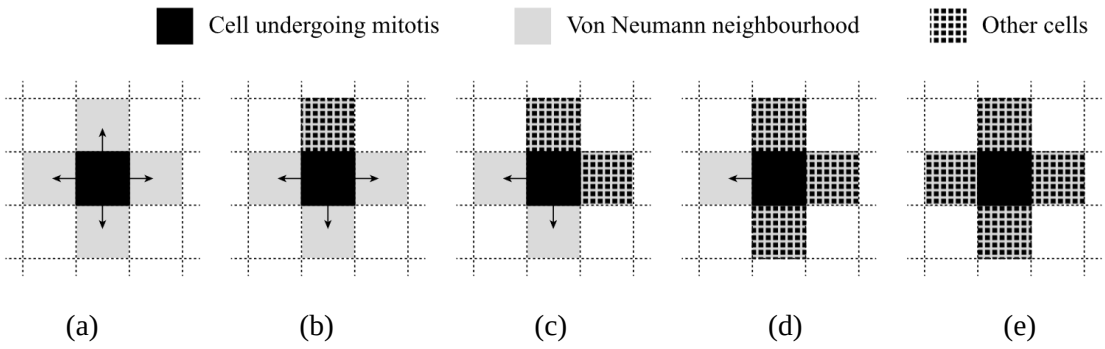

Figure 3.2. A cell undergoing mitosis (solid black), has a Von Neumann neighbourhood (grey) with: (a) 4 open adjacent spaces, and will divide into each space with probability $1/4$; (b) 3 open adjacent spaces, and will divide into each space with probability $1/3$; (c) 2 open adjacent spaces, and will divide into each space with equal probability; (d) 1 open adjacent space, and can only divide into this particular space; (e) zero open adjacent spaces, and cannot divide during this epoch.

The model can be generalised by considering the number of cells as a fraction of the matrix size. Consider a matrix of size $m \times n$ as defined in (3.1), which implies a population limit of

$$K = mn. \quad (3.6)$$

At a certain epoch x, let the matrix contain N_x cells. Confluency at that epoch can then be defined as

$$\gamma_x = \frac{N_x}{K}. \tag{3.7}$$

The confluency at epoch zero, γ_0, will be referred to as the seeded confluency. It should be noted that although γ_0 (%) is conceptually similar to seeding density (cells/cm^2), it is dependent on a certain population's limit K, and not on surface area.

A mitotically active cell at epoch x, is defined as a cell that will divide at epoch $x + 1$. Each cell that is mitotically active during epoch x is counted towards the mitotic fraction, α_x, and is defined as

$$\alpha_x = \frac{N_{\alpha_x}}{N_x}. \tag{3.8}$$

This is illustrated in Figure 3.3, where at a certain epoch x, N_x cells exist, of which some are mitotically active during that epoch (N_{α_x}) and divide in the next epoch. Mitotically active cells are indicated in grey.

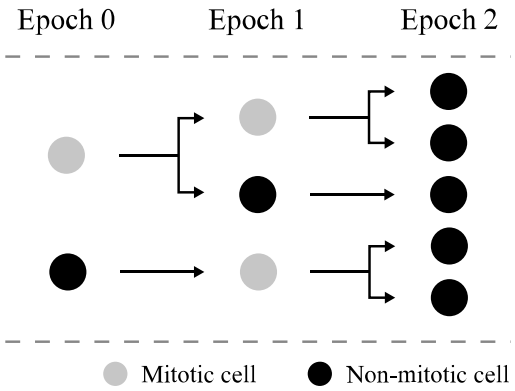

Figure 3.3. An example of cells that are counted towards the mitotic fraction (grey) that divide in the next epoch, and non-mitotic cells (black) that remain undivided during the next epoch. The scenario is considered across two epochs after seeding.

A realisation of the model for a 10×10 matrix, seeded with 3 cells ($N_0 = 3$) is shown in Figure 3.4.

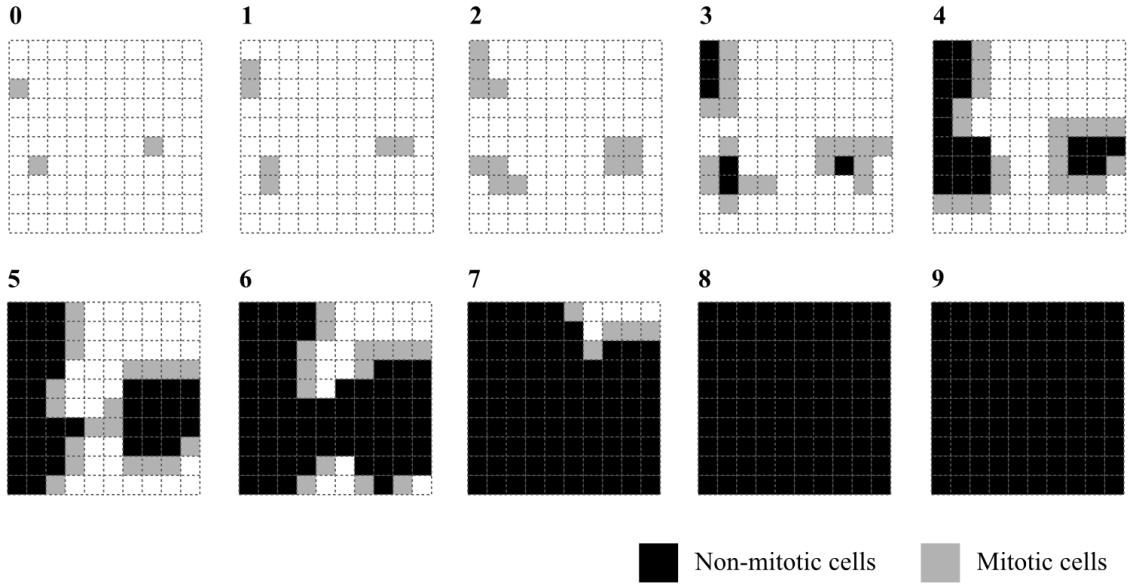

Figure 3.4. An example of the probabilistic cellular automata model for cell proliferation in a 10×10 matrix at $N_0 = 3$, proliferating until confluent. Non-mitotic cells are indicated in black, and mitotic cells that will divide in the next epoch in are indicated in grey.

3.3 PRELIMINARIES

3.3.1 Neighbourhood

The Von Neumann neighbourhood of adjacent cells defined in (3.3), or the Moore neighbourhood that includes the additional diagonal spaces defined in (3.5), can be used to determine if an open space exists for division. The number of cells per epoch are compared at different seeded confluencies, for Von Neumann and Moore neighbourhoods, in Figure 3.5.

The different neighbourhoods result in similar numbers of cells per epoch initially, but the Moore neighbourhood then results in a greater number of cells and reaches the population limit more quickly. This can be attributed to the additional spaces that are available for division in the Moore neighbourhood, which mitigates the limiting effects of increased confluency.

The limiting effects of contact inhibition are important to consider in this study, and this is more evident in the Von Neumann neighbourhood; therefore, the Von Neumann neighbourhood is used in all simulations in the subsequent sections.

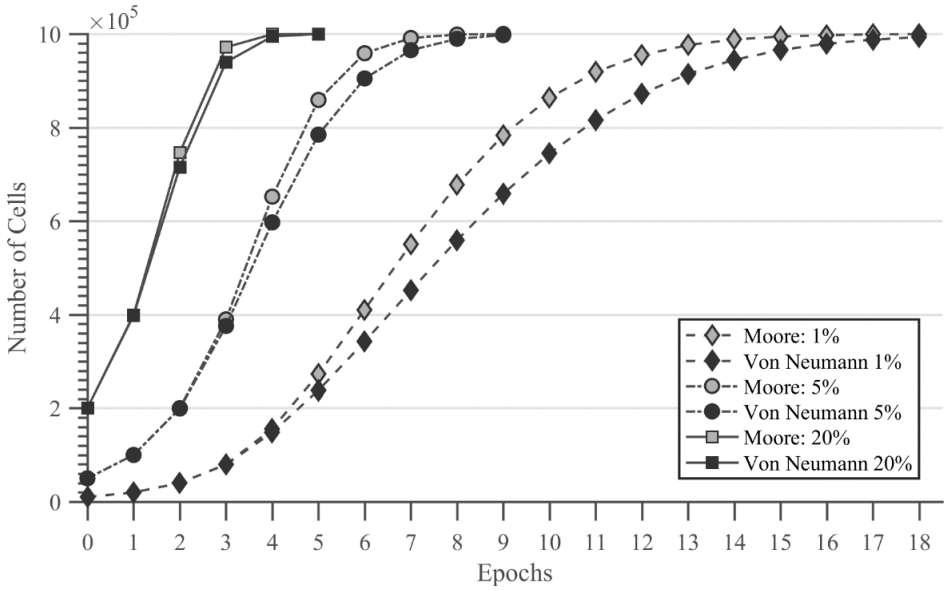

Figure 3.5. The number of cells per epoch for Von Neumann and Moore neighbourhoods of populations seeded at 1%, 5% and 20% confluency. Standard deviations were less than 0.2% of the mean at all points and 1000 simulations of each set were performed.

3.3.2 Matrix size

Given that confluency, as defined in (3.7), and the mitotic fraction, as defined in (3.8), are independent of the matrix size, then a smaller matrix could be used to simulate cell populations that are orders of magnitude bigger. However, since cells on the boundaries of the matrix are limited by space constraints that are not caused by other cells, this disproportionally affects smaller matrix sizes. Therefore, the simulated matrix needs to be a certain minimum size in order for the boundary effects to not skew the results. The effect of the population limit K on the population characteristics is considered in Figure 3.6.

The median number of cells in Figure 3.6 (a) is similar, but the variance of the number of cells is greater in smaller matrices, as seen in Figure 3.6 (b). An empirical probability distribution estimate of the number of cells at epoch 7, using a normal kernel function, is shown in Figure 3.7.

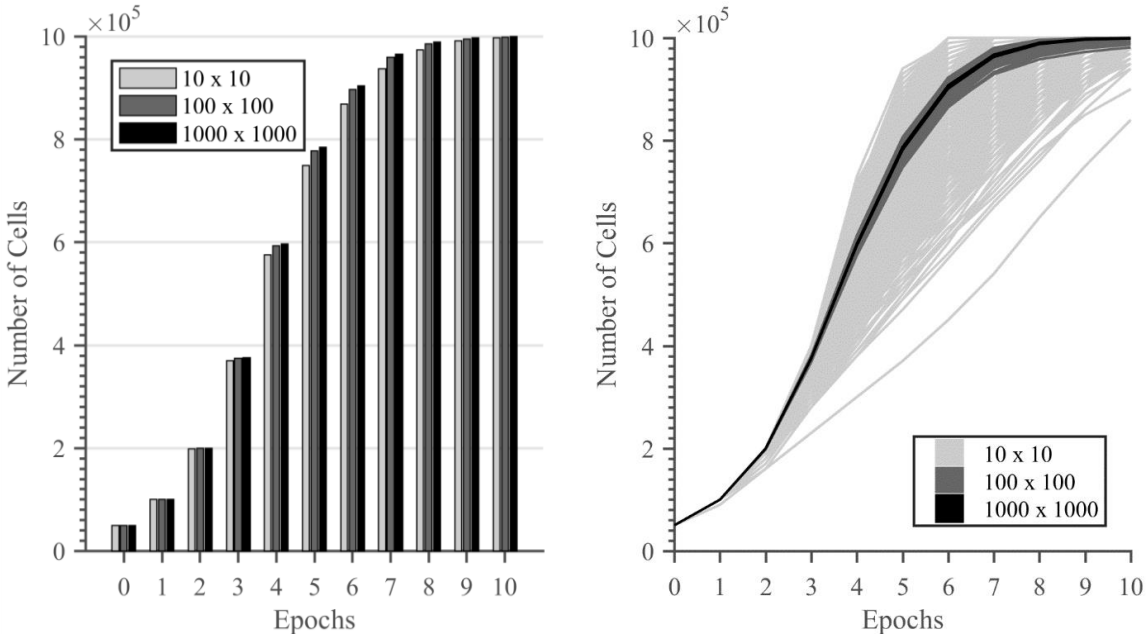

Figure 3.6. Cells seeded at 5% confluency are considered across 10 epochs in matrices with population limits 10^2, 10^4 and 10^6. The (a) the median number of cells and (b) individual realisations of 1000 simulations per population limit are shown.

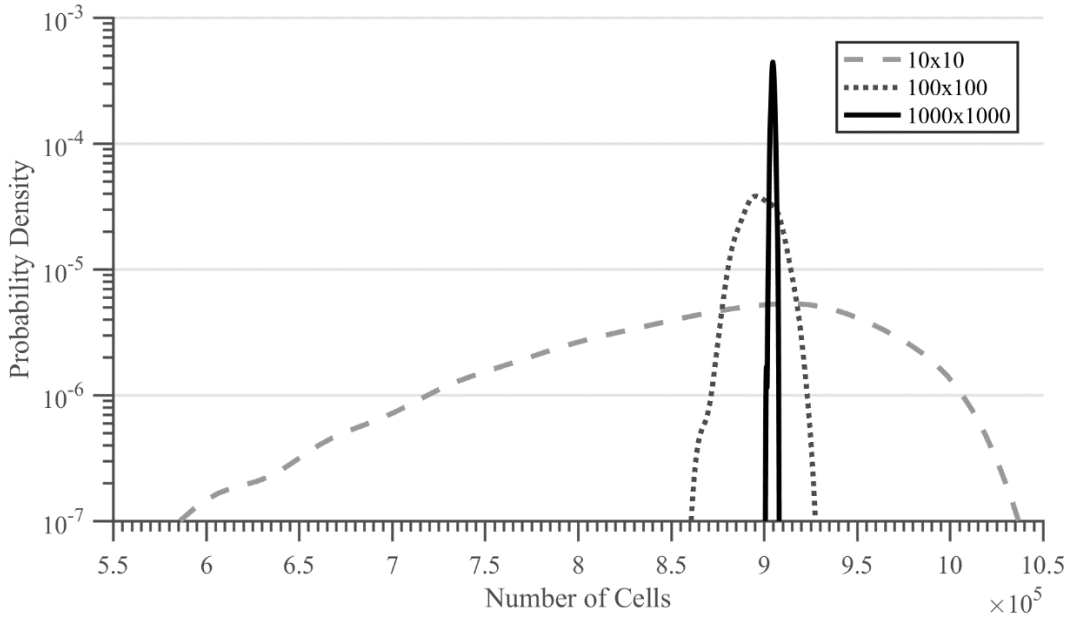

Figure 3.7. The empirical probability distributions of the number of cells at epoch 7 are shown for matrices with population limits 10^2, 10^4 and 10^6. The distributions were estimated using a normal kernel approximation of 1000 Monte Carlo simulations.

Considering that the boundary effects should be minimised, all subsequent sections simulate matrices with a population limit of $K = 10^6$.

3.4 CHARACTERISTICS

3.4.1 Seeded confluency

The effects of multiple epochs can be simplified by only considering cells for a single epoch. Consider N_0 cellular automata that are each seeded randomly (uniformly distributed) in a matrix of size K, with a corresponding seeded confluency γ_0. Out of the set of seeded cells, a cell is chosen randomly, and if there are one or more open spaces adjacent to the cell, then that cell is considered mitotically active. In the case of this scenario, $i = 0$; i.e. the mitotic fraction is only calculated for a single epoch. If the cell is mitotically active, it divides into an adjacent open space, possibly preventing cells not yet considered in the random selection from dividing. This is repeated until each originally seeded cell is considered exactly once. Figure 3.8 (a) shows the relationship between the seeded confluency and the mitotic fraction, which implies that for a given seeded population an estimate for the initial mitotic fraction can be readily inferred. Additionally, an upper limit exists for the mitotic fraction at a certain seeded confluency, when considering a purely space-constrained model for a single epoch.

It cannot be assumed that cells will remain uniformly distributed across multiple epochs. A statistical dependency exists between the previous position of a dividing cell, and whether its descendants will be mitotically active in future epochs: if a cell divided in the previous epoch into an adjacent space, its daughter cells are less likely to be mitotically active as a result of space constraints.

The previous scenario of randomly seeding various confluencies was extended to allow each seeded population to divide until fully confluent. The relationship between the confluency at each epoch and the mitotic fraction of that population is shown for various seeded confluencies in Figure 3.8 (b). Cells that are seeded at a lower confluency result in a mitotic fraction that remains lower across multiple epochs when compared to cells seeded at a higher

confluency. This can be expected when considering that cells are seeded uniform randomly, but cannot migrate.

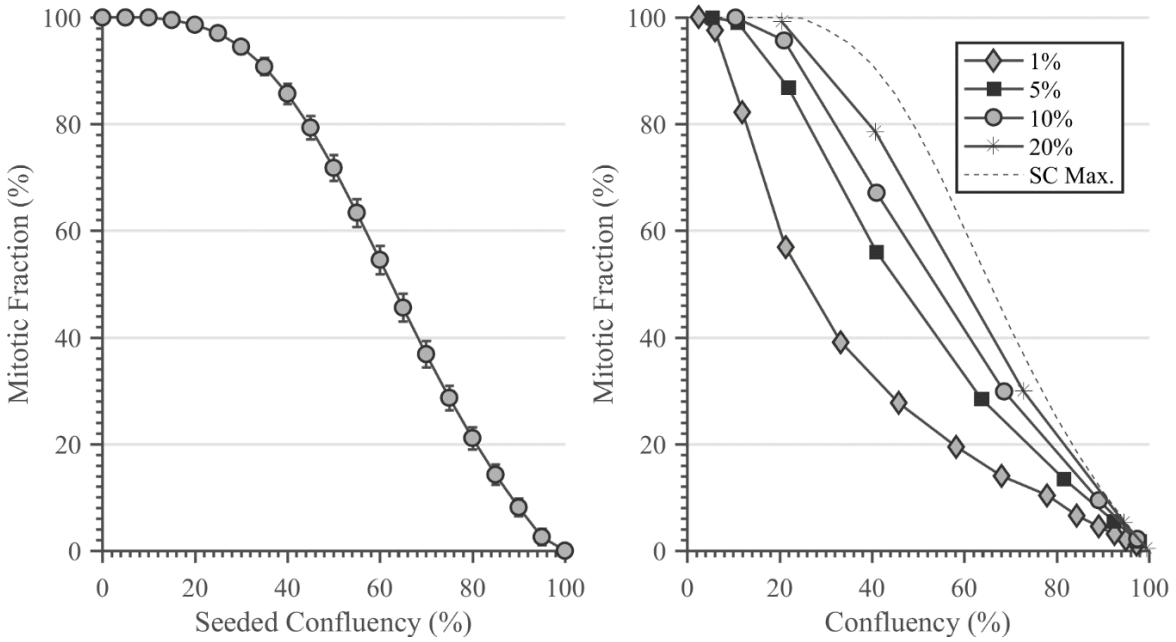

(a) (b)

Figure 3.8. The mitotic fraction as a function of confluency for cellular automata seeded and considered for (a) a single epoch, seeded uniform randomly into a matrix of size $K = 10^6$, and (b) multiple epochs seeded at 1%, 5%, 10% and 20% confluency and division was simulated until confluent. The dotted line represents the maximum mitotic fraction for each seeded confluency (abbreviated as SC Max.) of the data in (a).

3.4.2 Migration

Adherent ASCs have the ability to migrate when proliferating *in vitro* [83]. This can be simulated in the cellular automata model by using a similar sequence compared to division: if there are one or more adjacent open spaces in the defined neighbourhood, a cell migrates into them. After each cell is allowed to migrate, division occurs as previously described. Figure 3.9 shows the effect of division on the mitotic fraction of a given confluency and seeded confluency. As seen in Figure 3.9, an increase in migration results in an increase in the mitotic fraction for a given confluency and seeded confluency, which approaches the maximum mitotic fraction possible for a certain seeded confluency.

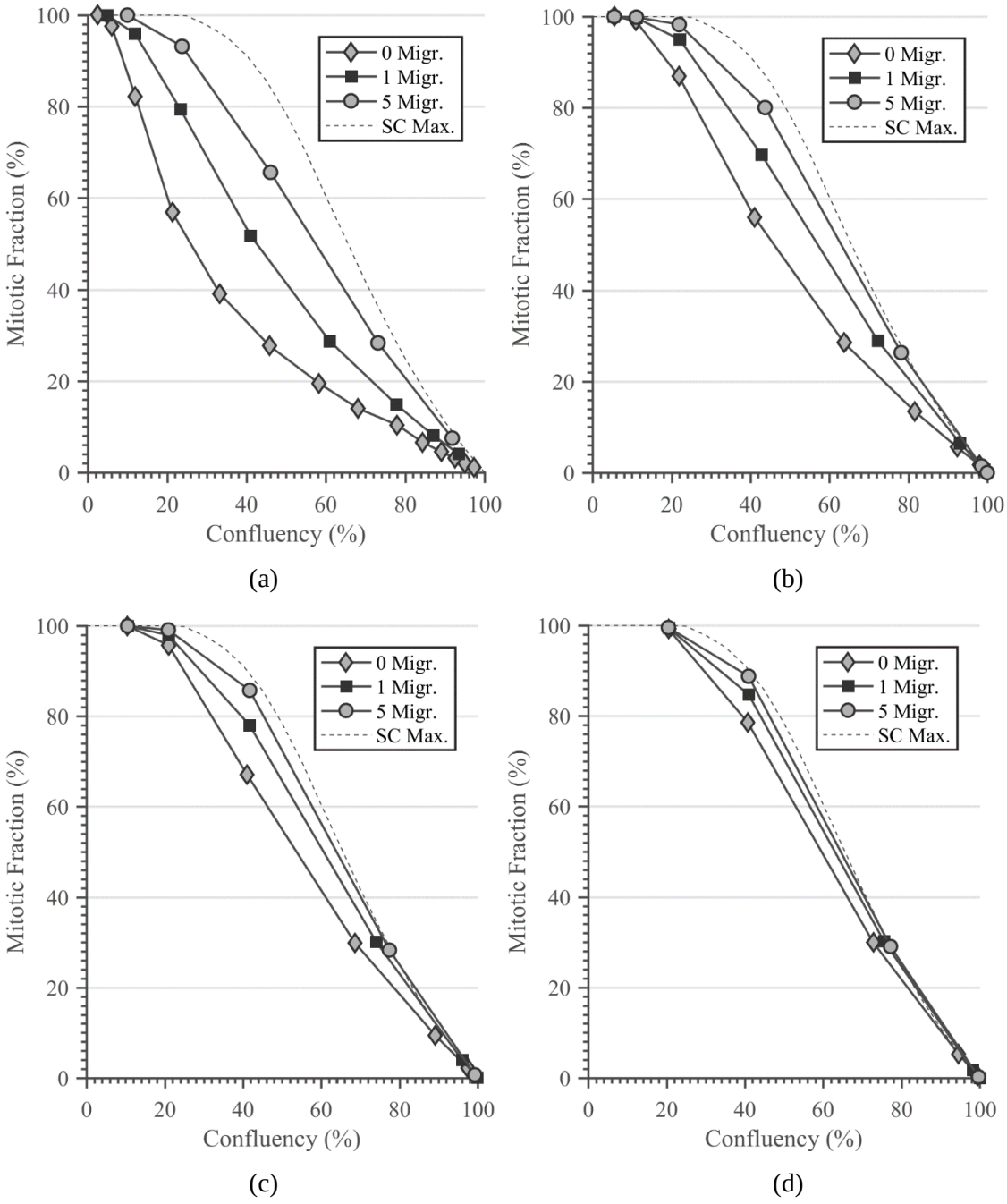

Figure 3.9. The influence of migration on the mitotic fraction of a population of cells at a certain confluency, for cells seeded at (a) 1%, (b) 5%, (c) 10% and (d) 20% confluency. In each case, curves for no migration (0 Migr.), 1 migration per epoch (1 Migr.), and 5 migrations per epoch (5 Migr.) are shown. Additionally, the maximum mitotic fraction for each seeded confluency (abbreviated as SC Max.) is indicated by the dotted line, which represents the maximum of the data shown in Figure 3.8 (a).

3.4.3 Spatial dispersion

Sections 3.4.1 and 3.4.2 indicated that the mitotic fraction is not only a function of confluency, but also of the seeded confluency and migration. The effect of the seeded confluency and migration on the underlying population of cells can be visualised by the four scenarios at the same confluency shown in Figure 3.10.

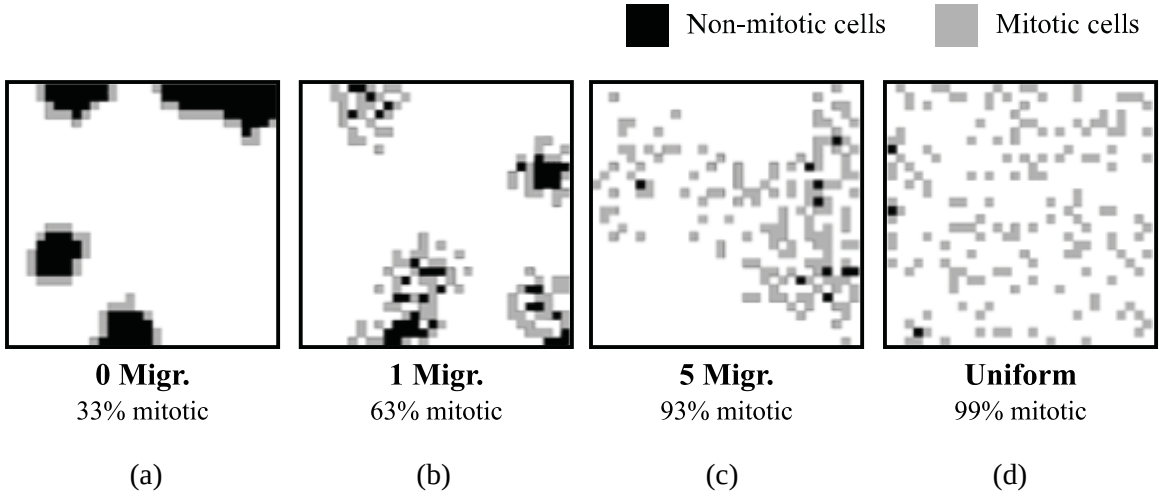

Figure 3.10. Representative samples of cell populations at approximately 20% confluency that illustrate the effect of the spatial grouping of cells on the mitotic fraction. Non-mitotic cells are shown in black and mitotically active cells are shown in grey. $N_0 = 4$ cells were seeded in (a), (b) and (c) and allowed to expand until approximately 20% confluency, with 0, 1 and 5 migrations (abbreviated as migr.) per epoch respectively. The cells in (d) were seeded uniform randomly at 20% confluency and considered for a single epoch.

Figure 3.10 (a) indicates that a low seeded confluency and no migration results in cells that form colonies that limit proliferation, where only the outer edge of each colony is able to divide. This results in a low mitotic fraction of only 33%. Figure 3.10 (b) and (c) have the same seeded confluency as (a), but cells were allowed to migrate each epoch (once, and five times, respectively). This resulted in cells that were spread out more evenly, therefore permitting higher mitotic fractions of 69% and 93%, respectively. Figure 3.10 (d) represents an instance of cells that were seeded at 20% confluency, which resulted in a mitotic fraction of 99%.

Therefore, cells that are more evenly distributed across the matrix result in a higher mitotic fraction. Higher seeded confluencies, and more frequent migration result in cells that are distributed more evenly, which explains the effects observed in Sections 3.4.1 and 3.4.2.

The manner in which cells are arranged on the matrix can be quantified by measuring *spatial dispersion*. If the matrix is divided into equal-sized areas called quadrats, and the number of cells in each quadrat is counted, then an index of dispersion can then defined as the ratio of the variance (σ^2) to the mean (μ) of the quadrat counts, i.e.

$$I = \frac{\sigma^2}{\mu}. \tag{3.9}$$

As I approaches zero, it indicates that cells are equidistant, or that the distribution is degenerate, such as a fully confluent matrix. As I approaches unity, it indicates that cells are approximately Poisson distributed: e.g. when initially seeded. An index of dispersion greater than unity indicates that cells are clumped together, and increases as more clumping occurs.

Figure 3.11 compares the mitotic fraction as a function of confluency when the indices of dispersion were divided into intervals. Cells were simulated at seeded confluencies from 0.01% to 99.99% and migrations were simulated between 0 and 5 times per epoch. Proliferation was then simulated until cells were confluent, and the mitotic fraction, confluency, and index of dispersion at each epoch was measured. The index of dispersion was calculated for quadrats of 5×5 within the matrix. The curves in Figure 3.11 indicate that when both confluency *and* spatial dispersion are known, then the mitotic fraction can be inferred more accurately than when only confluency is known. As seen in Figure 3.11, low indices of dispersion (cells that are spread out evenly) are associated with the highest mitotic fractions for a given confluency. Conversely, higher indices of dispersion (cells clumped together) result in lower mitotic fractions for a given confluency.

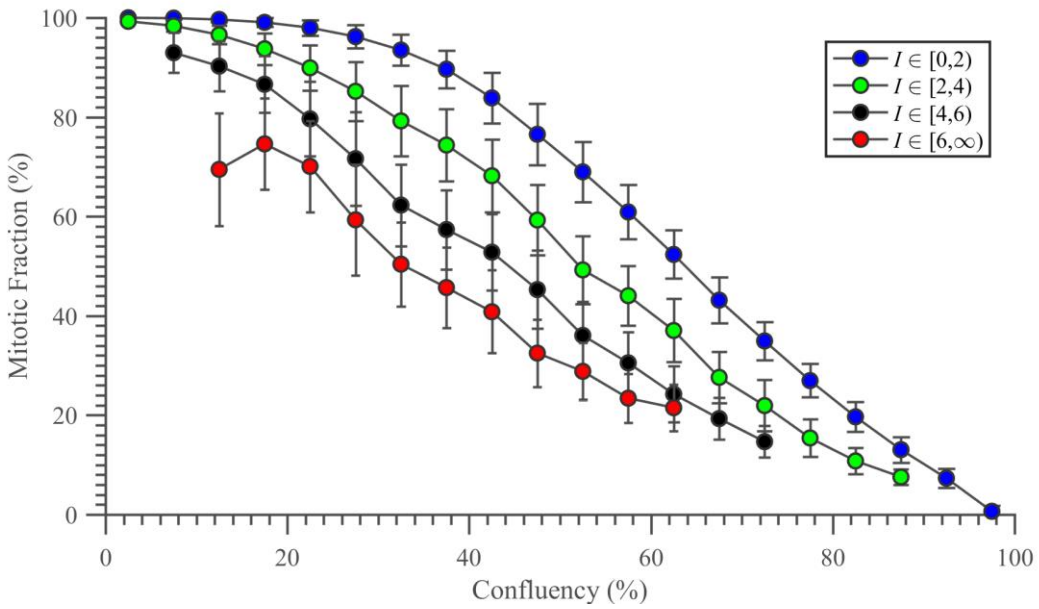

Figure 3.11. The mitotic fraction represented as a function of confluency for various intervals of spatial dispersion. Cellular automata were simulated at $N_0 = 1{:}\,10^6$, and migration was simulated between 0 to 5 times prior to division at each epoch. The curves represent 20000 Monte Carlo simulations.

3.5 ENHANCEMENTS

3.5.1 Apoptosis

Cells are cultured in an environment that mimics the human body, but two-dimensional culture using a growth medium does not perfectly replicate it. Cells experience certain stresses because of the foreign environment. Programmed cell death, known as apoptosis, is activated as a result of medium deficiencies or other factors that cause cellular stress [46]. The cell culture environment is kept approximately constant, and culture medium is regularly replenished. Therefore, any environmental stress would remain approximately constant during culture, and apoptosis could be modelled as a random process that occurs independently during each epoch.

In the cellular automata model, prior to division, each cell was considered for apoptosis with a constant probability per epoch. If a cell enters apoptosis, it is removed from the matrix,

and an open space remains. The result of 5%, 10% and 15% apoptosis per epoch is shown in Figure 3.12.

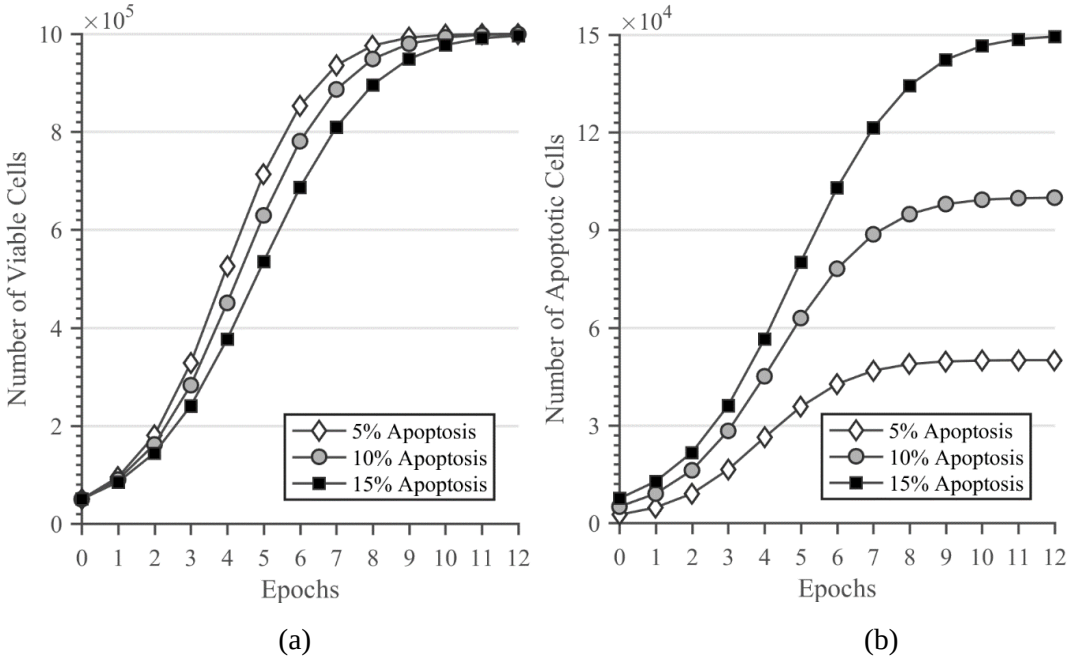

(a) (b)

Figure 3.12. The number of (a) viable cells, and (b) apoptotic cells per epoch, when 5%, 10% and 15% apoptosis per epoch occurs. Cells were simulated at a 5% seeded confluency, with no migration prior to division.

3.5.2 Cell epoch phases and the time-domain

In previous sections, cellular automata were considered for epochs, which can be interpreted as cell cycles. Practical applications of cellular automata simulations, such as prediction of cell counts, require conversion from epochs to time. Epochs can be converted to time by incorporating a division time, as seen in Figure 3.13, where the duration of each epoch corresponds to the division time.

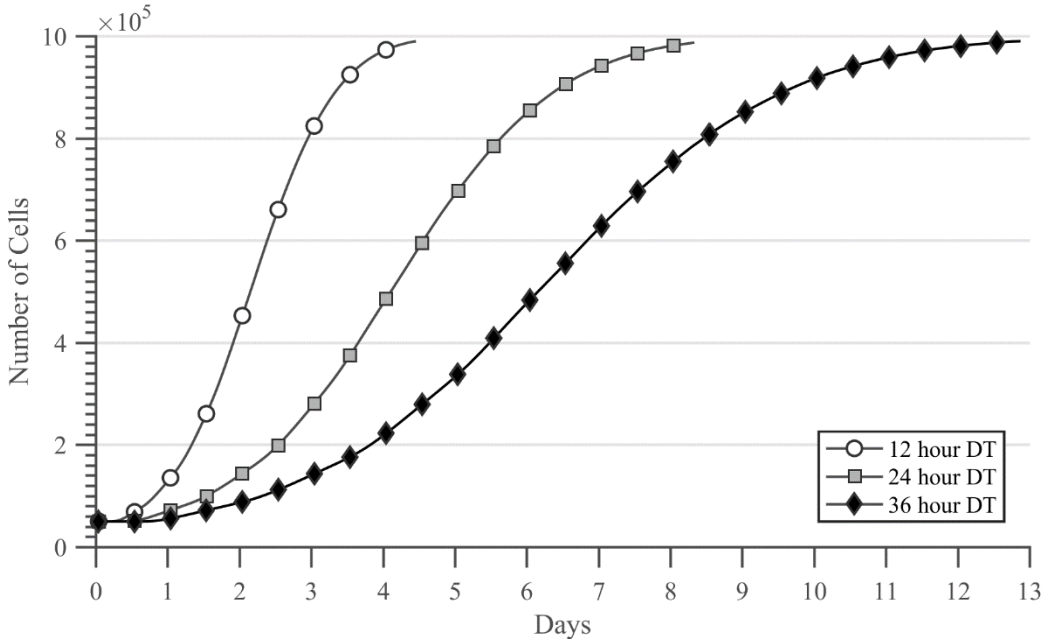

Figure 3.13. The number of cells over time for 12 hour, 24 hour, and 36 hour division times, when epochs are converted to hours.

In addition to the cell cycle time, the underlying phases of the cell cycle can also be simulated. In a human cell with a total cell cycle time of 24 hours, the G1 phase takes approximately 11 hours, the S phase approximately 8 hours, the G2 phase approximately 4 hours, and the M phase about 1 hour [84]. The percentage of cells in each phase of the cell cycle using these fractions, are shown in Figure 3.14. It is initially (somewhat unrealistically) assumed that cells are synchronised, i.e. each cell is initially in the same phase.

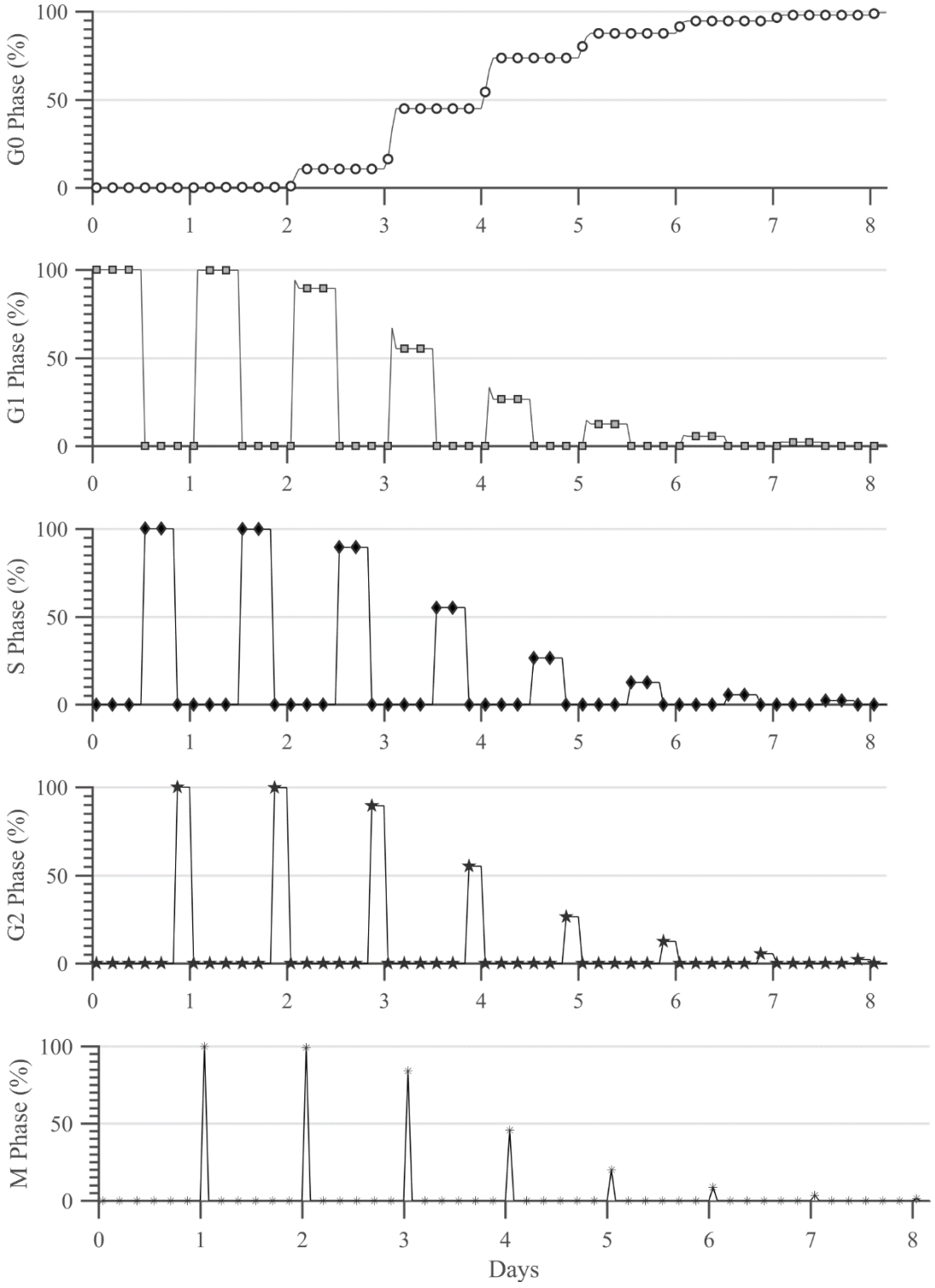

Figure 3.14. The percentage of cells in each cell cycle phase over time, when a total cell cycle of 24 hours is divided into a G1 phase of 11 hours, an S phase of 8 hours, a G2 phase of 4 hours, and an M phase of 1 hour. Cells were initialised into the G1 phase and assumed to be synchronised.

The population starts in G1, then progresses through each phase, until division occurs after the M phase. If at any point a cell has no open adjacent spaces, then it enters G0. The overshoot of G1 after days 2, 3, 4 and 5, is a result of cells entering G1 that then exit the cell cycle to G0 when no adjacent space is available.

A more realistic scenario would incorporate variability in the lengths of each cell cycle, since there will be differences in the lengths of phases in a heterogeneous population of cells. This can be simulated by drawing a random number of hours from a Poisson distribution every time a cell transitions into a new phase. The Poisson distributions were defined with λ equal to the cell phase durations that were previously defined. The resulting percentage of cells in each phase over time is seen in Figure 3.15.

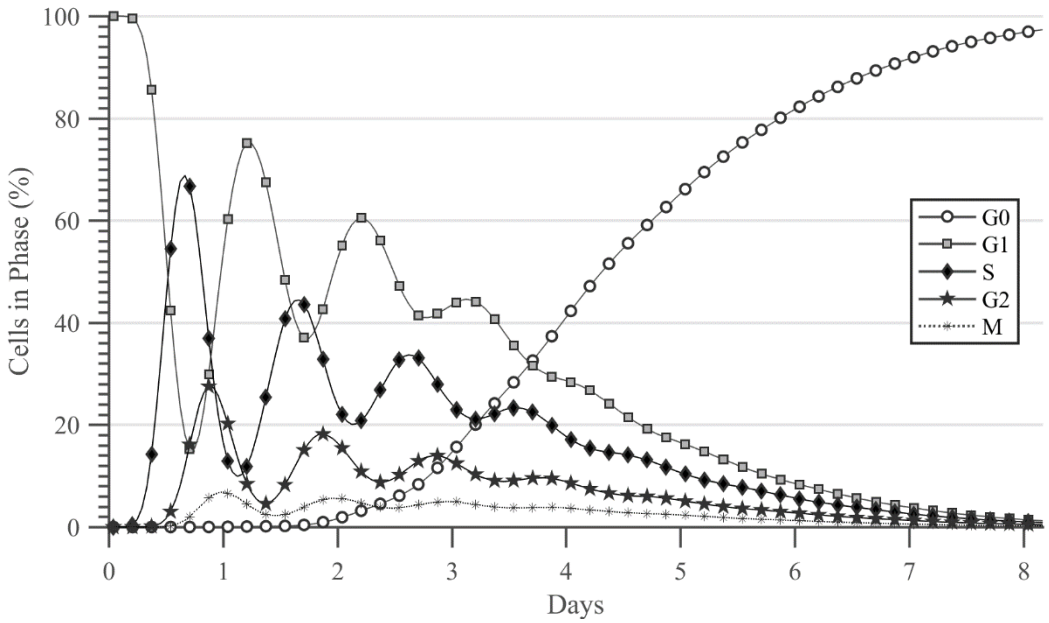

Figure 3.15. The percentage of cells in each cell cycle phase over time, when the duration of each cell cycle phase is drawn from Poisson distributions of $\lambda_{G1} = 11$, $\lambda_S = 8$, $\lambda_{G2} = 4$, and $\lambda_M = 1$.

As seen in Figure 3.16, the cyclical nature of the cell cycle phases still remains in the form of sinusoidal components in the G1, S, G2 and M phases, with a period equal to the division time. The percentage of cells in G0 is only influenced by space constraints and does not contain any sinusoidal components.

3.5.3 Lag phase

Seeded ASCs require time to adhere to the substrate, and remain in a latent lag period where no proliferation occurs. Most adherent cells remain in lag periods of between 12 and 24 hours [61], while ASC lag periods of less than a day [54] and nearly 3 days [34] have been reported.

Initially it could be assumed that during the lag period each cell exists in an undefined cell phase until it attaches to the substrate. The adherence of cells to the substrate can be modelled as a Poisson process, where a fixed rate of λ cells adhere each hour. Once attached to the substrate, cells exit the undefined phase and enter the G1 phase. Figure 3.16 (a) shows the percentage of cells in each phase, after adhering through a Poisson process with $\lambda = 20$.

It is important to note that cells do not only adhere during the lag period, but also need to recover from trypsinisation and spread out on the substrate [61]. A simplified model of this process could assume that each cell is equally likely to enter the cell cycle at any hour during the lag period. Such a process is shown in Figure 3.16 (b) for a lag period of 24 hours.

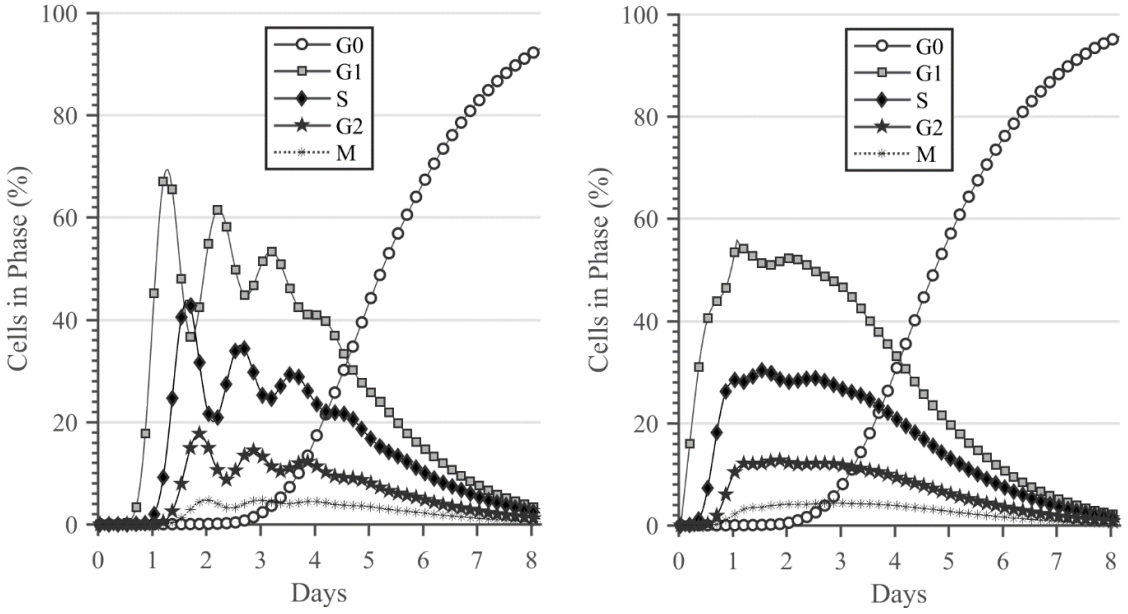

Figure 3.16. The percentage of the cell population in each cell cycle phase over time, when (a) a Poisson process, and (b) a uniform random process is used to model cells exiting the lag period. Adhering cells were modelled as an undefined phase until they re-entered the cell cycle.

Barring intentional intervention through physical or chemical means, cell cycles *in vitro* are typically not synchronised. An undefined phase during the lag period is a simplified assumption, and instead cells typically remain in the phase they were in when dissociated into suspension, i.e. when cells have reached the desired confluency. Considering that cells are usually dissociated at 80% confluency, the proportion of cells in each phase at approximately 4.5 days on Figure 3.15 were used as an initial approximation. The cell cycle phases of a uniform random process, through which each cell is equally likely to exit the lag period at any hour in a lag period of 24 hours, is shown in Figure 3.17.

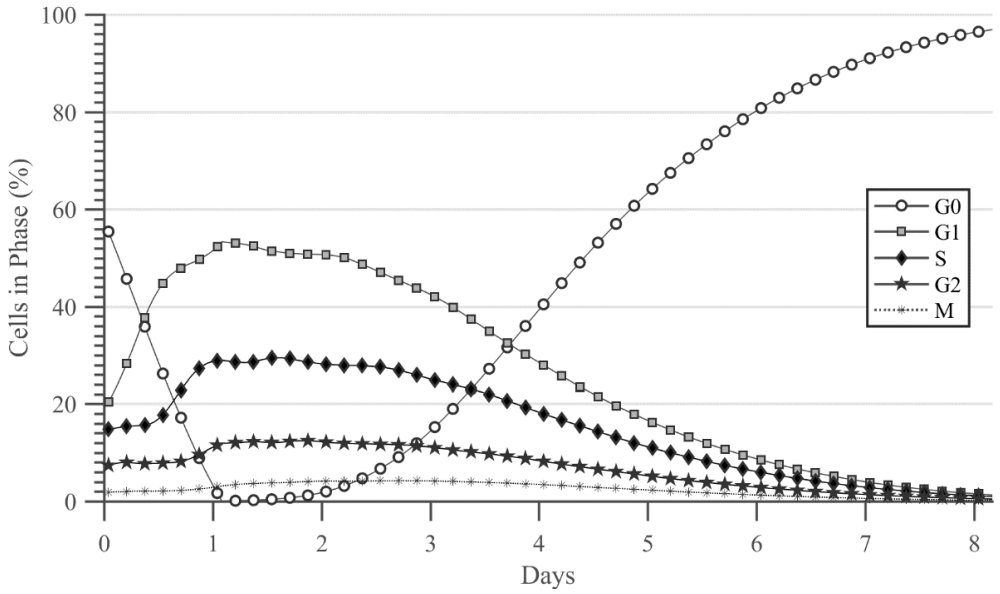

Figure 3.17. The percentage of cells in each cell cycle phase over time, when they have been initialised with approximately the proportions of cells in each phase at 80% confluency. The time when each cell exits the lag period was modelled as a uniform random process during the hours of the lag period, which was defined as 24 hours.

3.5.4 Subpopulations

Division time was modelled as constant for all cells in Sections 3.5.3 and 3.5.2. In contrast, bi-modal division time distributions have been observed in MSCs [62], which could indicate that subpopulations may also exist in ASCs. The division times of each subpopulation can be modelled by a Gaussian distribution, with a different mean for each subpopulation. The case of two subpopulations that were seeded at equal proportions, one with a mean division time of 12 hours, and another with a division time of 24 hours is shown in Figure 3.18.

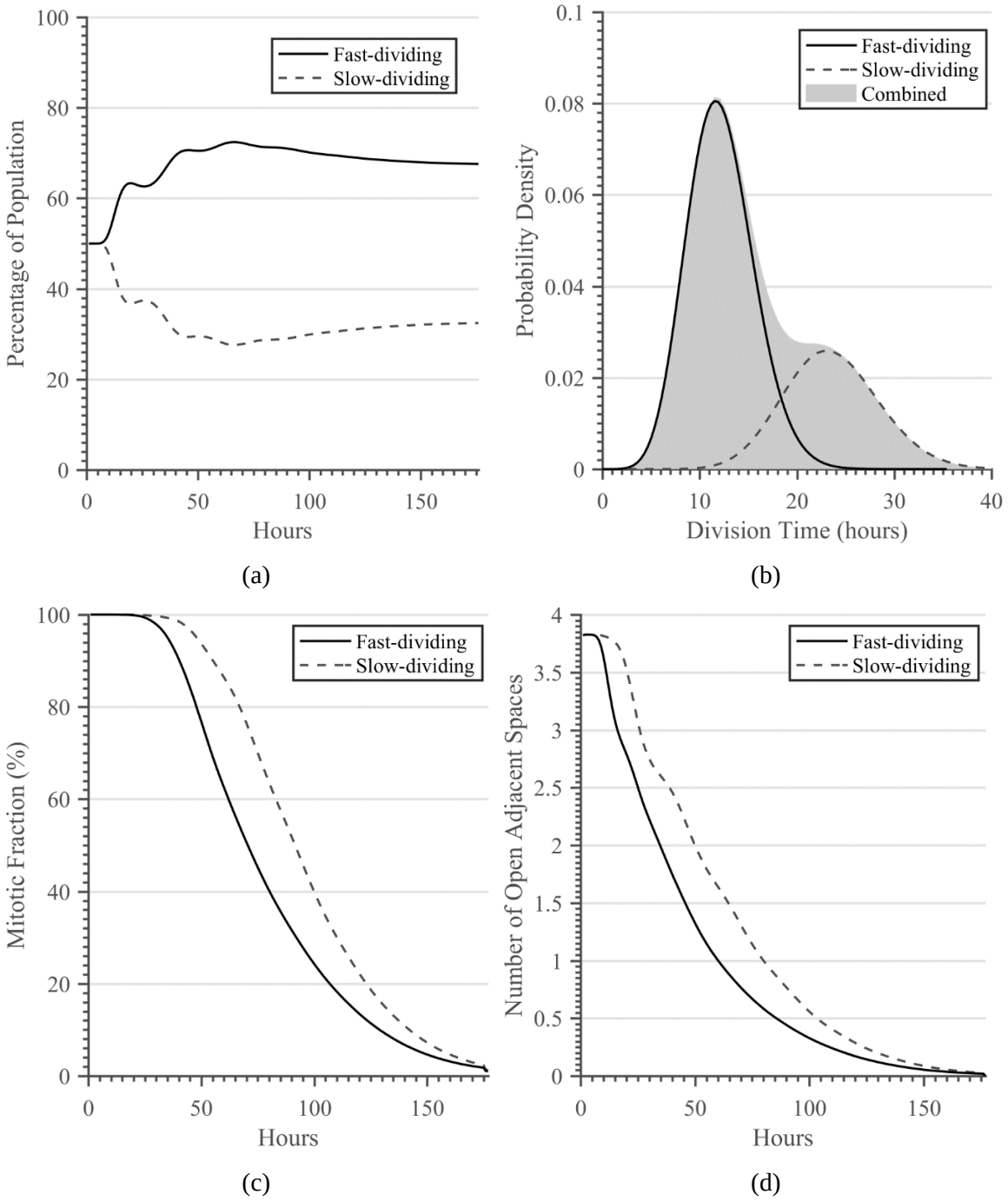

Figure 3.18. The effect of a bi-modal division time distribution on proliferation dynamics, when fast and slow-dividing populations were seeded at equal proportions, and no migration was allowed prior to division. (a) The percentage of the population that consists of each subpopulation. (b) A probability density estimate of the division times for the population when confluent. (c) The mitotic fraction of each subpopulation. (d) The number of open adjacent spaces for each subpopulation.

The subpopulation that divided faster attained an immediate advantage, and reached a maximum percentage of 72% of the population after 66 hours. However, this then decreased to 67.6% when the matrix was fully confluent after 177 hours. As seen in Figure 3.18 (c), the faster-dividing subpopulation initially had a larger mitotic fraction, but after 44 hours the slower-dividing subpopulation surpassed it. Considering that neither of the subpopulations were allowed to migrate, this could be explained by the faster-dividing subpopulation reaching a higher localised index of dispersion. As defined in (3.9), spatial dispersion is a summary measure for an entire matrix, and cannot discriminate between subpopulations. Instead, the number of open adjacent spaces was calculated to investigate a local measure of dispersion for each subpopulation, as seen in Figure 3.18 (d). The faster-dividing subpopulation reaches a mean of less than one open adjacent space after 60 hours, while the slower-dividing subpopulation only reaches this threshold after 80 hours. However, a faster division time, even at a lower mitotic fraction from 24 hours onwards, still provided a greater benefit, and the faster-dividing subpopulation occupied two-thirds of the available space when fully confluent.

Heterogeneity also exists in the motility of ASCs and the number of migratory cells in a population [85], [86]. This can be simulated by seeding migratory and non-migratory subpopulations at equal proportions. The population dynamics of this scenario is shown in Figure 3.19, where a migratory subpopulation was allowed to migrate every 4 hours if no division occurred at that time point.

As seen in Figure 3.19 (a), initially, the migrating subpopulation gained no advantage, owing to the abundant space that is available at low confluencies of less than 20%, which can be seen in Figure 3.19 (b). After 60 hours, the migratory subpopulation started to occupy a larger percentage of the matrix, and this percentage increased until the matrix was fully confluent, when 65.3% of all cells were migratory. As seen in Figure 3.19 (c), the mitotic fraction of both subpopulations remained equal until approximately 45 hours, after which the migrating subpopulation sustained a higher mitotic fraction until the matrix was fully confluent. The number of open adjacent spaces remain higher for migrating cells, and even increased between 29 and 37 hours, as seen in Figure 3.19 (d).

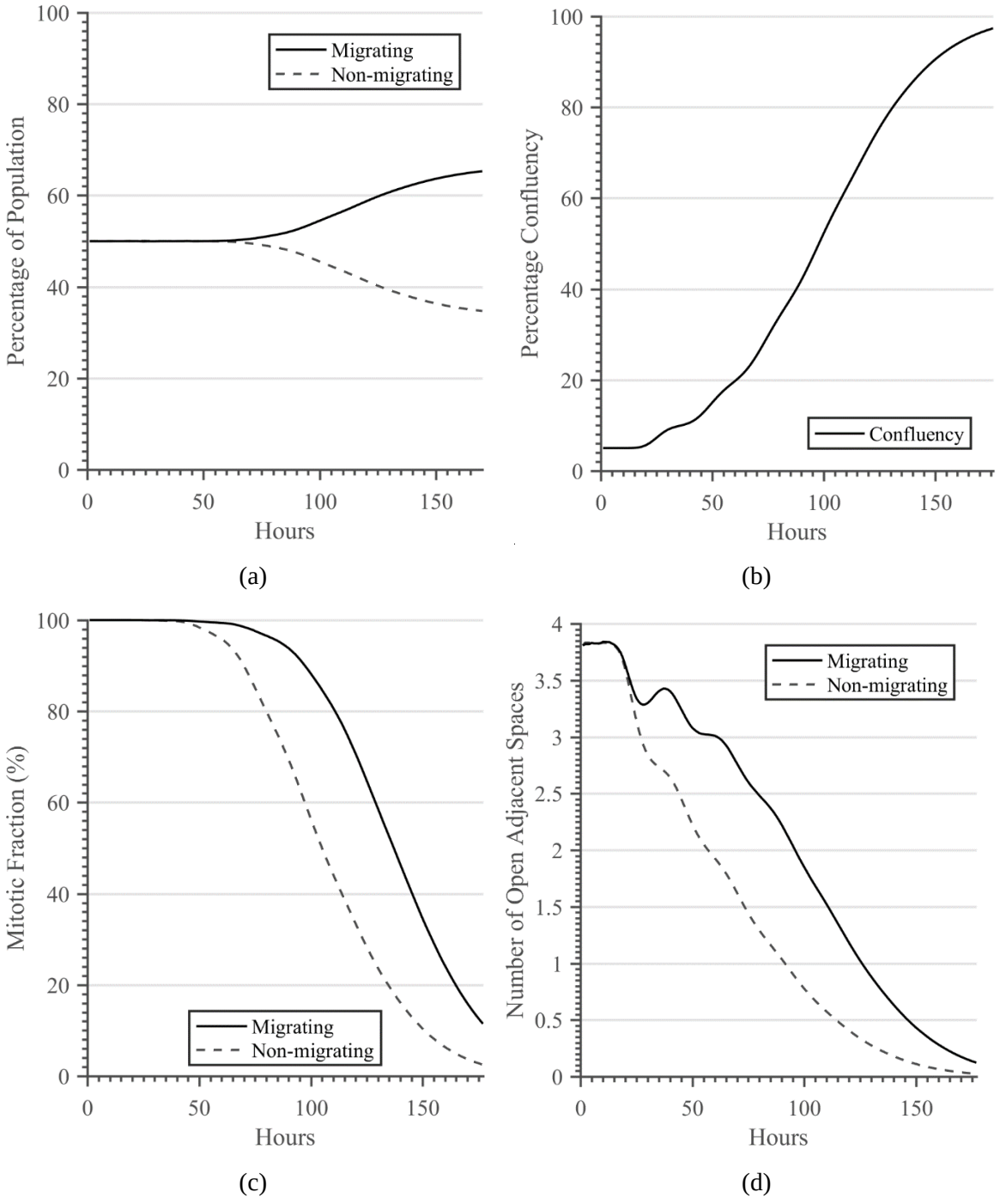

Figure 3.19. The effect of a migrating (at 4-hour intervals) and a non-migrating subpopulation on proliferation dynamics, when both subpopulations are seeded at equal proportions. (a) The percentage of the total population of each subpopulation over time. (b) The percentage confluency of the combined population. (c) The mitotic fraction of each subpopulation. (d) The number of open adjacent spaces for each subpopulation.

3.6 CHAPTER SUMMARY

A reductionist cellular automata model was implemented, where space-constraints were the only factor that determined whether a cell would divide. The model was generalised to be independent of the cell count and matrix size, by defining it in terms of confluency.

The model output was further generalised to be independent of epochs, by considering the mitotic fraction as a function of confluency. First, the case of a single epoch at various seeded confluencies was considered, which represented the maximum attainable mitotic fraction for a certain confluency. Different seeded confluencies were then considered across multiple cycles until fully confluent. The seeded confluency had an important effect on the mitotic fraction: lower seeded confluencies resulted in reduced mitotic fractions. Migration was then considered, which increased the mitotic fraction, and approached the single epoch maxima for a given confluency when migration was further increased.

The effect of both the seeded confluency and migration was then summarised by calculating a measure of spatial dispersion. The index of dispersion describes the relative grouping of cells on the matrix; a higher index is associated with cells that are more clumped together, which limits proliferation. When spatial dispersion and confluency were both known, the mitotic fraction could be estimated independently from migration and seeded confluency.

The model was converted to the time-domain by incorporating a static division time per epoch. Cell cycles were computed within each division time, initially as determinate intervals, then as random processes that were sampled from Poisson distributions. The effect of a lag period, during which newly seeded cells adhere to the substrate and prepare for division, was investigated for different assumptions.

The interaction between subpopulations with different characteristics was investigated. Fast- and slow-dividing subpopulations were considered, and it was found that initially the faster-dividing subpopulation commanded a larger percentage of the total population, but then decreased as confluency increased. This was a result of self-limiting of the faster-dividing population that, without migration, resulted in a reduced mitotic fraction. Next, a migrating

and non-migrating set of subpopulations were investigated. In the first 60 hours, migration provided no advantage. However, the number of open adjacent cells then remained higher for the migrating subpopulation, which resulted in a higher mitotic fraction and a higher proportion of the total population.

It should be noted that although complex interactions were simulated, the model makes significant assumptions, and the model variables differ from their real-world counterparts. Confluency, when defined as a fraction of the population limit, is only valid if it is assumed that each cell occupies the same surface area. Similarly, the seeded confluency can only be translated to seeding density for a constant and known cell size.

Apoptosis was simulated as a random process that occurs during every epoch, and apoptotic cells were removed immediately from the matrix. In contrast, apoptosis *in vitro* does not occur instantly, and is a process that takes 12 to 24 hours [87]. Apoptotic cells would not only exit the cell cycle, and be removed from the population, but would also occupy space and prevent other cells from dividing during that time.

CHAPTER 4 POPULATION MODEL

4.1 CHAPTER OBJECTIVES

Agent-based models cannot be readily applied to estimation and prediction when supplied with sequential observations of a system. In contrast, mathematical models of dynamic systems allow the propagation of the system state and can incorporate new observations to improve state estimation.

The objective of this chapter is to derive a population model with biologically-relevant variables, and to compare the model to the cellular automata simulations of Chapter 3. The population model should not require the modelling of individual cells.

4.2 FIRST-PRINCIPLES POPULATION MODEL

If a population of N_0 cells are seeded, then according to the Sherley model [88] the number of cells after one cell cycle (N_1) is equal to the sum of the fraction that did not divide, and twice the fraction that divided, i.e.

$$N_1 = (1-\alpha)N_0 + (2\alpha)N_0, \tag{4.1}$$

where α is the fraction of the population that divided during that cycle (i.e. the mitotic fraction). Only cells that divided in the previous cycle are considered for subsequent division; therefore, after two cycles,

$$N_2 = (1-\alpha)N_0 + (1-\alpha)(2\alpha)N_0 + (2\alpha)(2\alpha)N_0. \tag{4.2}$$

More generally, after x cycles,

$$N_x = (1-\alpha)(2\alpha)^0 N_0 + (1-\alpha)(2\alpha)^1 N_0 + \cdots + (1-\alpha)(2\alpha)^{x-1} N_0 + (2\alpha)^x N_0. \quad (4.3)$$

The series simplifies to

$$N_x = N_0[0.5 + 0.5\sum_{n=0}^{x}(2\alpha)^n]. \quad (4.4)$$

Assuming a constant α, a constant division time (DT), and by applying the following geometric identity [3]

$$b\sum_{n=0}^{x} y^n = b\frac{1-y^{x+1}}{1-y}, \quad (4.5)$$

the Sherley model is derived as

$$N(t) = N_0\left[0.5 + \frac{1-(2\alpha)^{\frac{t}{DT}+1}}{2(1-2\alpha)}\right], \quad (4.6)$$

where $N(t)$ represents the number of cells at a given time t. It should be noted that an asymptote is introduced at $\alpha = 0.5$ by the geometric identity defined in (4.5). Without the introduction of the asymptote, $\alpha = 0.5$ results in linear growth.

The Sherley model, simulated for several constant mitotic fractions, is shown in Figure 4.1. As seen in Figure 4.1, when $\alpha < 0.5$ the model results in exponential growth, while $\alpha > 0.5$ results in logarithmically increasing growth. Therefore, the model cannot describe both early exponential growth, and later slowing of growth when a saturation point is approached.

It is important to note that (4.3) implies that cells that are part of the non-mitotic fraction in any cycle will never divide in any subsequent cycles; thus, non-dividing cells are seen as senescent or terminally differentiated. Therefore, the Sherley model does not allow cells to enter a quiescent state temporarily.

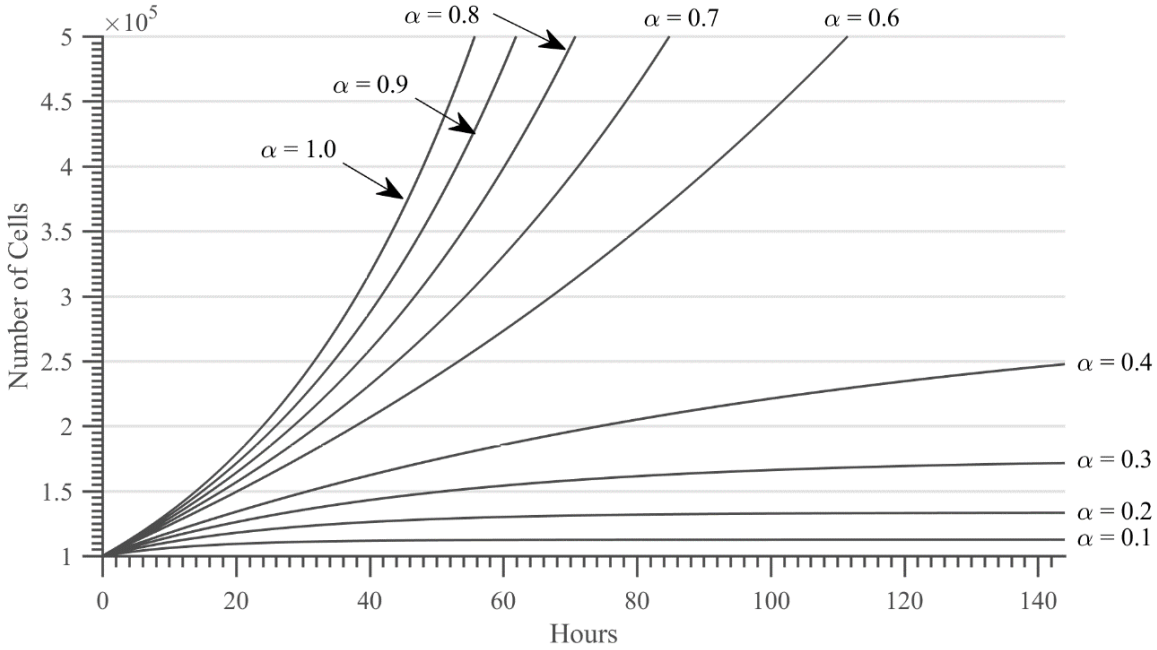

Figure 4.1. The number of cells per hour simulated with the Sherley model and $N_0 = 10^4$, a constant $DT = 24$ hours, and constant mitotic fractions between 0.1 and 1.0. The size of the seeded population and the division time do not affect the curve shape.

4.3 MARKOV POPULATION MODEL

Instead of assuming that the non-mitotic fraction will never divide again, a Markov assumption can be made; i.e. it can be assumed that the population has no memory beyond the previous cell cycle. This is reasonable, since cells that were temporarily in a quiescent state may re-enter the cell cycle if space, nutrients, or other limited resources become available. The first cycle remains

$$N_1 = (1 - \alpha)N_0 + (2\alpha)N_0. \tag{4.7}$$

However, during the second cycle, the *entire* colony is again considered as available to divide, i.e.

$$N_2 = (1 - \alpha)N_1 + (2\alpha)N_1. \tag{4.8}$$

As demonstrated in Chapter 3, owing to space constraints, the mitotic fraction is not constant. Therefore, more generally, for any cell cycle $x + 1$,

$$N_{x+1} = (1 - \alpha_x)N_x + (2\alpha_x)N_x. \quad (4.9)$$

This simplifies to the Markov population model

$$N_{x+1} = (1 + \alpha_x)N_x. \quad (4.10)$$

(4.10) has not been previously described in the literature, and provides a new approach to modelling proliferation.

If, as in the Sherley model, a constant α is assumed, the model reduces to

$$N_x = (1 + \alpha)^x N_{0.} \quad (4.11)$$

Therefore, for a constant α, the model is exponentially increasing for all $\alpha > 0$. And when the entire population is mitotically active, i.e. $\alpha = 1$, the model results in the well-known exponential biological growth function,

$$N_x = 2^x N_0. \quad (4.12)$$

4.4 MODELLING THE MITOTIC FRACTION

As shown in (4.11), a constant α results in an exponentially increasing function that does not incorporate the slowing of growth as a saturation point is reached; therefore, α needs to be modelled as cycle-varying. The following sections use the cellular automata simulations of Section 3.4.3 as the measure of success. Although a time-varying mitotic fraction has been suggested by [6], the mitotic fraction has not been explicitly modelled in the literature.

4.4.1 Verhulst mitotic fraction

A well-known biologically-relevant growth model, the Verhulst equation [74], is defined as

$$N(t) = \frac{KN_0e^{rt}}{K + N_0(e^{rt} - 1)}. \quad (4.13)$$

It is described by the differential equation,

$$\frac{dN}{dt} = rN\left(1 - \frac{N}{K}\right), \tag{4.14}$$

where K is the population limit

$$\lim_{t\to\infty} N(t) = K, \tag{4.15}$$

and r is the intrinsic growth rate; i.e. the growth rate when there are no constraints on growth. If $r = 1$, it implies that when sufficient space and nutrients are available, all cells are mitotically active and double after every cell cycle.

The Taylor series of a function $f(x)$ at x_0 is defined as [89]

$$\begin{aligned} f(x) = f(x_0) + \frac{f'(x_0)}{1!}(x - x_0) + \frac{f''(x_0)}{2!}(x - x_0)^2 \\ + \frac{f'''(x_0)}{3!}(x - x_0)^3 + \cdots, \end{aligned} \tag{4.16}$$

where f' denotes the first derivative, f'' the second derivative, and so forth. Using the first two terms of (4.16) as a first-order discrete approximation of a function f, then

$$f(x_0 + \Delta t) = f(x_0) + \Delta t\, f'(x_0). \tag{4.17}$$

Therefore, a first-order discrete approximation of (4.13), for cycles $x \in \mathbb{N}_0$, is given by

$$N_{x+1} = N_x + N_x r\left(1 - \frac{N_x}{K}\right). \tag{4.18}$$

Equating (4.18) to (4.10), the Verhulst mitotic fraction is derived as

$$\alpha_x = r\left(1 - \frac{N_x}{K}\right). \tag{4.19}$$

It is assumed that

- $K \in \mathbb{N}$, i.e. the population limit is a positive integer,
- the number of cells cannot exceed the population limit, i.e. $N_x \in [0, K]$, and
- the intrinsic growth rate and the mitotic fraction are positive fractions, i.e. $r \in [0, 1]$ and $\alpha_x \in [0, 1]$, by definition (i.e. a fraction cannot be less than 0% or exceed 100%).

Substituting (3.7) into (4.19) results in α_x as a function of the confluency, γ_x, i.e.

$$\alpha_x = r(1 - \gamma_x). \tag{4.20}$$

The Verhulst mitotic fraction as a function of confluency is depicted at various values of r in Figure 4.2, and is compared to the range of mitotic fractions that were realised with the cellular automata simulations of Section 3.4.3.

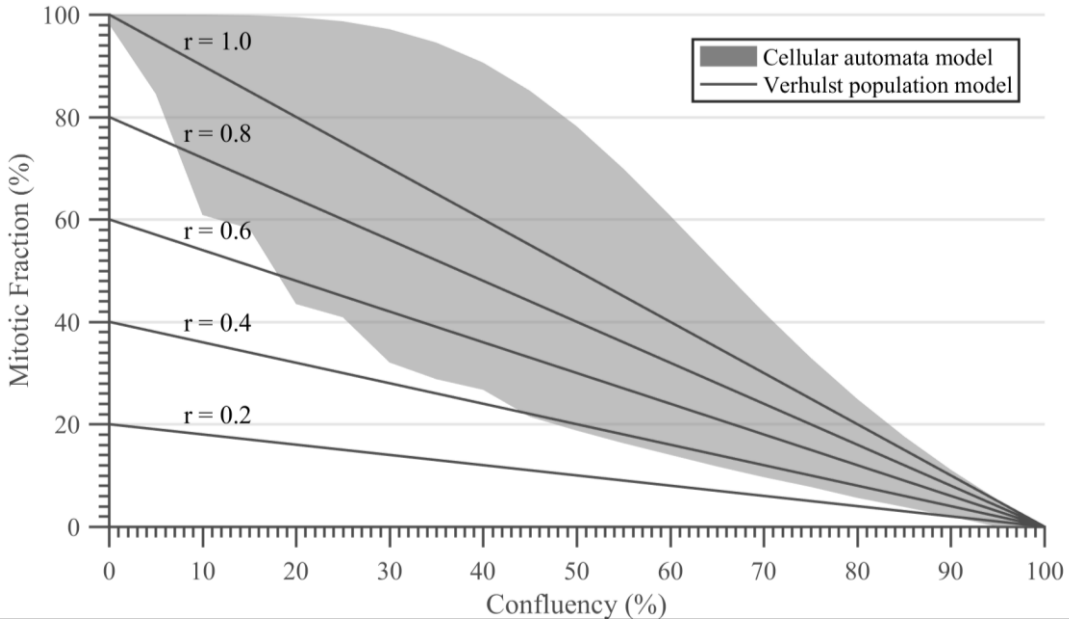

Figure 4.2. The Verhulst mitotic fraction compared cellular automata and the at various r values. Cellular automata were seeded at confluencies between 0.1% and 99.9%, and allowed to migrate between zero and five times per cycle, as described in Section 3.4.3.

Assuming a known N_0 and K, the Verhulst mitotic fraction and resulting confluencies are compared to cellular automata, at various seeded confluencies, in Figure 4.3.

The root-mean-square error (RMSE), which is a measure of the difference between predicted and true values, was used as a measure of accuracy. The RMSE of the Verhulst mitotic fraction and resulting confluencies at various seeded confluencies are shown in Table 4.1.

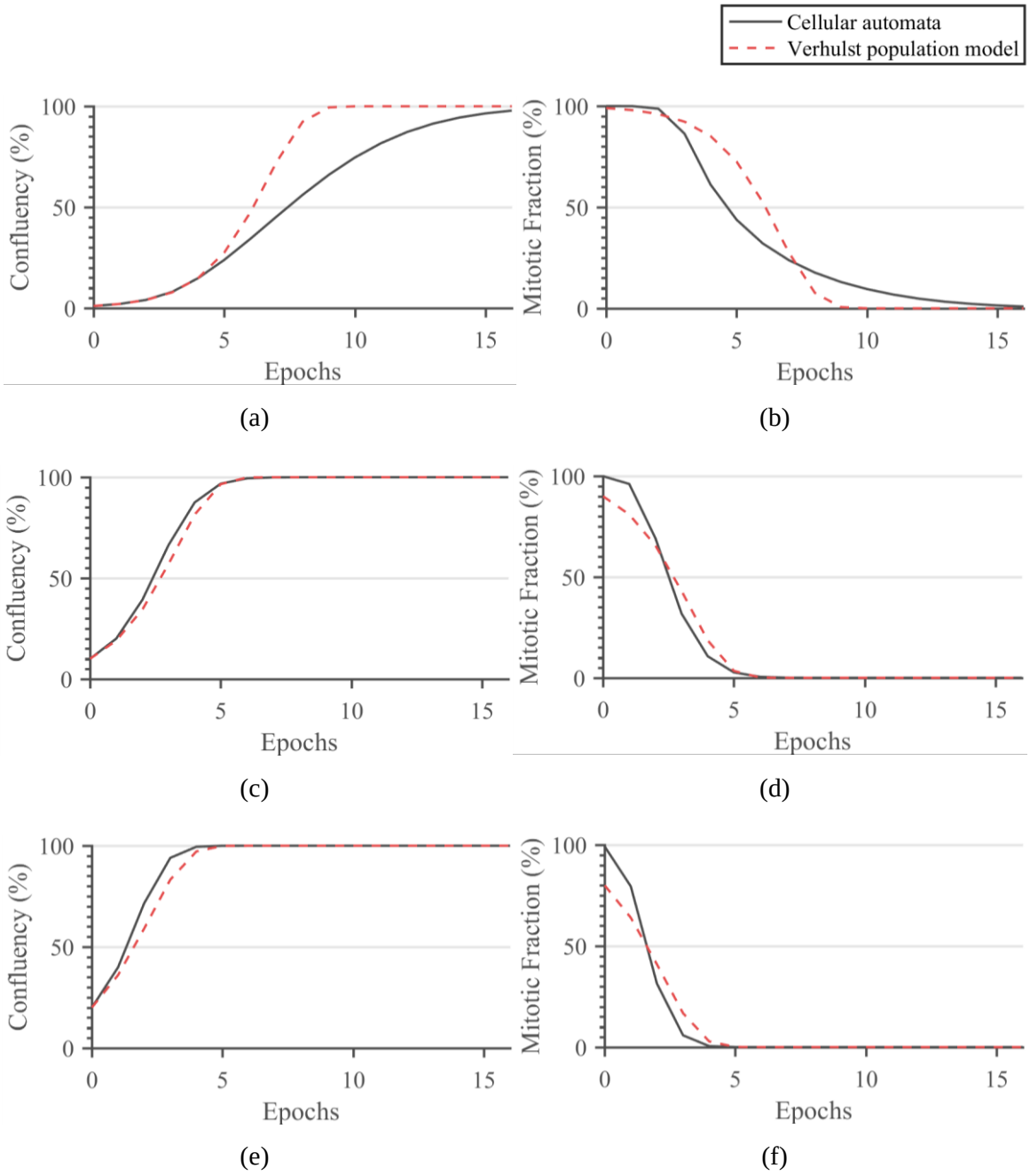

Figure 4.3. Comparing confluency (left) and the mitotic fraction (right) between cellular automata and the Verhulst mitotic fraction model, seeded at different confluencies in each row. Cells were seeded at confluencies of (a) - (b) 1%, (c) - (d) 10%, and (e) - (f) 20%. In all simulations $K = 10^6$, and no migration was allowed for the cellular automata. The Verhulst model was set at $r = 1$.

Table 4.1 The RMSE of confluency and the mitotic fraction for various seeded confluencies, when using the Verhulst mitotic fraction model to predict cellular automata.

Seeded Confluency	RMSE Confluency	RMSE Mitotic Fraction
1%	12.8314	9.0906
10%	4.3206	8.1301
20%	6.9774	11.7361
50%	7.1703	14.5930

As seen in Figure 4.3 (b), the model overestimates the mitotic fraction of populations that are limited by cells at low seeding densities; and conversely, as seen in Figures 4.3 (d) and (f), the mitotic fraction of cells seeded at higher densities are initially underestimated.

The Verhulst mitotic fraction assumes that the mitotic fraction is only a function of confluency. As demonstrated in Chapter 3, this is not the case, and the mitotic fraction depends on the seeded confluency as well as migration, both of which can be summarised by a measure of spatial dispersion.

4.4.2 Generalised logistic mitotic fraction

A generalised logistic differential equation [79], which is defined by the differential equation,

$$\frac{dN}{dt} = rN^{\rho}\left[1 - \left(\frac{N}{K}\right)^{\beta}\right]^{\phi}, \tag{4.21}$$

provides additional parameters to describe population growth. A wide variety of biological growth models can be derived from (4.21), including the Gompertz, Weibull, and Richards equations [79]. N represents the total number of cells and is initialised by the initial seeding population N_0. Similarly to the Verhulst model, K represents the population limit and r represents the intrinsic growth rate. The additional parameters ρ, β and ϕ have no defined biological meaning.

A first-order discrete approximation, again using (4.17), for the function defined in (4.21), for cell cycles $x \in \mathbb{N}_0$, is given by

$$N_{x+1} = N_x + rN_x{}^{\rho}\left[1 - \left(\frac{N_x}{K}\right)^{\beta}\right]^{\phi}. \tag{4.22}$$

Equating (4.22) to (4.10), the mitotic fraction can be calculated as,

$$\alpha_x = rN_x{}^{\rho-1}\left[1 - \left(\frac{N_x}{K}\right)^{\beta}\right]^{\phi}. \tag{4.23}$$

It should be noted that for $\rho = \phi = \beta = 1$, the generalised logistic mitotic fraction results in the Verhulst mitotic fraction.

The first factor, $N_x{}^{\rho-1}$, is not dependent on the saturation point K, but only on the absolute number of cells. For $\rho < 1$, an exponentially decaying factor is introduced that quickly approaches an asymptote as the number of cells increase, while $\rho > 1$ results in logarithmic growth that increases as the number of cells increase. It is unlikely that a factor that is directly dependent on the number of cells would have an effect on the mitotic fraction; therefore, it is assumed that $\rho = 1$. Additionally, if confluency is again defined as γ_x, then (4.23) becomes

$$\alpha_x = \left[1 - \gamma_x{}^{\beta}\right]^{\phi}. \tag{4.24}$$

Given that $\gamma_x \in [0, 1]$, it is of specific interest when $\beta \in [0, \infty)$ and $\phi \in [0, \infty)$, since that would imply that $\alpha_x \in [0, 1]$.

The curves of the upper and lower bounds of mitotic fractions of the cellular automata simulations were fitted to (4.24) using least squares approximation, and the results are summarised in Table 4.2. The parameter ϕ was set as a constant to simplify the resulting equation, and a comparable RMSE was found when $\phi = 2$.

The generalised logistic mitotic fraction, as a function of confluency, is depicted for $\phi = 2$ and β between 0.8 and 3 in Figure 4.4, and is compared to the range of mitotic fractions realised during the cellular automata simulations of Section 3.4.3.

Table 4.2 The RMSE when the parameters of (4.24) are fitted to the upper and lower bound of the mitotic fractions obtained during cellular automata simulations. The RMSE describes the error in the mitotic fraction, and is therefore dimensionless. The fixed values column indicates whether ϕ was set to a fixed value of $\phi = 2$, or included as a fitted parameter.

Mitotic Fraction	Fixed Values	β	ϕ	RMSE
Upper Bound	None	3.077	2.016	0.01868
Upper Bound	$\phi = 2$	3.062	2.000	0.01822
Lower Bound	None	0.6207	1.602	0.02854
Lower Bound	$\phi = 2$	0.7423	2.000	0.03301

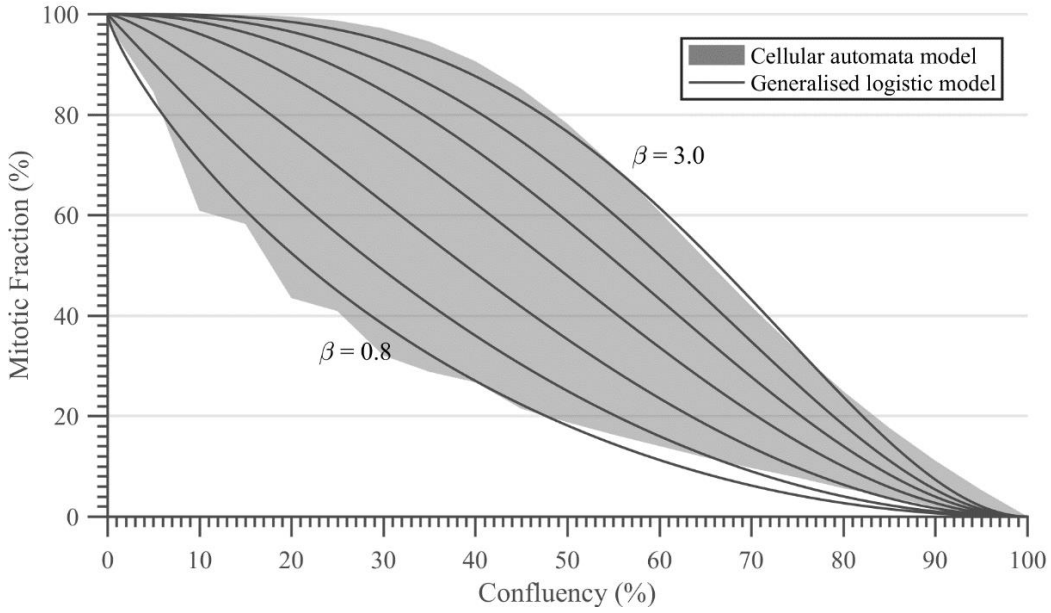

Figure 4.4. Comparing the mitotic fraction as a function of confluency for cellular automata and the generalised logistic mitotic fraction, with $\phi = 2$ and β varied between 0.8 and 3. Cellular automata were seeded at confluencies between 0.1% and 99.9%, and allowed to migrate between zero and five times per cycle, as described in Section 3.4.3.

When comparing Figure 4.4. to Figure 3.11, a similarity exists between the way that the index of dispersion (which was calculated for cellular automata), and the parameter β as defined in (4.24) influence the mitotic fraction. The relationship between the index of dispersion and β can be explored by calculating the value of β when the index of dispersion is known. Solving (4.24) for β results in

$$\beta = \log_\gamma(1 \pm \sqrt{\alpha}), \tag{4.25}$$

which yields a reflection of the function across the horizontal axis. Only $\beta \geq 0$ was considered to simplify the analysis, i.e.

$$\beta = \log_\gamma(1 - \sqrt{\alpha}). \tag{4.26}$$

The index of dispersion and the β that was calculated using (4.26), are shown for cellular automata seeded at 1% confluency in Figure 4.5 (a). As seen in Figure 4.5 (a), there is an inverse correlation between β and the index of dispersion. As shown in Figure 4.5 (b), when β is depicted as a function of the index of dispersion, the inverse relationship can be described by an exponential function. A least squares approximation of the exponential equation

$$\beta = aI^b, \tag{4.27}$$

where I is the index of dispersion, and a and b are fitted parameters, was performed, and is also shown in Figure 4.5 (b). The resulting fitted parameters are listed in Table 4.3.

Table 4.3 The fitted parameters for (4.27) that describe β as a function of the index of dispersion. The RMSE describes the error in β, and is therefore dimensionless.

$\boldsymbol{a}$	$\boldsymbol{b}$	**RMSE**
2.56	-0.5	0.09819

Therefore, when substituting the parameters in Table 4.3., then β can be calculated as

$$\beta = \frac{2.56}{\sqrt{I_x}}. \tag{4.28}$$

Substituting (4.28) into (4.22) results in the generalised logistic mitotic fraction as a function of confluency and the index of dispersion, i.e.

$$\alpha_x = \left[1 - \gamma_x^{\frac{2.56}{\sqrt{I_x}}}\right]^2. \tag{4.29}$$

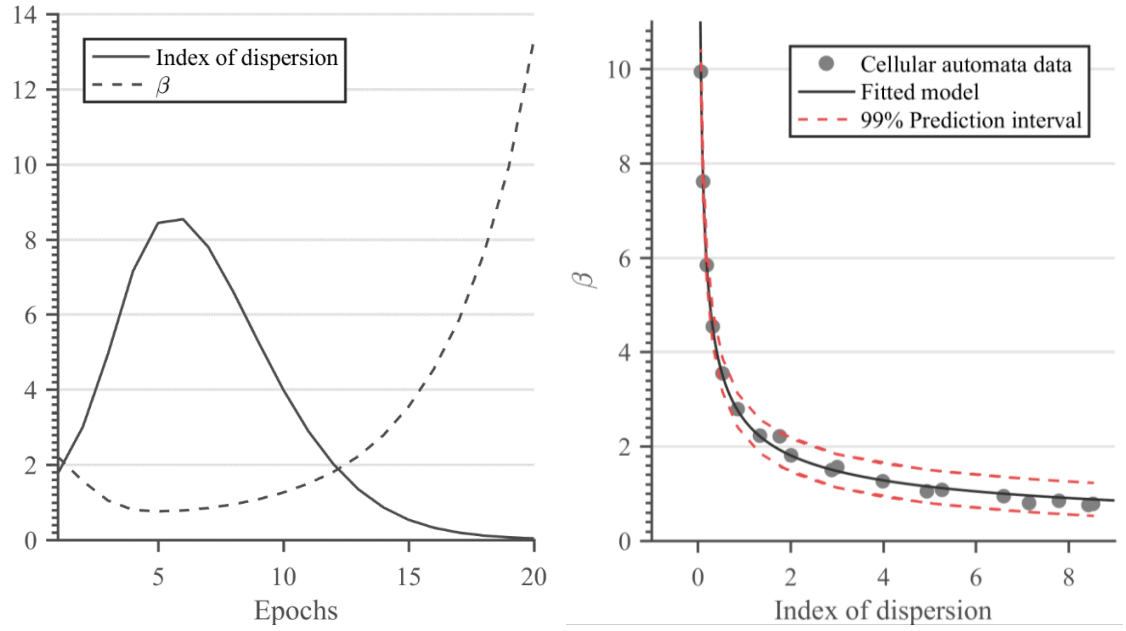

(a) (b)

Figure 4.5. (a) The measured index of dispersion, and β calculated using (4.23), shown for cellular automata seeded at 1% confluency and allowed to expand until confluency after 20 epochs. (b) A comparison between the fitted model described in (4.24) and the cellular automata data of 4.6 (a), for β as a function of the index of dispersion.

Assuming a known N_0, K, and I_x, the generalised logistic mitotic fraction and resulting confluencies are compared to cellular automata, at various seeded confluencies, in Figure 4.6. The corresponding RMSE of confluency and the mitotic fraction are summarised in Table 4.4.

Table 4.4 The RMSE of confluency and the mitotic fraction, when using the generalised logistic mitotic fraction model to predict the proliferation of cellular automata at various seeded confluencies.

Seeded Confluency	RMSE Confluency (%)	RMSE Mitotic Fraction (%)
1%	1.9534	2.2531
10%	1.6293	2.5551
20%	0.8311	1.6628
50%	2.5027	4.3157

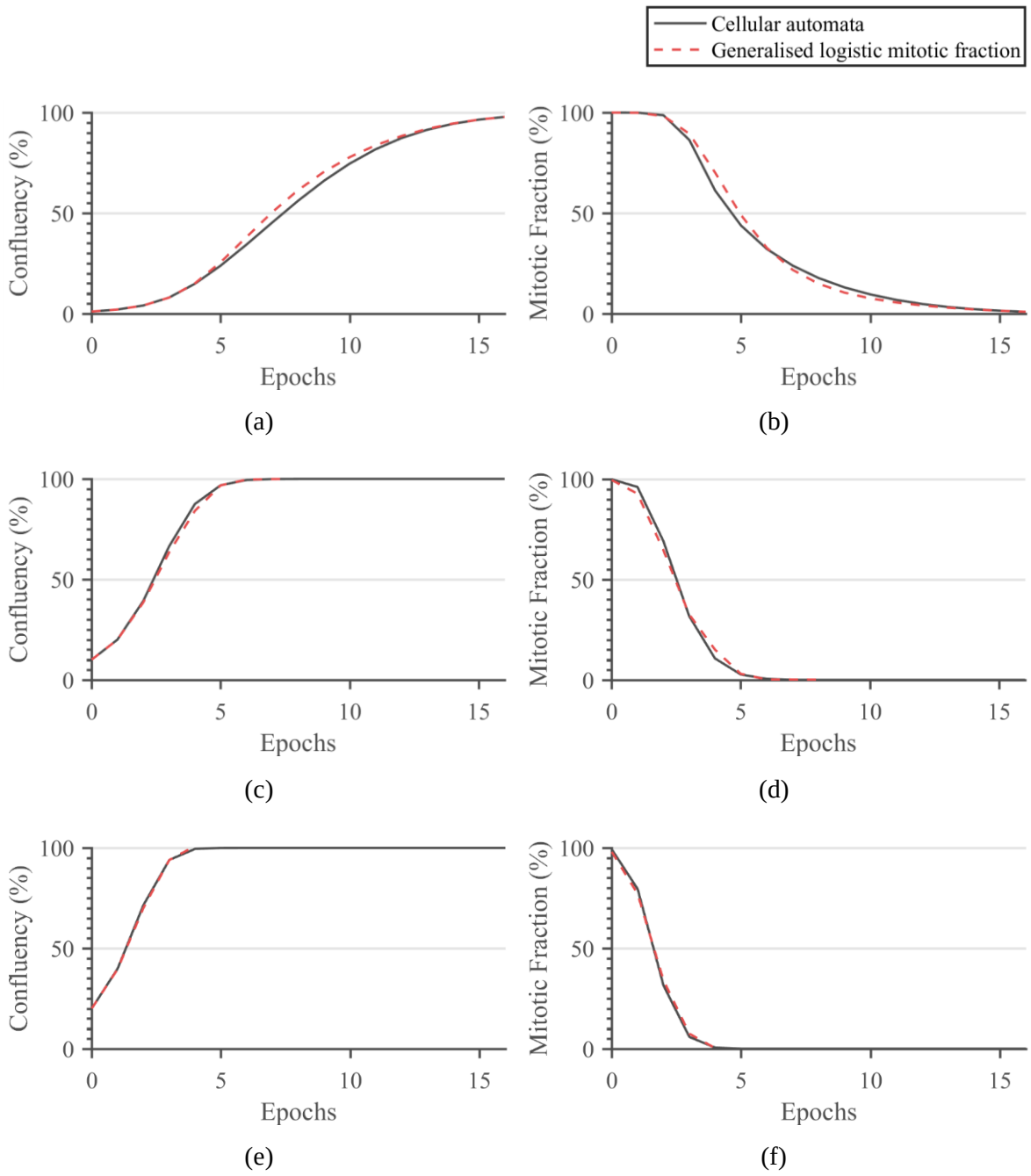

Figure 4.6. Comparing confluency (left) and the mitotic fraction (right) between cellular automata and the generalised logistic mitotic fraction model, seeded at different confluencies in each row. Cells were seeded at confluencies of (a) - (b) 1%, (c) - (d) 10%, and (e) - (f) 20%. In all simulations $K = 10^6$, and no migration was allowed for the cellular automata. The generalised logistic model was set at $\phi = 2$, and β was calculated using the measured index of dispersion.

4.4.3 Discussion

The RMSE of confluency and mitotic fraction for the Verhulst and generalised logistic mitotic fractions are shown in Figure 4.7.

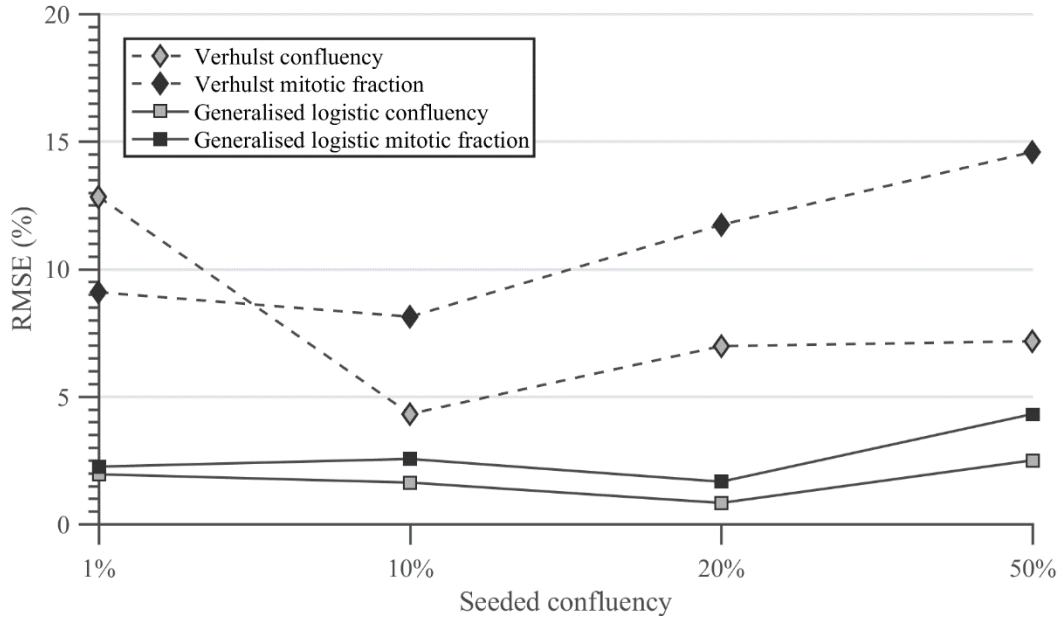

Figure 4.7. The RMSE of confluency and the mitotic fraction for the Verhulst and generalised logistic models predict cellular automata proliferation at various seeded confluencies.

The Verhulst model performed poorly at very low or high seeded confluencies, which suggests the importance of spatial dispersion. The generalised logistic model, which incorporated spatial dispersion, outperformed the Verhulst model at all seeded confluencies.

4.5 ADAPTING CELL CYCLES TO TIME

The cycles of cells are usually not synchronised, and the cell cycle of a population is usually not known. Therefore, if the cell population is described as a function of cell cycles, then practical applications of the model are limited. Modelling a population as a function of time can be more readily applied.

The population doubling time (PDT) is defined as [46]

$$PDT = (\mathrm{t}_2 - t_1)\log_{\frac{N_2}{N_1}} 2. \tag{4.30}$$

This is equal to the average division time of the individual cells that comprise the population, if it is assumed that *all* cells in the population are mitotically active. If the population is sampled every $\Delta\mathrm{t} = \mathrm{t}_2 - t_1$ then from (4.9), the number of cells as a result of division between samples x and $x + 1$, is

$$2\alpha_x N_x = N_{x+1} - (1 - \alpha_x)N_x. \tag{4.31}$$

The average division time (DT) of the mitotically active population can then be approximated as the PDT of only the mitotic fraction of the cells, i.e. $\alpha_x N_x$ dividing into $2\alpha_x N_x$. For sampling intervals $0 < \Delta t \leq DT$, and $\alpha_x > 0$,

$$DT = \Delta t.\log_{\left[\frac{N_{x+1}-(1-\alpha_x)N_x}{\alpha_x N_x}\right]} 2\,. \tag{4.32}$$

Solving for N_{x+1}, then

$$N_{x+1} = N_x\left(\alpha_x e^{\frac{\Delta t\, ln2}{DT}} - \alpha_x + 1\right). \tag{4.33}$$

Compared to (4.10), α_x is multiplied by a factor $(e^{\frac{\Delta t\, ln2}{DT}} - 1)$. Intuitively, when the sampling period is equal to the division time, i.e. $\Delta t = DT$, then (4.33) reduces to (4.10).

The approximation of confluency using (4.33) is shown in Figure 4.8 for different sampling periods, assuming a known N_0, K, DT and α_x.

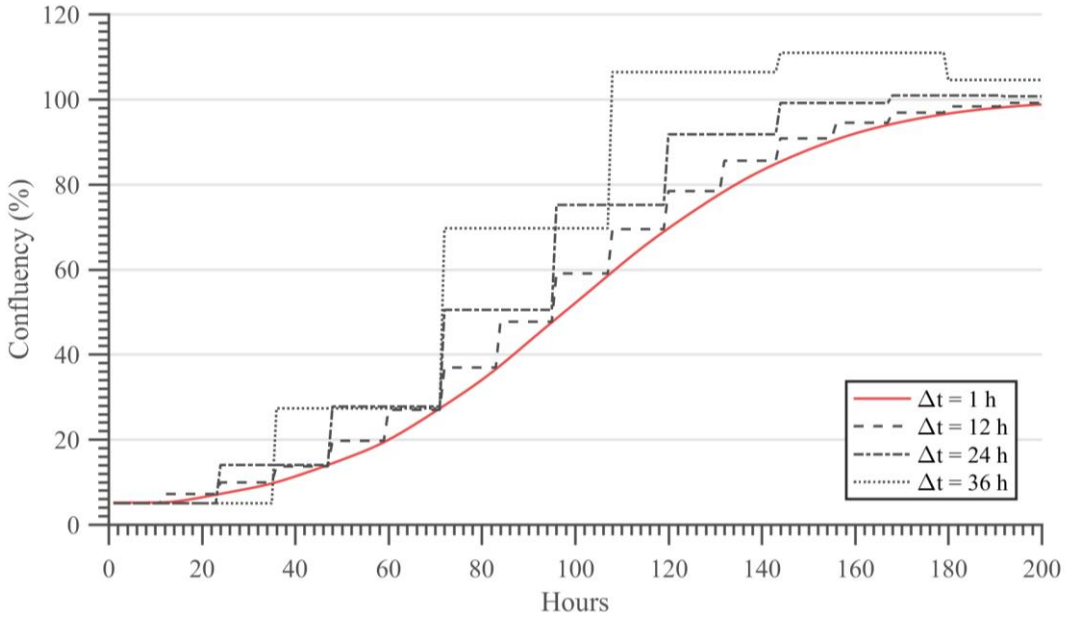

Figure 4.8. The time-domain approximation of confluency for different sampling periods, given a known N_0, DT and α_x. Cellular automata were simulated for $N_0 = 5 \times 10^4$, $K = 10^6$, and $DT = 24$.

The corresponding estimates of DT using (4.32) are shown in Figure 4.9. Initially, cells that form part of the mitotic fraction have not divided yet; therefore, when sampling at hourly intervals, initially

$$\frac{N_{x+1} - (1-\alpha_x)N_x}{\alpha_x N_x} \approx 1, \tag{4.34}$$

thus

$$\log_{\left[\frac{N_{x+1}-(1-\alpha_x)N_x}{\alpha_x N_x}\right]} 2 \to \infty. \tag{4.35}$$

It should also be noted that each estimate only uses the latest two measurements, and is therefore prone to errors, especially when growth begins to plateau. By including additional measurements into the estimate, accuracy could be improved; however, this is beyond the scope of this study, and could be investigated in future work.

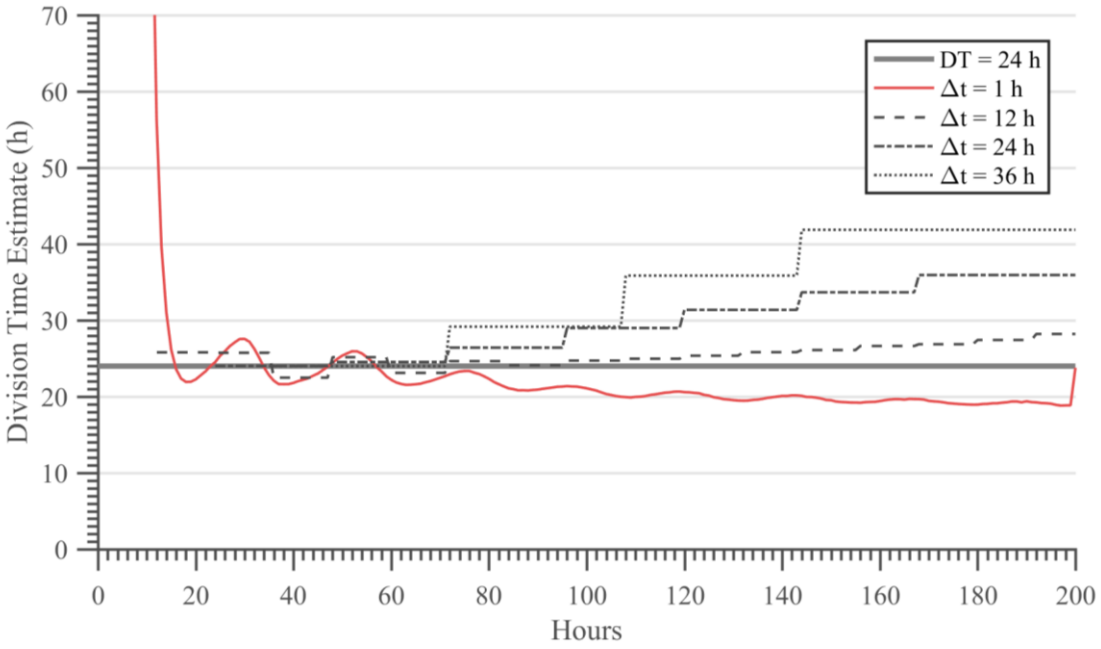

Figure 4.9. Estimates of division time for different sampling periods, given a known N_x and α_x. Cellular automata were simulated for $N_0 = 5 \times 10^4$, $K = 10^6$, and $DT = 24$.

4.6 MODELLING THE LAG PHASE

As discussed in Section 3.5.3, ASCs *in vitro* typically enter a lag phase directly after seeding, during which little or no division occurs while cells attach to the substrate. The lag phase can be modelled as a separate process that depends on the time since seeding. If ω_x represents the fraction of adhering cells at a certain interval, and assuming that the mitotic fraction is equally likely to adhere as other cells, then the *lag-phase adapted mitotic fraction* ($\widehat{\alpha_x}$) is

$$\widehat{\alpha_x} = \alpha_x - \omega_x \alpha_x. \tag{4.36}$$

One approach would be to model ω_x as an exponentially decaying function of time, then

$$\frac{d\omega}{dt} = -\frac{\omega}{\tau_{lag}}, \tag{4.37}$$

where τ_{lag} is the lag time constant, i.e. the time until $\frac{1}{e}$ cells have attached to the substrate. A first-order discrete approximation, again using (4.17), is given by

$$\omega_{x+1} = \omega_x - \frac{\Delta t}{\tau_{lag}}\omega_x. \tag{4.38}$$

It is assumed that $\omega_0 = 1$, i.e. all cells are adhering when seeded, and that $\tau_{lag} \geq \Delta t$. A realisation of the model for various τ_{lag} values is shown in Figure 4.10 (a).

The exponential decay function implies that more cells would adhere per time period initially, and the rate of decays slows as time progresses. Instead, it could be reasoned that cells take approximately the same amount of time to adhere, and that almost all cells adhere during a certain period after seeding. This could be modelled as an inverted sigmoidal function, described by the differential equation

$$\frac{d\omega}{dt} = \frac{-\xi\, e^{-\xi\,(t-t_{1/2})}}{\left(e^{-\xi\,(t-t_{1/2})}+1\right)^2}, \tag{4.39}$$

and first-order discrete approximation

$$\omega_{x+1} = \omega_x - \frac{\Delta t\, \xi\, e^{-\xi(t-t_{1/2})}}{\left(e^{-\xi\,(t-t_{1/2})}+1\right)^2}, \tag{4.40}$$

where ξ determines the steepness slope of the sigmoid, and $t_{1/2}$ determines the time when half of cells have attached. A realisation of the model for various $t_{1/2} = 24$ and various ξ values is shown in Figure 4.10 (b).

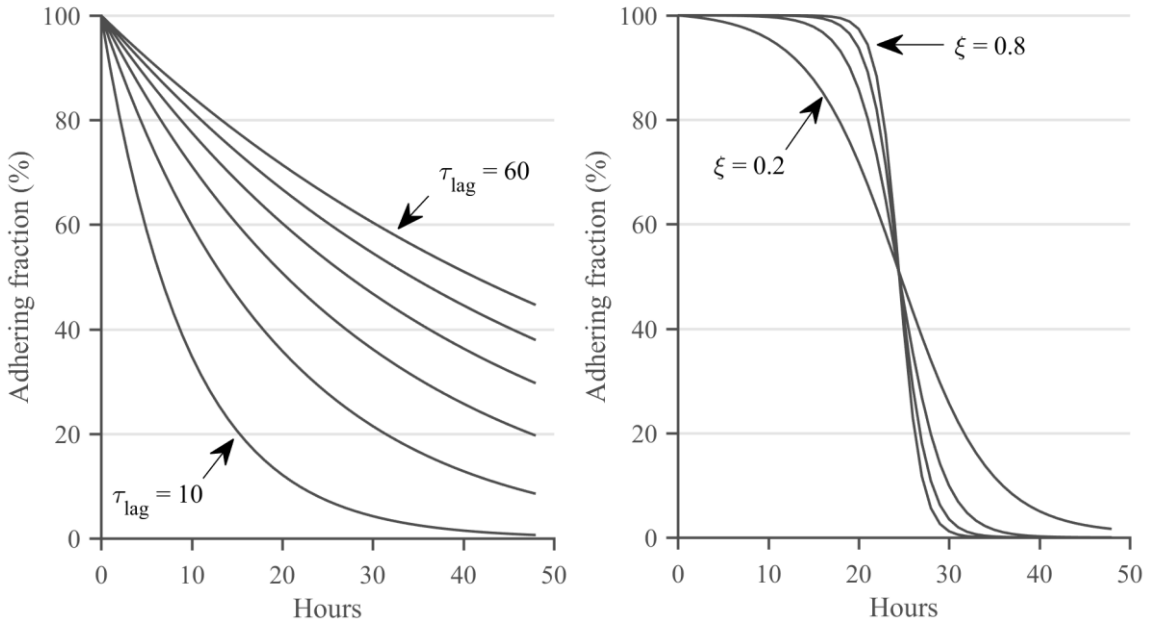

Figure 4.10. The fraction of cells that are adhering and in the lag phase, as modelled by (a) an exponential decay function with τ_{lag} between 10 and 60 hours, and (b) a sigmoidal function with ξ between 0.2 and 0.8.

4.7 CHAPTER SUMMARY

A Markov population model was derived from the first-principles Sherley model, by allowing cells to enter quiescent states that may later re-enter the cell cycle. The Markov population model describes the number of cells in a population as a function of cell cycles and the mitotic fraction; an approach that has not previously been described in the literature.

Initially, the mitotic fraction of the Markov population model was derived from the Verhulst model, and a linear relationship with confluency was found. The Verhulst mitotic fraction provided reasonable approximations for the cellular automata simulations of Chapter 3 for certain seeded confluencies, but failed to accurately describe very low or high seeding densities.

The mitotic fraction of the Markov population model was then derived from a generalised logistic equation. In addition to confluency, the generalised logistic model included ϕ and β parameters that had no defined biological meaning. Assuming a fixed ϕ, it was found that β could be varied to generate curves that corresponded well to the cellular automata simulations that were performed in Chapter 3. An exponential relationship between β and the index of dispersion of cellular automata simulations was discovered and described mathematically. By including this relationship, the generalised logistic equation described the mitotic fraction as a function of confluency and the index of dispersion.

When spatial dispersion was measured, and when the derived β parameter was included, a lower RMSE was achieved for the generalised logistic mitotic fraction when compared to the Verhulst mitotic fraction. It also performed well for very low or high seeding densities. It should be noted that the index of dispersion depends on a certain quadrat size, so the relationship between β and the index of dispersion may be sensitive to different quadrat sizes; however, this is beyond the scope of this study, and could be investigated in future work.

Finally, the Markov population model was adapted to a time-approximation by using the population doubling time equation. The population doubling time equation was adapted to an estimate of *division time*, by only considering the mitotic cells that divide during a sampling interval. This approximation was found to be reasonable for sampling periods that are equal to, or smaller than, the true division time.

Two models for the lag phase were considered: an exponentially decaying function that depends on the number of cells yet to adhere, and a sigmoidal function that describes cells as adhering within a certain period. Both assumptions need to be tested experimentally to determine their validity.

CHAPTER 5 *IN VITRO* MEASUREMENT

5.1 CHAPTER OBJECTIVES

The objective of this chapter is to observe measurable features of ASCs *in vitro*. Instruments and measurement techniques are briefly discussed, and the features that can be derived from measurements are listed. Experimental data of various patients, at various intervals, expanded in various sera, are then presented. The experimental results, and the implications of the results, are briefly discussed at the end of each section.

5.2 INTRODUCTION

Flow cytometry is frequently used to quantitatively measure cell counts, viability, and cell cycle phases. Microscopy, and specifically fluorescence microscopy, is mostly used as a supplemental qualitative measurement [46].

Flow cytometric measurements of ASCs require that cells are dissociated from their adherent state and placed into suspension. This implies that a separate flask needs to be seeded and incubated in parallel for each time point at which flow cytometry will be performed, as seen in Figure 5.1. This means that the same population of cells cannot be observed across multiple time intervals.

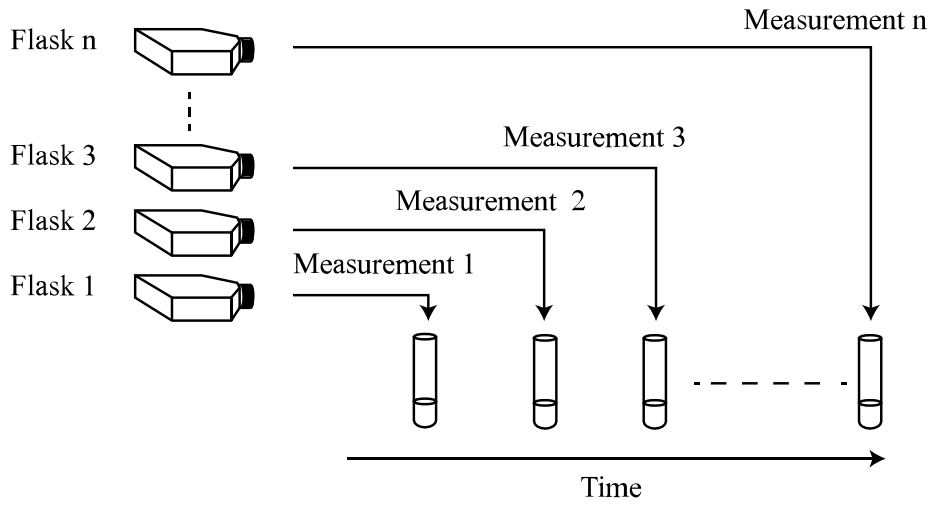

Figure 5.1. The experimental setup that is required when flow cytometry is performed. Each planned measurement requires that a separate flask is expanded in parallel from the start of the experiment. Although only a portion of each flask is measured via flow cytometry, the cells that were not measured remain dissociated. Re-plating dissociated cells are considered a separate passage.

Measurements obtained from unstained phase-contrast imagery do not have this drawback, because microscopy is a non-invasive measurement process. Another advantage is that the spatial positions of individual cells can be measured.

5.3 MEASURABLE FEATURES

5.3.1 Counting

5.3.1.1 Flow cytometric cell counting

A flow cytometer passes cells in suspension through the path of a laser beam, measures the interaction of the laser with the cells, and counts calibrated fluorescent beads to measure the volume of the sample [90]. Intact and viable cells can be counted by using forward and side scatter measurements, after fluorescent staining of the nuclei [91]. This excludes debris and dead cells from measurements.

5.3.1.2 Micrograph cell counting

Adherent ASCs have a characteristic morphology when observed through a phase-contrast microscope, as seen in Figure 5.2.

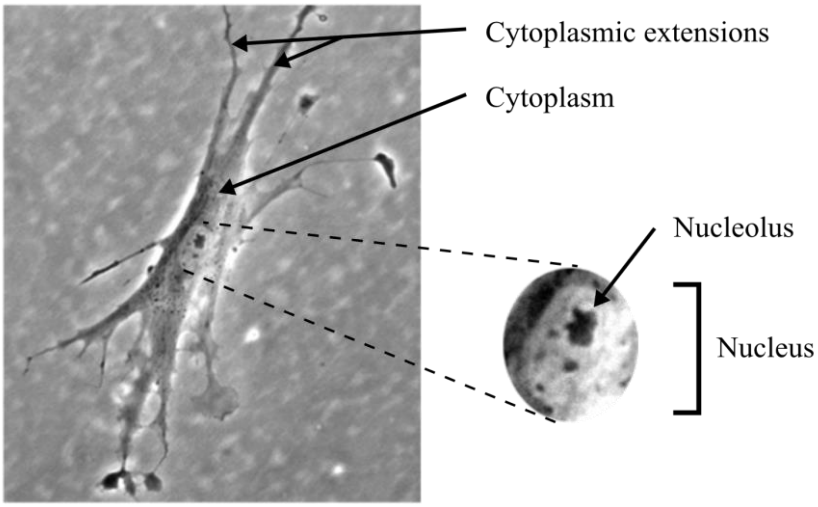

Figure 5.2. The morphology of adherent ASCs when observed using phase-contrast microscopy. The cytoplasm appears darker compared to the background. The nucleus is frequently visible in the form of a lighter-coloured ellipse that contains dark nucleoli.

Microscopy can be performed at magnification levels that capture multiple cells simultaneously on a single image. Such an image is then a sample of the total substrate area of adherent cells. Total population numbers can be estimated by counting a number of samples from the substrate area. A Zeiss Axio Vert.A1 microscope fitted with a Zeiss Axiocam digital camera captures images with a resolution of 1388×1038 pixels, and at 5X magnification each pixel corresponds to 1.075 µm of observed substrate.

The surface area captured by each image at 5X magnification is,

$$A_i = 1.25 \times 10^6 \, \mu m^2.$$

The flask area (A_f) is determined by the manufacturer, for example, in the case of a T25 flask,

$$A_f = 2.5 \times 10^9 \, \mu m^2.$$

If the number of cells in an image (N_i) is counted, then an estimate of the total number of cells in the flask ($\widehat{N}$) is given by

$$\widehat{N} = N_i \left[\frac{A_f}{A_i}\right]. \tag{5.1}$$

5.3.2 Confluency

The decision to passage ASCs is usually based on the percentage confluency [45], which is subjectively estimated by a human observer [92]. However, if each pixel in an image is labelled as either representing a cell or background (which may include the substrate, growth medium, and other non-cellular components), then confluency can be quantified more precisely [92]–[94].

If N_c is the number of pixels that represent cells in an image, and N_b is the number of non-cell (background) pixels in an image, then the percentage confluency of an image (γ_i) is given by

$$\gamma_i = \frac{N_c}{N_c + N_b}. \tag{5.2}$$

5.3.3 Viability

The viability of ASCs can be assessed using flow cytometry, after staining cells with propidium iodide and annexin V. Propidium iodide is a fluorescent dye that cannot cross the membrane of live cells, and annexin V is a cellular protein that binds to the membrane of apoptotic cells. Similar to the counting process described in Section 5.3.1.1, cells are passed through the flow cytometer after staining. The frequency components of the measured fluorescence can then be used to distinguish between live, apoptotic, and necrotic cells [91].

5.3.4 Cell cycle and mitotic fraction

5.3.4.1 Flow cytometric measurement of the cell cycle

The percentage of cells in different phases of the cell cycle can be assessed by measuring the changes in DNA content by 4', 6-diamidino-2-phenylindole (DAPI) staining and flow cytometry [91], [95]. This approach does not distinguish between G0 and G1 phases, and the cell cycle is only measured at a certain instant in time. This means that the cycle measurement is not equivalent to the mitotic fraction. For example, a cell that divided shortly prior to the cell cycle measurement should be considered as part of the mitotic fraction, but both daughter cells would instead be measured as within G0/G1 (i.e. indeterminate).

5.3.4.2 Mitotic fraction estimates from micrographs

The mitotic index is the visible fraction of cells within mitosis (as observed through a microscope), and is a measurement that is used to determine the optimum incubation time in certain protocols [46].

In phase-contrast microscopy, bright contours are often visible around the edges of cells, which is commonly referred to as a halo artefact [93], [96]. Adherent ASCs retract to form a sphere before dividing, which is surrounded by a bright halo when captured on a phase-contrast micrograph. If it can be assumed that a cell that is part of the mitotic fraction is equally likely to divide at any point in time, then the mitotic index could give an indication of the size of the mitotic fraction.

5.3.5 Spatial dispersion

As described in Chapter 3, spatial dispersion is a summary measure of the distribution of cells on the substrate, which indicates whether cells are equally spaced or clustered together in certain areas. In Chapter 3, the index of dispersion was defined in terms of a simulated grid; however, an index of dispersion can also be calculated using micrographs that have been labelled with the coordinates of the centres of cells. An index of less than one indicates more uniformly distributed cells, an index equal to one indicates a Poisson distribution, and an index of greater than one indicates that clusters of cells have been formed.

5.3.6 Adherent cell size

5.3.6.1 Manually labelled phase-contrast micrographs

If cell counts (as described in Section 5.3.1.2), as well as the individual pixels that comprise cells are labelled (as in Section 5.3.2), then the average adherent cell area can be calculated per image. If any cells intersect, then the estimate becomes less accurate, as seen in Figure 5.3.

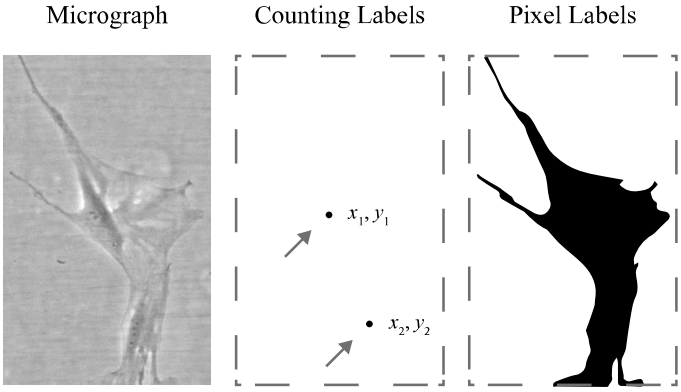

Figure 5.3. An example of the limitations of cell area estimation using labelled pixels. If cells intersect, then the average area in pixels becomes less accurate owing to cell area overlap.

5.3.6.2 Fluorescent micrographs

Nuclei can be stained with DAPI, and cytoplasm with a carboxyfluorescein succinimidyl ester (CSFE) [97]. Fluorescent micrographs of the same area can then be captured through different filters, and automated processing of the cells can measure the surface area occupied by each adherent cell in each image [97]. Fluorescent staining simplifies the task of labelling the pixels in a micrograph; however, dyes have varying levels of toxicity [98], which precludes the use of dyes in a clinical setting.

5.4 EXPERIMENTAL MEASUREMENTS

The following experiments were performed by Dessels [91], [97] to compare the expansion of ASCs in human alternatives (such as pHPL) to those expanded in FBS. The study, and the sharing of data, was approved by the University of Pretoria Faculty of Health Sciences

Ethics Committee (number 421/2013). Platelet concentrates were obtained from the South African National Blood Service (SANBS) under approval number 2013/17. A summary of the experimental data is shown in Table 5.1.

The experimental data has been grouped into fundamental (Section 5.4.1) and intra-passage (Section 5.4.2) characteristics. Fundamental characteristics guide the applicability of models and can be used as prior knowledge, while intra-passage measurements can be used to train and validate proliferation models. Inter-passage characteristics were considered beyond the scope of this study, but are described in Addendum B.

Cells from the same three patients were used in Sections 5.4.1.2 and 5.4.2.2. Different patients were used in each of the other experiments.

Table 5.1 A summary of the experimental data that was provided to this study.

Fundamental characteristics		
Section	**Experiment**	**Measurements**
5.4.1.1	Multi-patient population limit and cell death expanded in both FBS and pHPL	• Flow cytometric cell counts • Flow cytometric viability
5.4.1.2	Cell size assay	• Cell sizes determined by stained fluorescent micrographs
Intra-passage characteristics		
Section	**Experiment**	**Measurements**
5.4.2.1	Single-patient proliferation assay expanded in FBS	• Flow cytometric cell counts • Flow cytometric viability • Phase-contrast micrographs
5.4.2.2	Multi-patient proliferation assay expanded in both FBS and pHPL	• Flow cytometric cell counts • Flow cytometric viability • Flow cytometric cell cycle analysis • Phase-contrast micrographs
5.4.2.3	Non-destructive single-patient proliferation assay expanded in FBS	• Phase-contrast micrographs

5.4.1 Fundamental characteristics

5.4.1.1 Population limit and cell death

ASCs isolated from the abdominal and gluteal fat of two patients, and the gluteal fat of a third patient, were expanded in a set of 5 flasks with FBS, and a set of 5 flasks with pHPL, until visually confluent. The various patients and sera required different times to reach confluency, and the subsequent measurements did not occur simultaneously. One flask of each set was measured at confluency, while the other four flasks remained incubated and supplemented with fresh medium for 1, 7, 14, and 21 days after confluency, and were then measured. Cell counts and viability percentages were determined via flow cytometry, and are shown in Figures 5.4 and 5.5 respectively. The adipose extraction site is abbreviated as A (abdominal) and G (gluteal) next to each patient identifier.

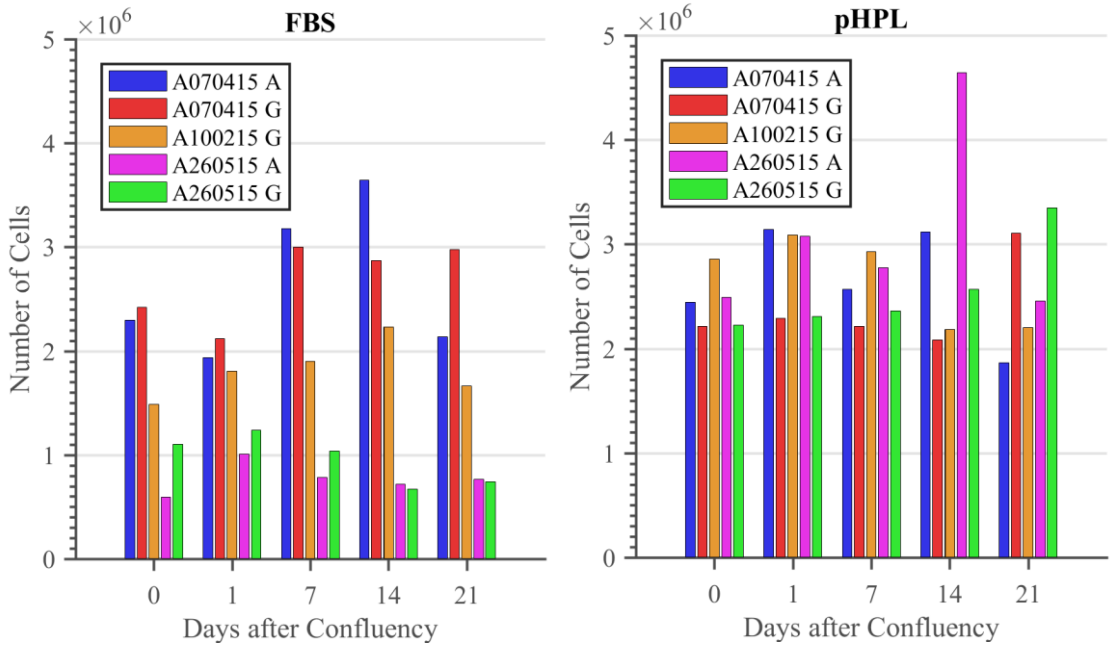

Figure 5.4. The number of cells at confluency, and 1, 7, 14 and 21 days post-confluency, of (a) cells expanded in FBS, and (b) cells expanded in pHPL.

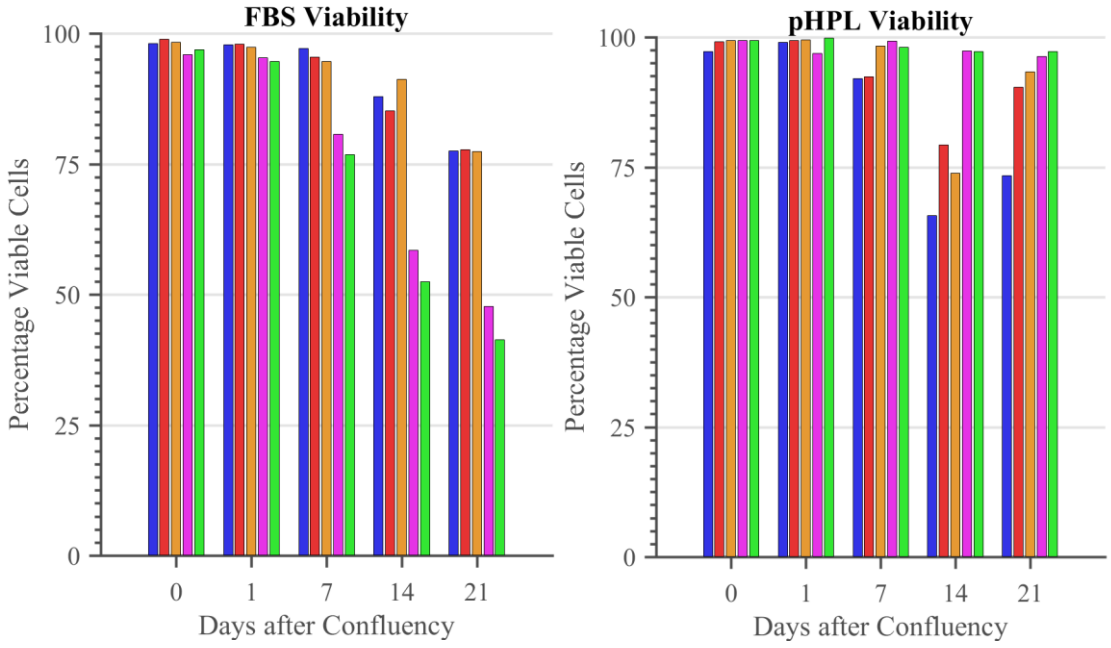

Figure 5.5. The viability percentages at confluency, and 1, 7, 14 and 21 days post-confluency, of (a) cells expanded in FBS, and (b) cells expanded in pHPL.

5.4.1.2 Adherent cell size

Cells from three patients were expanded for 7 days in either FBS or pHPL, and five micrographs were captured for each patient and each serum. Cells were stained with DAPI and CSFE, and fluorescent micrographs were captured at different wavelengths [97], as seen in Figure 5.6.

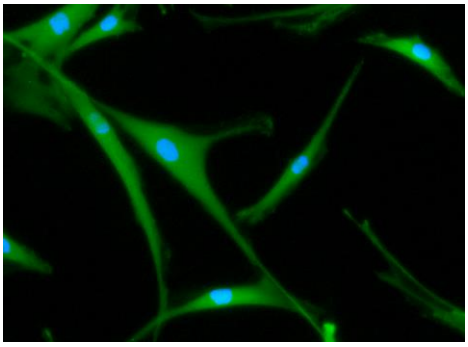

Figure 5.6. An example of fluorescent staining of cytoplasma using CSFE (green), and nuclei using DAPI (blue).

Automated processing of the micrographs, using ImageJ [99] provided the number of pixels occupied by each cell. Probability density estimates of the measured cell areas, using a normal kernel function, is shown in Figure 5.7.

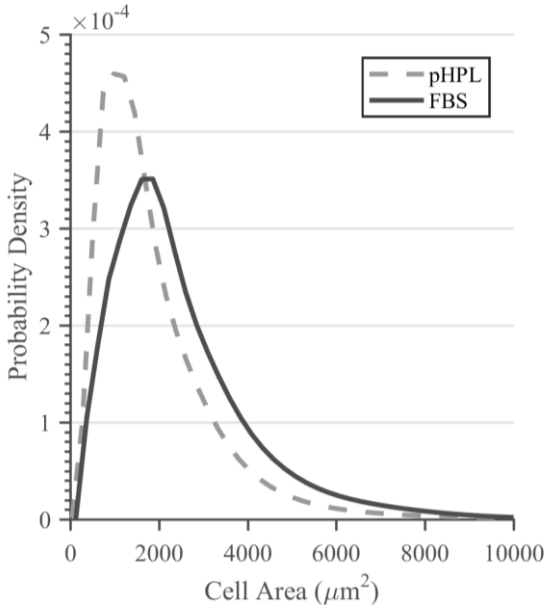

Figure 5.7. Probability density estimates of the areas occupied by adherent ASCs expanded in FBS and pHPL at day 7. The data represents 414 FBS and 359 pHPL cell sizes, measured from three patients and five images per patient for each serum [97].

5.4.1.3 Discussion

ASCs appear to have a population limit, but the limit seems to vary between patients and sera. The inter-patient variability of the population limit was greater when expanded in FBS, and cells from certain patients reached consistently higher numbers than other patients. Cells expanded in pHPL resulted in lower inter-patient variability, and reached higher population limits compared to FBS. When expanded in FBS, cells decreased in viability after 7 days at confluence. The viability of pHPL-expanded cells also decreased when cultured at confluence, but remained more viable compared to FBS.

If two flasks both contain a confluent monolayer of cells, but the absolute cell count in each flask is different, then the larger population would occupy less area on the substrate per cell. Cell sizes of both FBS- and pHPL-expanded cells were measured, and resulted in positive skewed distributions, where smaller cells appear more commonplace. Cells expanded in

pHPL occupied a smaller median area per cell, and exhibited less variation in size. This suggests that ASCs remain in a monolayer, and that variation in cell sizes affect the population limit.

5.4.2 Intra-passage characteristics

5.4.2.1 Single-patient proliferation assay expanded in FBS

ASCs isolated from a patient at passage 10 were seeded into 10 flasks at 1000 cells/cm^2 and 10 flasks at 5000 cells/cm^2. Flow cytometric counts and viability were measured daily for 10 days, as seen in Figure 5.8.

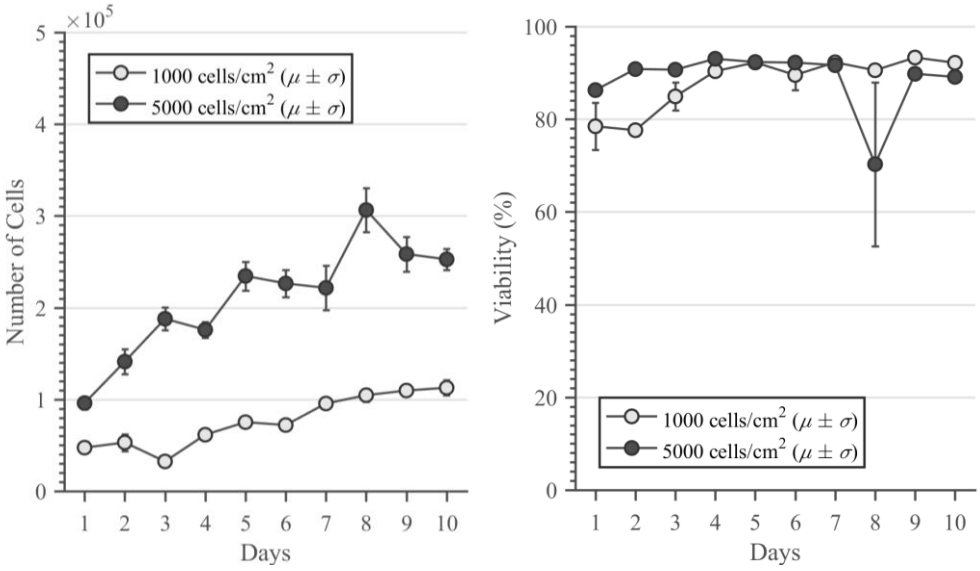

(a) (b)

Figure 5.8. The mean and standard deviation of (a) cell counts, and (b) viability of cells seeded at 1000 and 5000 cells per cm^2. Error bars are present but not necessarily visible on all curves. The large variability of viability at day 8, for cells seeded at 5000 cells/cm^2, is likely due to technical error.

In addition to the flow cytometric measurements, daily micrographs were captured. The coordinates of cells were labelled on the micrographs. The counts derived from the micrographs, compared to counts obtained via flow cytometry, are shown in Figure 5.9. Images were then divided into 4 x 6 quadrats, and the labelled cell coordinates were used to calculate the index of dispersion per image, and per day, as seen in Figure 5.10.

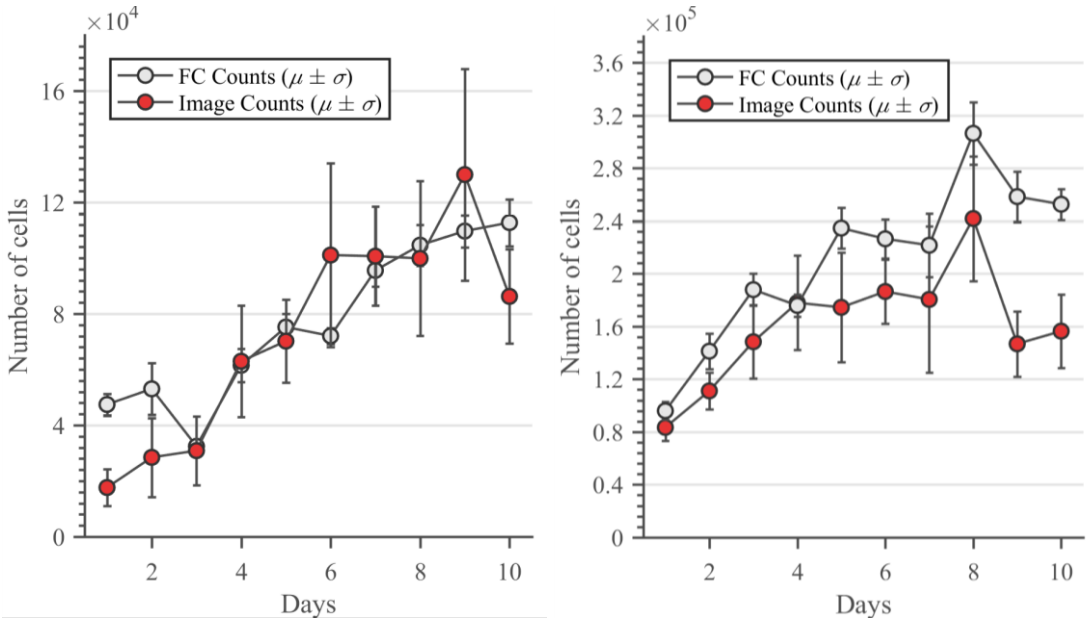

(a) (b)

Figure 5.9. The mean and standard deviation of cell counts measured using a flow cytometer (grey) compared to cell counts derived from images (red) for (a) 1000 cells/cm^2, and (b) 5000 cells/cm^2. T25 flasks were used, and $A_f/A_i = 2500$.

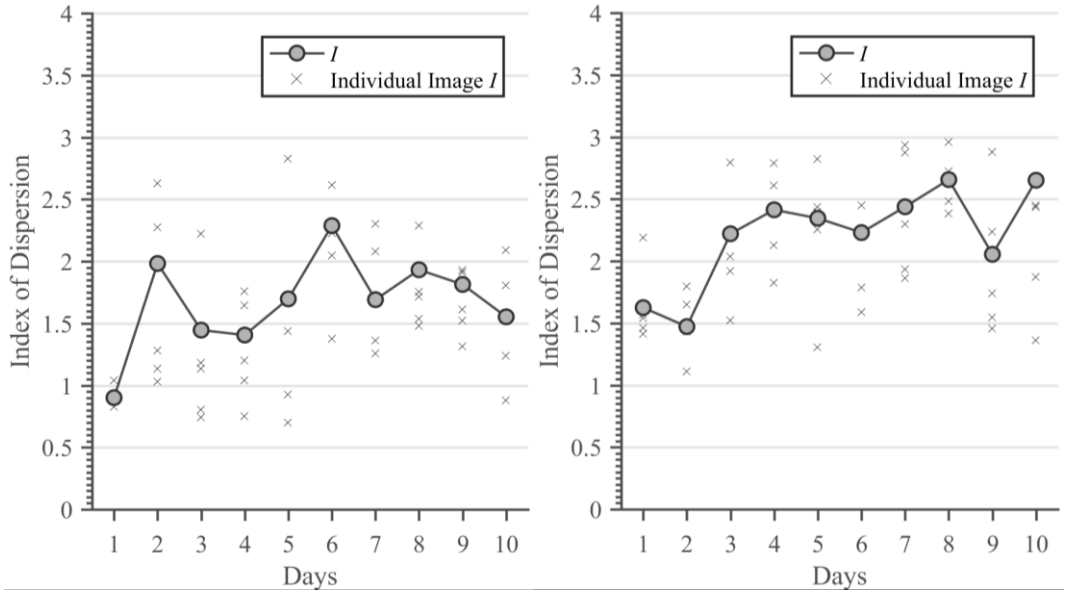

(a) (b)

Figure 5.10. The index of dispersion (I) per day, derived from images that were divided into 4 x 6 quadrats for (a) 1000 cells/cm^2, and (b) 5000 cells/cm^2. Crosses indicate the indices of dispersion of individual images.

In addition to the coordinate labels, the pixels that comprise cells were labelled for the flask seeded at 1000 cells/cm^2, as shown in Figure 5.11. The quantified percentage confluency was calculated using (5.2) and is shown in Figure 5.12.

The number of cell-pixels per image were divided by the number of cells counted per image, to derive the average adherent cell area, as shown in Figure 5.13 (a). The relationship between the number of cells per image and the confluency of the image, and a least-squares linear fit of this relationship, is shown in Figure 5.13 (b). The linear fit in Figure 5.13 (b) means that if more cells are captured in an image, then the confluency of that image will increase proportionally by

$$\gamma_i = 0.7\, N_i - 2.5, \tag{5.3}$$

where γ_i represents the confluency of the image, and N_i is the number of cells in the image.

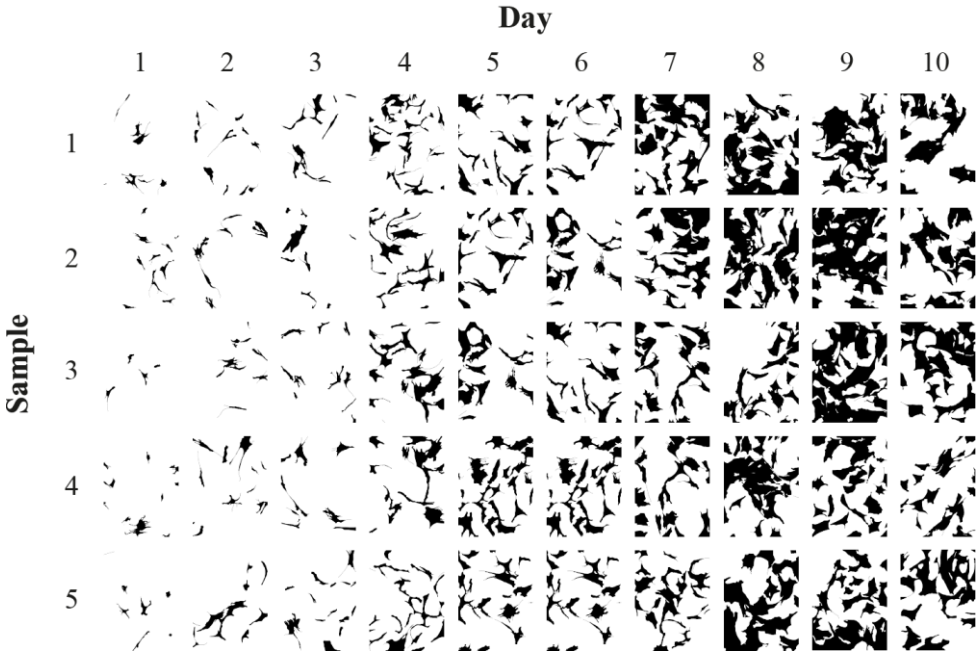

Figure 5.11. Manually labelled cell-pixels (black) and background pixels (white) per day of cells seeded at 1000 cells/cm^2. Rows in each column represent randomly selected areas in the same flask. Each column represents a different flask that was cultured for a day longer than the previous column.

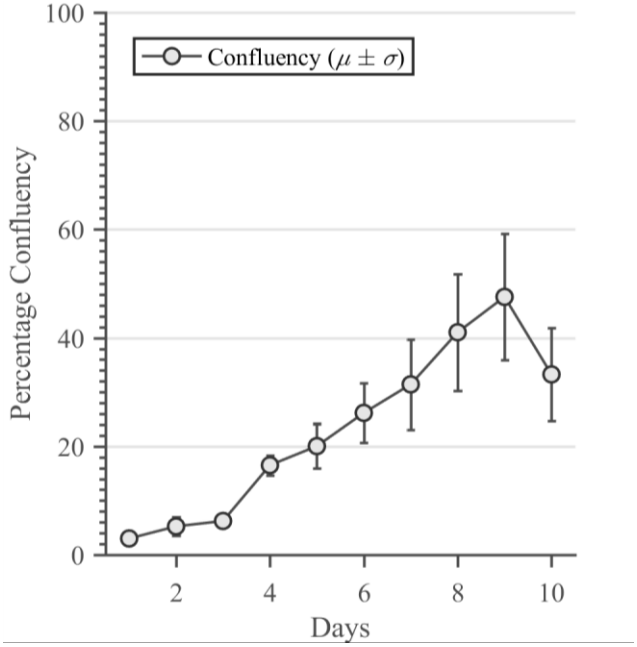

Figure 5.12. Confluency per day of cells seeded at 1000 cells/cm^2, calculated using (5.2) after manual pixel labelling.

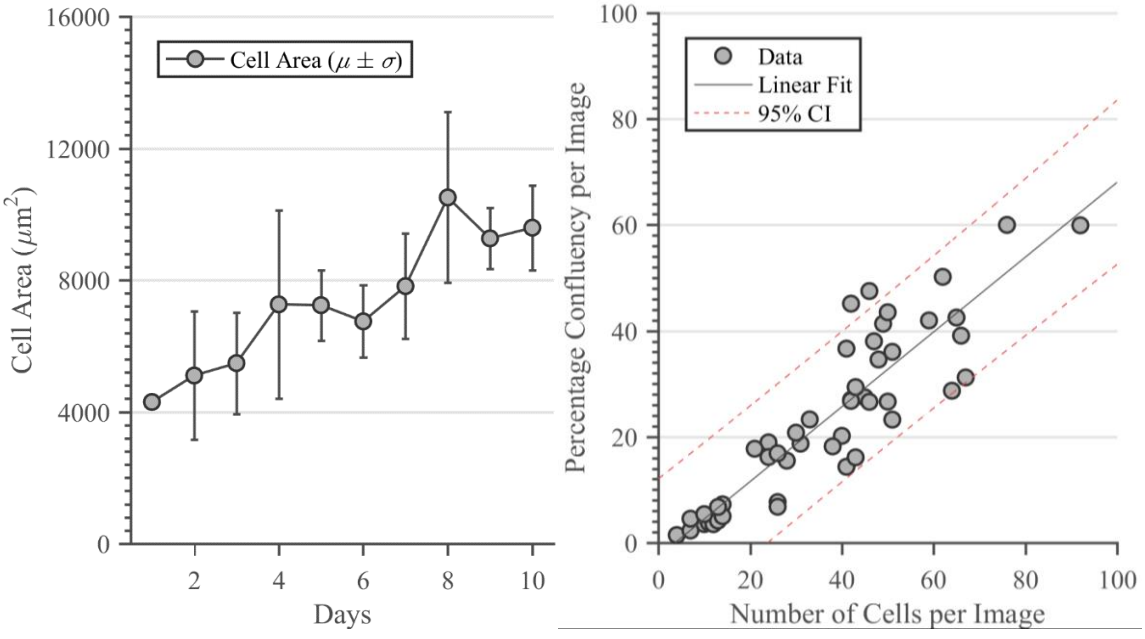

(a) (b)

Figure 5.13. (a) The average cell area per day. (b) A linear least-squares approximation of the relationship between the percentage confluency (γ_i) and the number of cells per image (N_i). The linear model represents $\gamma_i = 0.7\ N_i - 2.5$. The dashed red lines represent the 95% confidence interval of the model.

5.4.2.2 Multi-patient proliferation assay expanded in both FBS and pHPL

ASCs at passage 5, isolated from the same patient and extraction sites as Section 5.4.1.2, were plated into 14 flasks supplemented with FBS and 14 flasks supplemented with pHPL. Flow cytometric counts and viability were measured daily, as shown in Figures 5.14, 5.15 and 5.16. It is important to note that the vertical axis of Figure 5.14 (b) is an order of magnitude greater than Figure 5.14 (a); therefore, after approximately 4 days, ASCs expanded in pHPL exceeded the number of ASCs yielded after 14 days in FBS. The error bars in Figure 5.14 (a) and (b) represent technical replicates. The variability of cell counts between days in Figure 5.14 (b) is likely due to differences in viability, as can be seen in Figures 5.15 and 5.16.

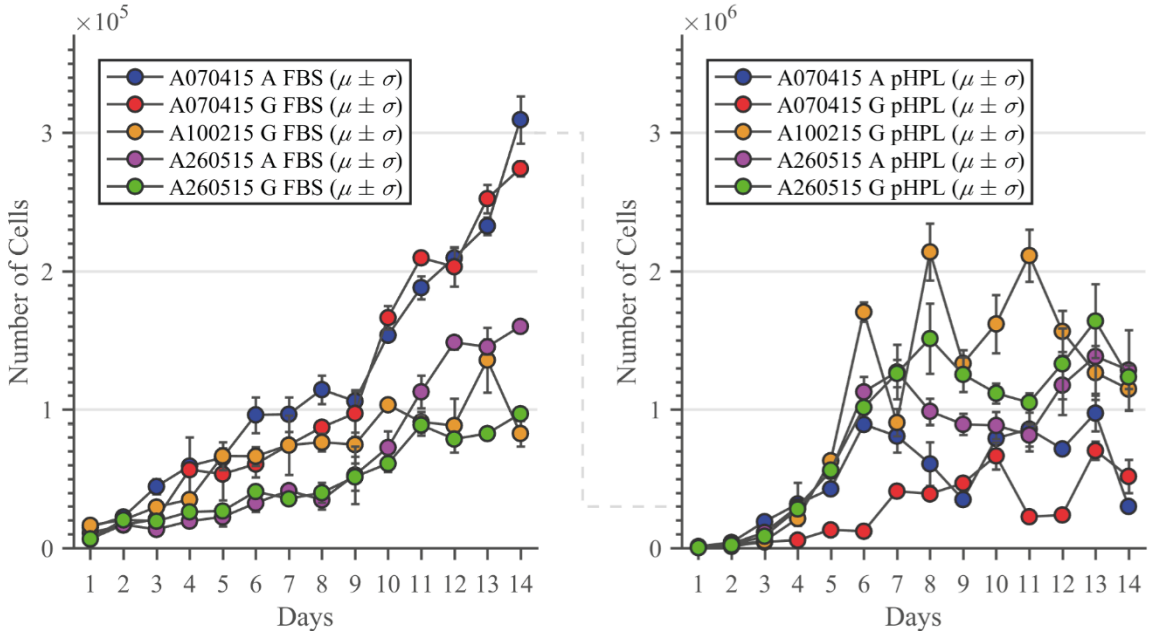

Figure 5.14. (a) The number of FBS-expanded ASCs per day. (b) The number of pHPL-expanded ASCs per day. The vertical axis of (b) is an order of magnitude greater than (a), and the dashed line indicates the position of 3×10^5.

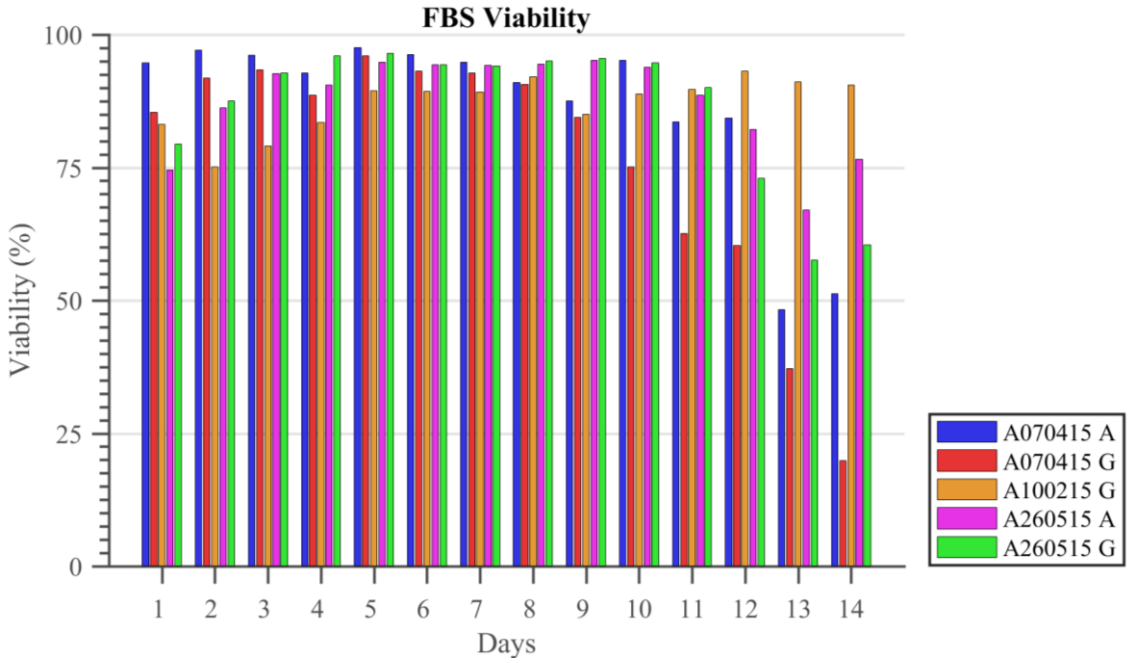

Figure 5.15. Daily viability percentages of FBS-expanded ASCs measured using flow cytometry.

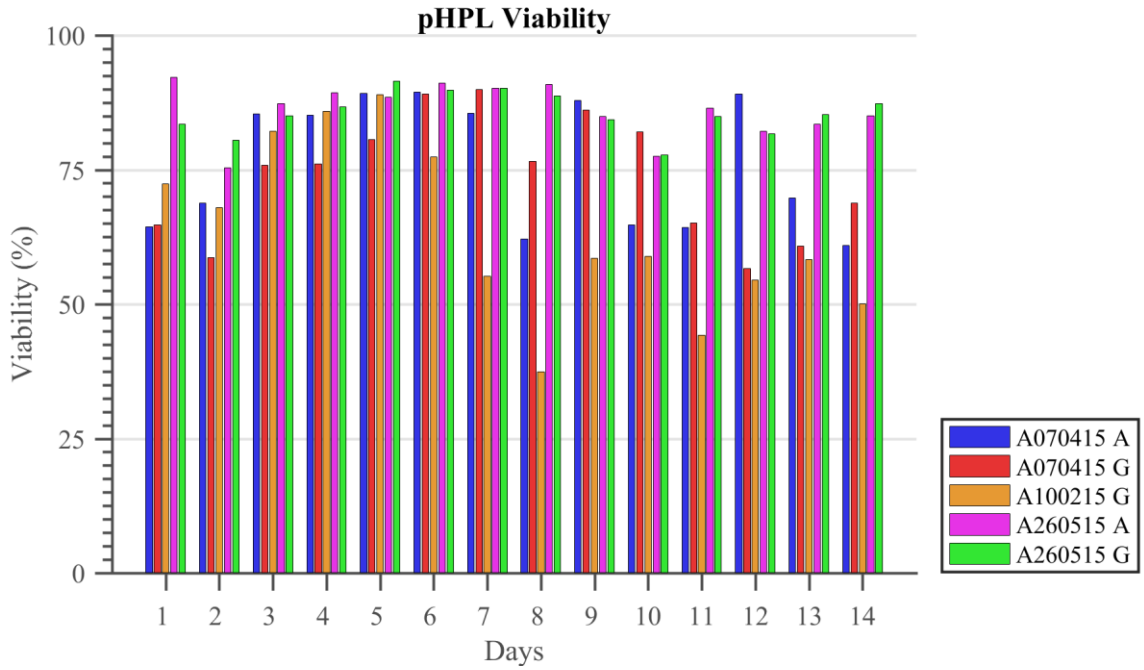

Figure 5.16. Daily viability percentages of pHPL-expanded ASCs measured using flow cytometry.

Cell cycle analysis was performed (as described in Section 5.3.4.1), and the percentage of cells in phases G0/G1, S, and G2/M is shown in Figure 5.17.

The index of dispersion for 4 x 6 quadrats was calculated using manually labelled cell coordinates on phase-contrast micrographs. Micrographs from pHPL patients were confluent from 7 days onwards, and the positions of cells could not be reliably marked. In these cases no index of dispersion could be calculated. The daily indices of dispersion are shown in Figures 5.18 and 5.19.

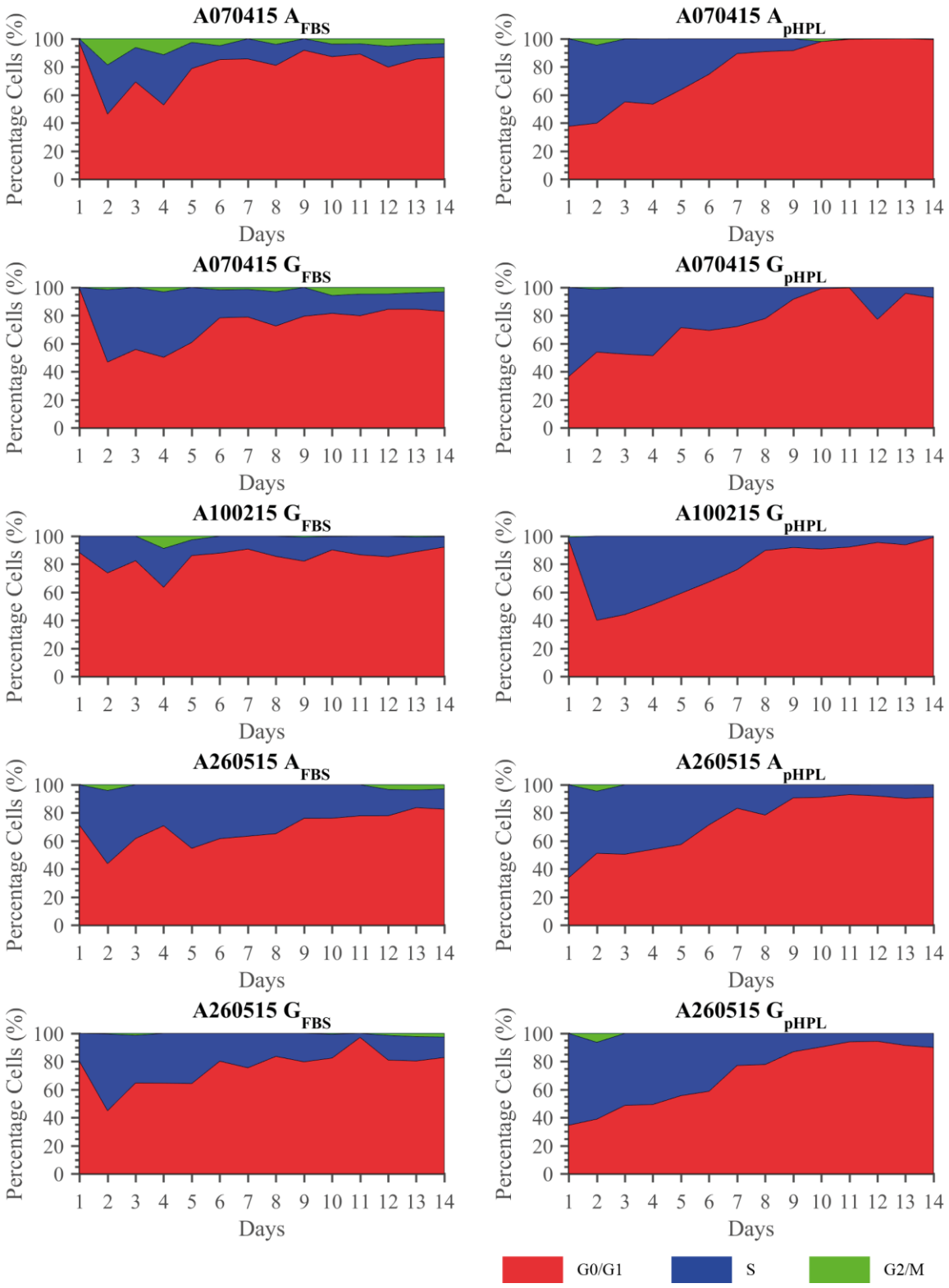

Figure 5.17. Cell cycle percentages measured using flow cytometry, of cells expanded in FBS (left) and pHPL (right).

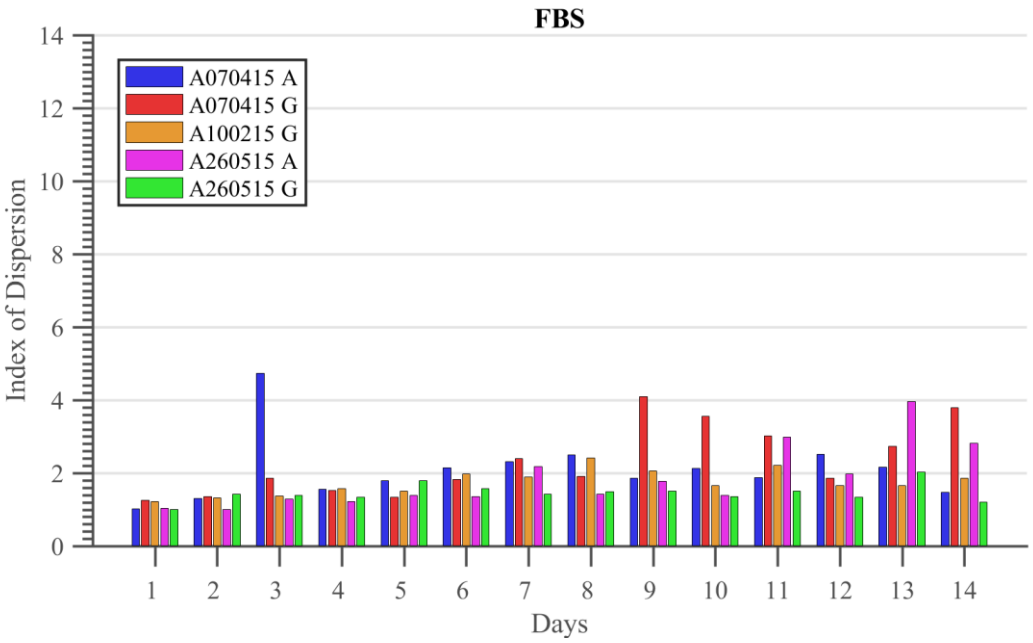

Figure 5.18. Daily indices of dispersion of cells expanded in FBS. Indices were calculated using images that were divided into 4 x 6 quadrats.

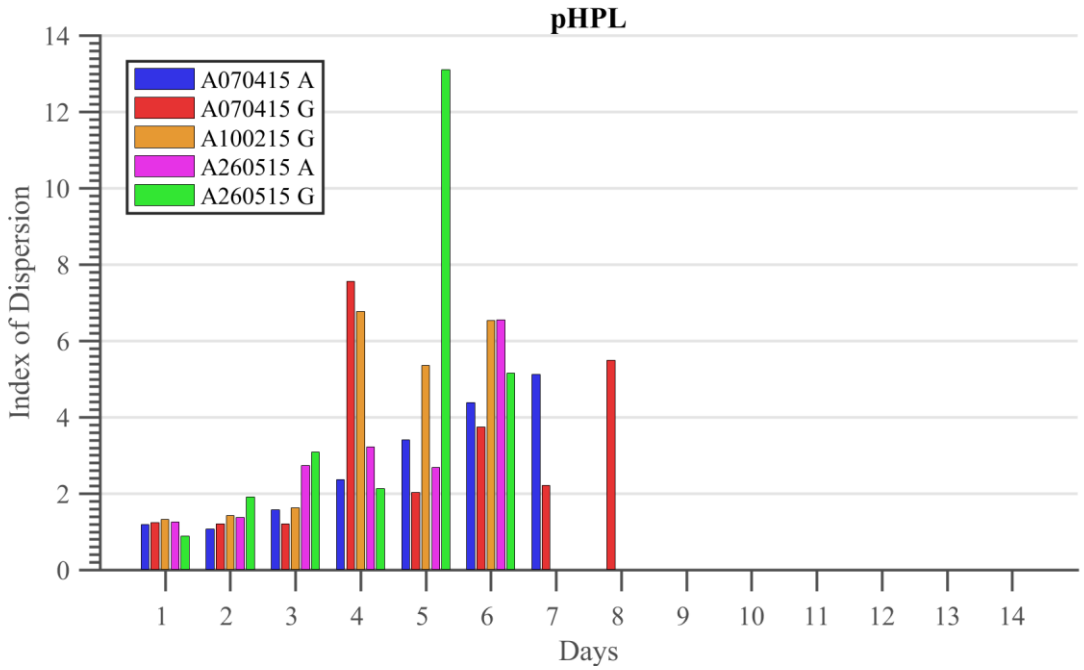

Figure 5.19. Daily indices of dispersion of cells expanded in pHPL. Owing to over-confluency from day 7 onwards, cells could no longer be labelled reliably. Indices were calculated using images that were divided into 4 x 6 quadrats.

5.4.2.3 Non-destructive proliferation assay expanded in FBS

ASCs at passage 10 were seeded into 3 wells at 2500 cells/cm^2. Images of the same wells were captured daily for 7 days, i.e. no destructive measurements were taken. The number of cells is shown in Figure 5.20 (a), and the indices of dispersion are shown in Figure 5.20 (b).

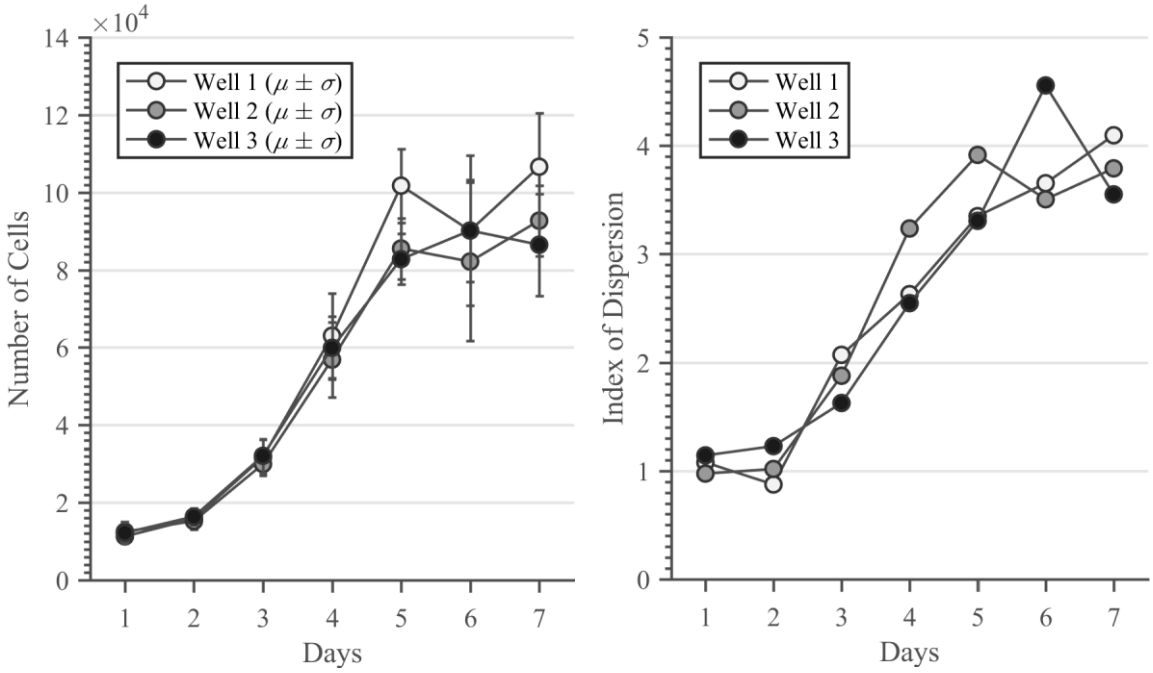

Figure 5.20. (a) The number of FBS-expanded ASCs per day derived from image counts, with $A_f/A_i = 305$. (b) Daily indices of dispersion of cells expanded in FBS using images that were divided into 4 x 6 quadrats.

5.4.2.4 Discussion

The intra-passage characteristics of ASCs were investigated in this section, and experimental data of three proliferation assays are presented. The first proliferation assay only considered a single patient and FBS supplementation, but varied the seeding density. The growth kinetics and population limit of this patient were strongly affected by seeding density. When seeded at a lower density, cells seemed to reach a lower plateau, even though only a comparatively low confluency of 50 to 60 percent was reached. A lower seeding density resulted in lower viability for the first three days in culture, but then reached approximately

equivalent viability in subsequent days. This indicates that cell death was not the primary reason for the lower population limit.

Cell counts that were estimated using phase-contrast micrographs corresponded well to counts obtained using flow cytometry, although measurements from images resulted in greater variance. In addition to the labelled counts, the pixels of each micrograph were labelled, and confluency was quantified as the ratio of cell pixels to total pixels per image. It was found that confluency could be approximated well by cell counts, if the population limit is known. This means that in certain cases the labour-intensive process of individual pixel labelling can be omitted. However, the decision to passage is usually based on a subjective estimate of confluency, and a more quantitative approach could be valuable in clinical applications. Automated image-processing approaches could potentially be employed to classify pixels for this purpose.

Cell area was estimated using the number of cell pixels and the number of cells counted per image. The average cell size did not correspond well to the FBS-expanded cell sizes that were measured using fluorescent dyes in Section 5.4.1.3. This can be attributed to the cells not being individually labelled, and that only the average number of pixels per cell was calculated. Since a positive-skewed distribution of cell sizes was observed, it could be expected that the mean cell size is higher than the median. Though biased, the average cell size increased over time, which could indicate that cells spread when they remain in culture for protracted periods and cease to proliferate. This could be important to account for when cell counts are used to estimate confluency, or when population limits are estimated using cell sizes.

The index of dispersion was calculated using labelled cell coordinates on micrographs. Cell positions were initially approximately Poisson distributed when seeded, but cells became more clustered in subsequent days. A difference in spatial dispersion was observed between images on the same day, where cells in certain images remained Poisson distributed and in certain cases became more uniformly distributed.

The second proliferation assay consisted of a large multi-patient comparison between FBS and pHPL. A large amount of inter-patient variability in growth kinetics was observed in both FBS- and pHPL-expanded cells. Intra-patient differences on consecutive days were also observed, which are likely to be a side-effect of observing parallel-plated cells instead of the same population of cells. It is possible that small differences in initial conditions, such as in seeding density, have a large resulting effect over time. Equally important are the intrinsic differences in cells isolated from different donors, whose age and medical history were not taken into consideration.

The number of cells obtained using pHPL was nearly an order of magnitude greater than cells expanded in FBS. Viability differed between patients and between sera; pHPL viability markedly decreased after confluency (at approximately day 7), while FBS decreased steadily from day 9 onwards, even when confluency had not been reached.

The percentage of cells in each cell cycle phase was measured. A lag period of 1 day was observed for FBS, which was characterised by a lower number of cells in the S phase. In contrast, the majority of cells expanded in pHPL were in the S phase on day 1, with the exception of one patient. The S phase of cells expanded in pHPL remained larger compared to FBS for the first seven days, after which confluency was reached in pHPL, and the S phase percentage decreased. A percentage of cells expanded in FBS remained in the S phase at the end of the 14 day period, which could indicate that a plateau had not yet been reached.

The index of dispersion of FBS mirrored earlier results, where cell positions were initially approximately Poisson-distributed, then steadily became more clustered. Inter-patient variability was also observed here, but in contrast to what was predicted by cellular automata simulations in Chapter 3, patients with lower indices of dispersion divided more slowly. This could indicate that the index of dispersion is a side-effect of varying proliferation rates, and not a causal predictor of proliferation rates. This was also observed in pHPL, where higher indices of dispersion resulted in faster proliferation compared to FBS.

In the first two proliferation assays each daily measurement required a separate flask, as described in Figure 5.1. A third proliferation assay utilised non-destructive phase-contrast

micrograph measurements, which were captured daily in three wells. Measurements in different wells did not display the expected intra-patient variability. This could be a consequence of the well substrate area that is smaller than that of the flasks used in prior proliferation assays.

5.5 CHAPTER SUMMARY

This chapter presents results of *in vitro* experiments. First, fundamental characteristics were investigated. Confluent ASCs were cultured for up to 21 days post-confluency, and a population limit appeared to have been reached. However, the limit differed between patients and the different sera. Cells from certain patients reached consistently higher numbers than other patients when expanded in FBS, while all patients reached higher population limits in pHPL. Cell sizes were measured, and a positive skewed distribution was observed where smaller cells appear more commonplace. ASCs expanded in pHPL were smaller than those expanded in FBS, which could indicate that cell size plays a role in determining the population limit. Alternatively, cells that proliferate slowly tend to spread more.

Next, intra passage characteristics were investigated through three proliferation assays, and substantial variability between patients, sera and seeding densities was observed. ASCs expanded at low seeding densities in FBS seemed to reach an intra-patient population limit, even though low (60%) confluency was observed. This could indicate that space constraints are not the only limiting factor when expanding ASCs, and that cell-to-cell interactions could be an important factor.

A multi-patient proliferation assay that compared FBS and pHPL was performed, and cell counts and viability differed substantially between patients. Considerable differences in cell counts of subsequent days, within the same patient, were also observed: cell counts nearly halved in one day, then more than doubled in the following day. This is likely a result of variability introduced by the experimenter for example at the time of seeding, and is reflective of the parallel expansion in separate flasks that are dissociated prior to daily flow cytometer measurements.

The number of cells obtained using pHPL was approximately an order of magnitude greater than cells expanded in FBS. In contrast to what was predicted by the cellular automata simulations in Chapter 3, patients with lower indices of dispersion divided more slowly. In addition, the faster-dividing pHPL-supplemented cells resulted in high indices of dispersion. Instead of a causal predictor of proliferation rates, this may indicate a reverse-causality between proliferation rates and the index of dispersion.

CHAPTER 6 RESULTS AND DISCUSSION

6.1 CHAPTER OBJECTIVES

The objective of this chapter is to evaluate the population models described in Chapter 4 based on their descriptive and predictive capacity of the measured data described in Chapter 5. Descriptive capacity refers to how well each model describes the data given a complete set of observations, while predictive capacity evaluates the model predictions of future observations, when only partial observations are supplied. Over-fitting is a risk whenever optimisation is performed; therefore, simpler models are preferred for generalisation to different patients.

6.2 INTRODUCTION

The intra-passage measurements that were described in Section 5.4.2.1 were used for both descriptive and predictive validation, and are numbered in Table 6.1. Additionally, each experiment was stratified into one of four experimental groups.

The cell cycle measurements in Section 5.4.2.2 do not distinguish between G0 (non-mitotic fraction) and G1 (part of mitotic fraction) phases; therefore, they were not included in validation of the mitotic fraction, and validation was limited to cell counts. The RMSE of cell counts was used as a measure of accuracy, i.e. the error function.

Table 6.1 The experiment numbers and groups used in this chapter.

Experimental group	Experiment number	Seeding density	Substrate area (cm^2)	Serum supplement	Relevant section
1	1	1000	25	FBS	5.4.2.1
	2	5000	25	FBS	5.4.2.1
2	3	1000	25	FBS	5.4.2.2
	4	1000	25	FBS	5.4.2.2
	5	1000	25	FBS	5.4.2.2
	6	1000	25	FBS	5.4.2.2
	7	1000	25	FBS	5.4.2.2
3	8	1000	25	pHPL	5.4.2.2
	9	1000	25	pHPL	5.4.2.2
	10	1000	25	pHPL	5.4.2.2
	11	1000	25	pHPL	5.4.2.2
	12	1000	25	pHPL	5.4.2.2
4	13	2500	3.8	FBS	5.4.2.3
	14	2500	3.8	FBS	5.4.2.3
	15	2500	3.8	FBS	5.4.2.3

6.3 DESCRIPTIVE MODELLING

6.3.1 Assumptions

It is assumed that cells were seeded at a known density on a known substrate area, allowing N_0 to be calculated. It was also assumed that a set of cell counts and spatial dispersion measurements for h days were known for each experiment, i.e. $\{N_1, N_2, \dots, N_h\}$ and $\{I_1, I_2, \dots, I_h\}$.

Apoptosis was not included in the models; therefore, if $N_1 < N_0$, then N_0 was set equal to N_1. Certain spatial dispersion measurements of the cells expanded in pHPL of experimental group 3 could not be taken after a certain number of days. In these cases, the last known spatial dispersion measurement was used for the remaining days. This assumption could significantly affect the results if the index of dispersion changes in following days. Specifically, as confluency is approached, the index of dispersion becomes the degenerate case of $I = 0$. It is expected that the assumption of a constant non-zero index of dispersion would have a detrimental effect on the accuracy of models.

When the population limit was not optimised, it was assumed as

$$K = \max(\{N_1, N_2, \dots, N_h\}). \tag{6.1}$$

6.3.2 Optimisation strategy and model description

In Chapter 4, when the population model was compared to the cellular automata data it was convenient to quantify errors in terms of confluency. However, if the population limit is not known, as is the case with experimental data, confluency cannot reliably be determined from cell counts. Instead, errors were quantified in terms of the RMSE of cell counts.

The optimised variables and abbreviations for each model are shown in Table 6.2. In the case of VH-1 and GL-1, K was not optimised but assumed as (6.1). VH-3 and GL-3 were optimised for an exponential lag parameter, and VH-4 and GL-4 for sigmoidal lag, as discussed in Section 4.6

Table 6.2 The optimised variables and abbreviations of the models considered for optimisation.

Mitotic fraction model	Model abbreviation	Optimised variables
Verhulst	VH-1	DT
Verhulst	VH-2	DT and K
Verhulst	VH-3	DT, K, and τ_{lag}
Verhulst	VH-4	DT, K, ξ, and $t_{1/2}$
Generalised logistic	GL-1	DT
Generalised logistic	GL-2	DT and K
Generalised logistic	GL-3	DT, K, and τ_{lag}
Generalised logistic	GL-4	DT, K, ξ, and $t_{1/2}$

6.3.3 Error surfaces

Certain sets of parameters could yield similar outputs. For example, a lower mitotic fraction could result in similar cell counts for a longer division time.

Complete enumeration of the optimisation space was performed for VH-2 and GL-2 to examine if multiple equivalent solutions existed. For each K and DT the RMSE was calculated, and the error contours of representative examples are shown for experimental

groups 1 and 2 in Figure 6.1, and experimental groups 3 and 4 in Figure 6.2. Blue contours indicate a smaller RMSE. An error contour with a single global minimum indicates the presence of a single solution. A single minimum is preferable, since additional measurements are not needed to distinguish between solutions.

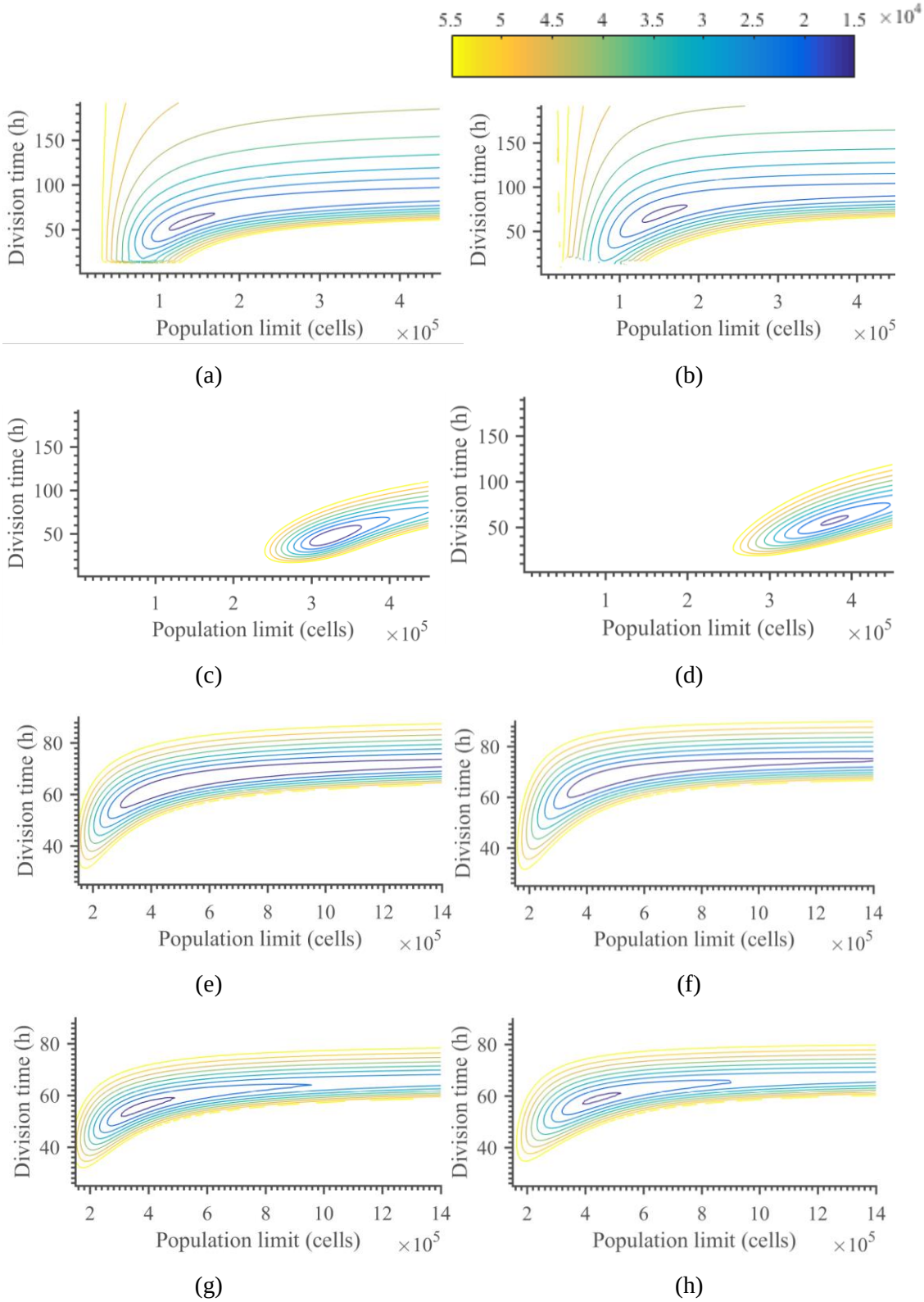

Figure 6.1. The error surface contours for VH-2 (left) and GL-2 (right) mitotic fractions for (a) – (b) experiment 1, (c) – (d) experiment 2, (e) – (f) experiment 3, (g) – (h) experiment 4.

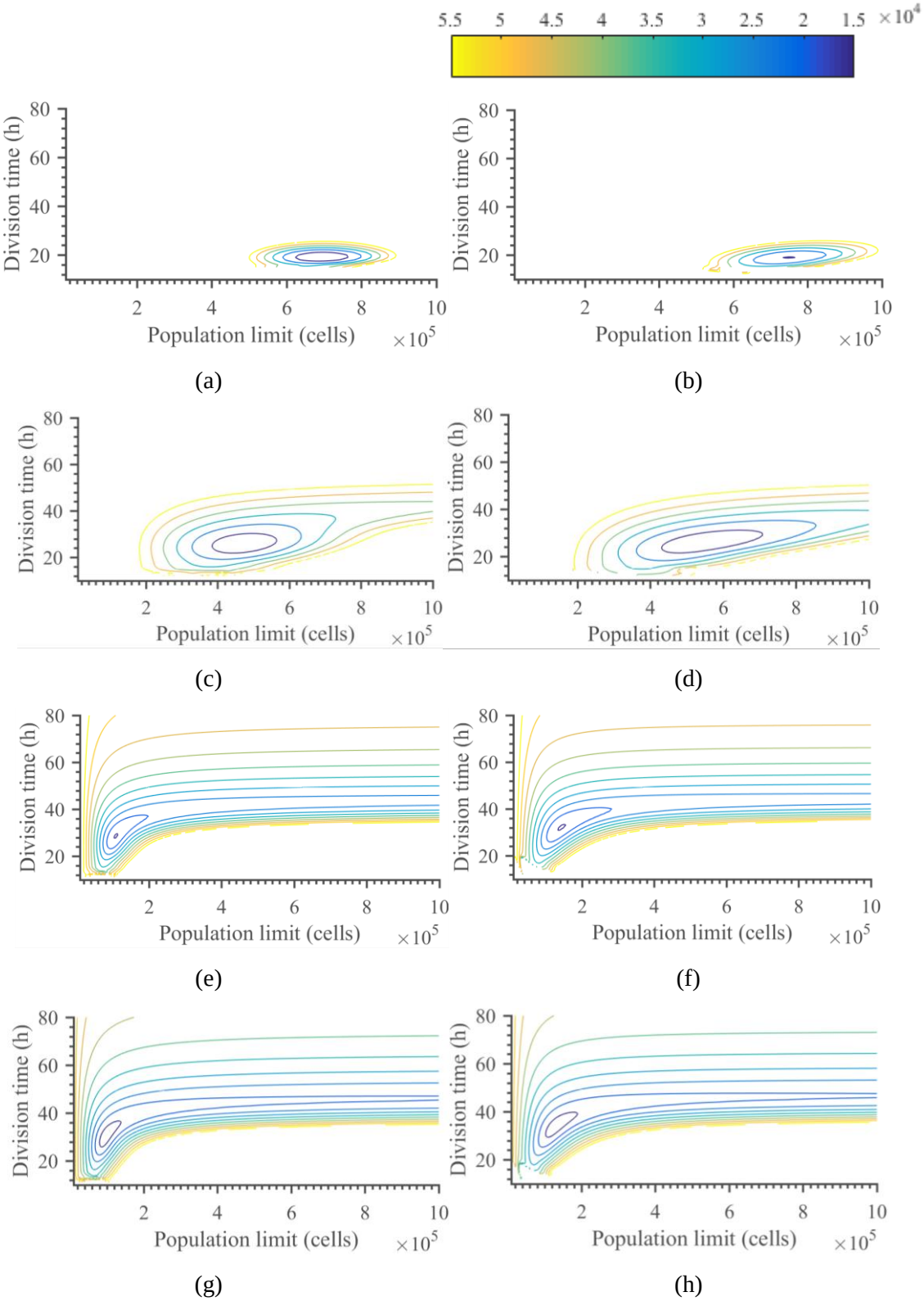

Figure 6.2. The error surfaces for VH-2 (left) and GL-2 (right) mitotic fractions for (a) – (b) experiment 8, (c) – (d) experiment 9, (e) – (f) experiment 14, (g) – (h) experiment 15.

6.3.4 Results

The optimisation results for all experiments are listed in Table C.1 in Addendum C. An example of the optimised models for experiment 13 is shown in Figure 6.3.

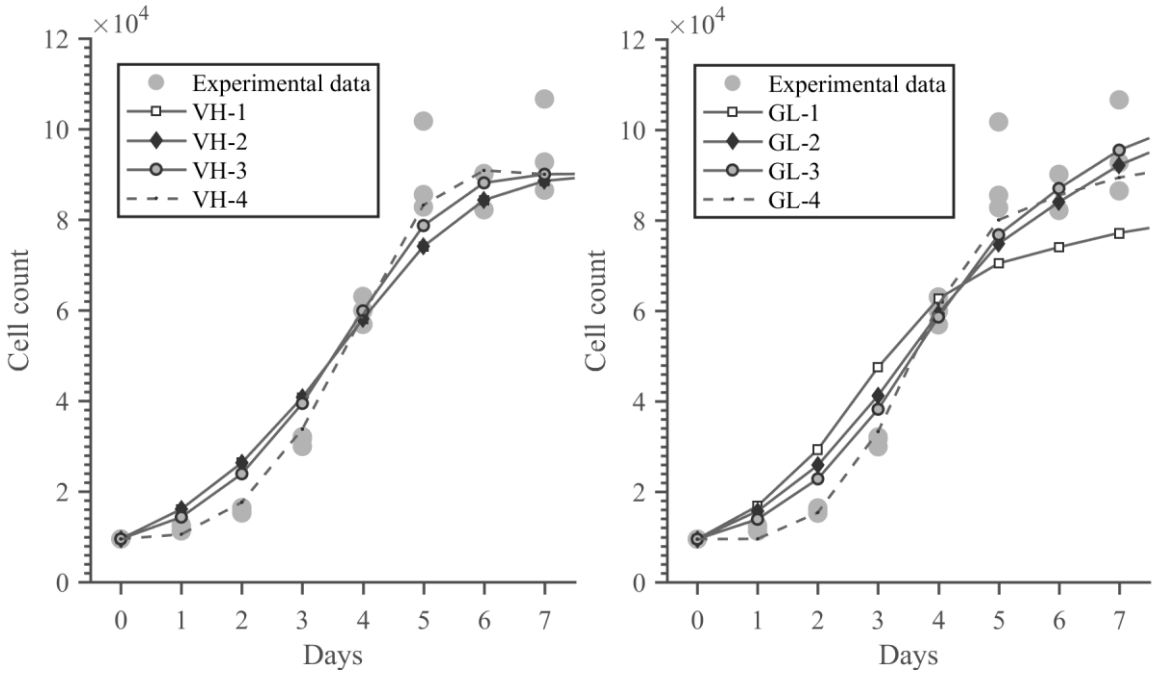

Figure 6.3. An example of the resulting cell counts of the optimised Verhulst (left) and generalised logistic (right) mitotic fractions compared to the experimental data of experiment 13.

The RMSE per day is shown for experimental groups 1 and 2 in Figure 6.4, and for experimental groups 3 and 4 in Figure 6.5. The RMSE across days remains approximately the same for experimental groups 1, 2, and 4. However, the RMSE of experimental group 3 (pHPL) seems to increase exponentially in the first 10 days. The total RMSE for each experimental group is shown in Figure 6.6, and the optimised population limits and division times, grouped by serum supplement, are shown in Figures 6.7 and 6.8 respectively. The larger standard deviations of the FBS VH-4 and GL-4 division times shown in Figure 6.8 are due to certain experiments that were optimised with ξ values closer to unity, i.e. a lag phase that transitions more quickly. For these experiments, the lowest RMSE was associated with a fast lag transition and a higher corresponding division time (i.e. slower division).

In Figure 6.6, no statistically significant difference was found between models (e.g. VH-1 vs. VH-2, VH-2 vs. VH-3, etc.), nor between equivalent Verhulst and generalised logistic models (e.g. VH-1 vs. GL-1) in any of the experimental groups.

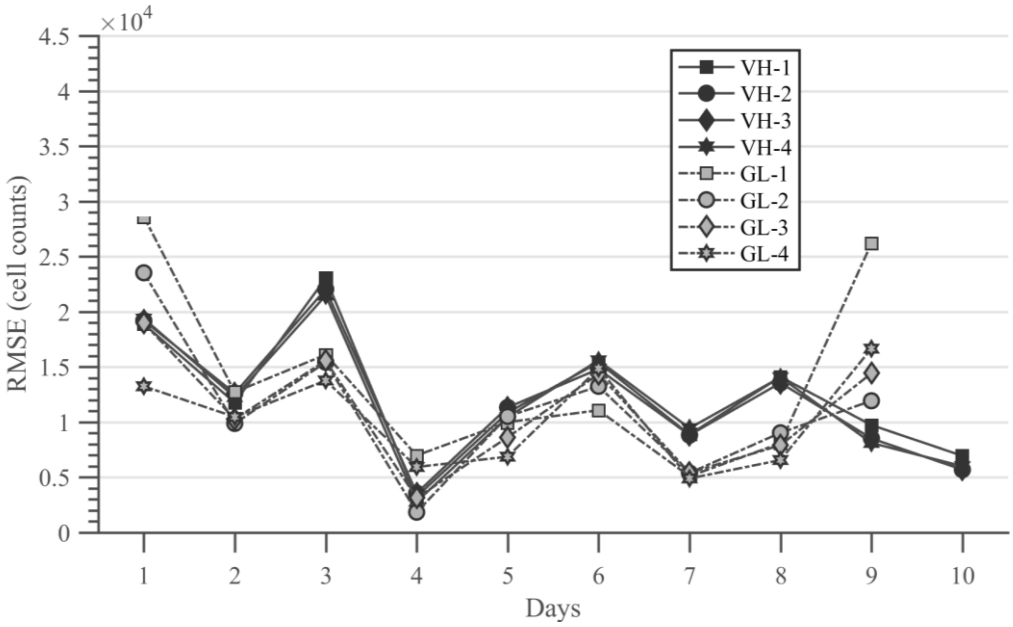

(a)

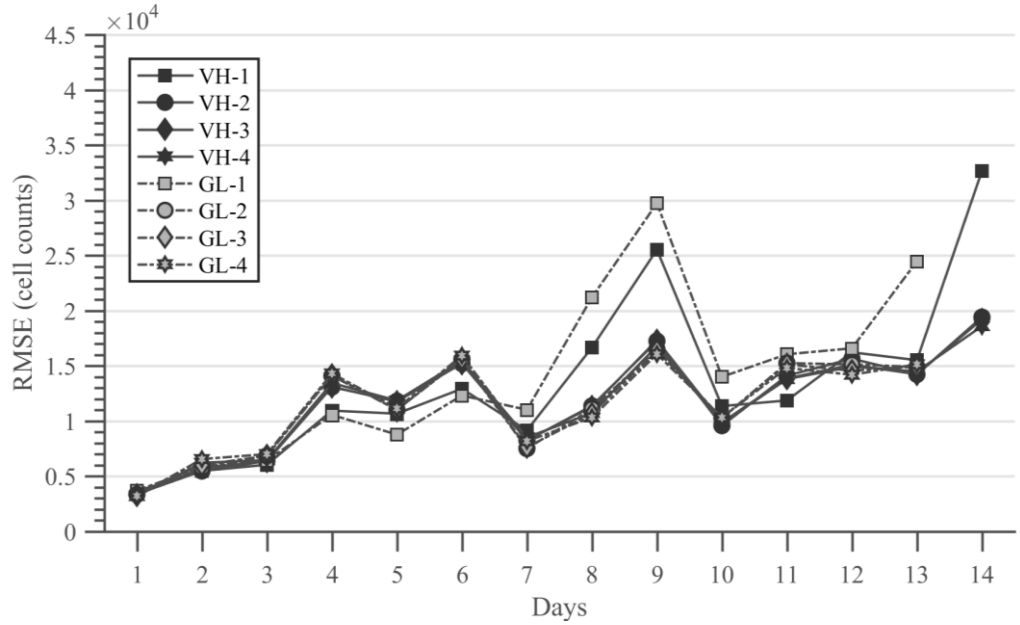

(b)

Figure 6.4. The RMSE per day after optimisation for (a) experimental group 1, and (b) experimental group 2. The RMSE of the generalised logistic models were only calculated for days that spatial dispersion data were available.

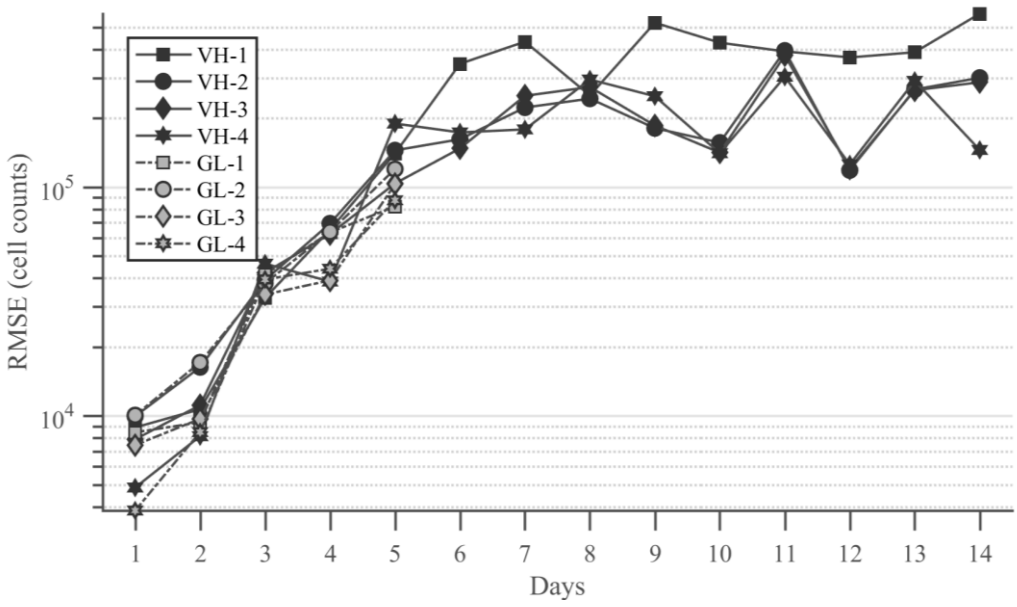

(a)

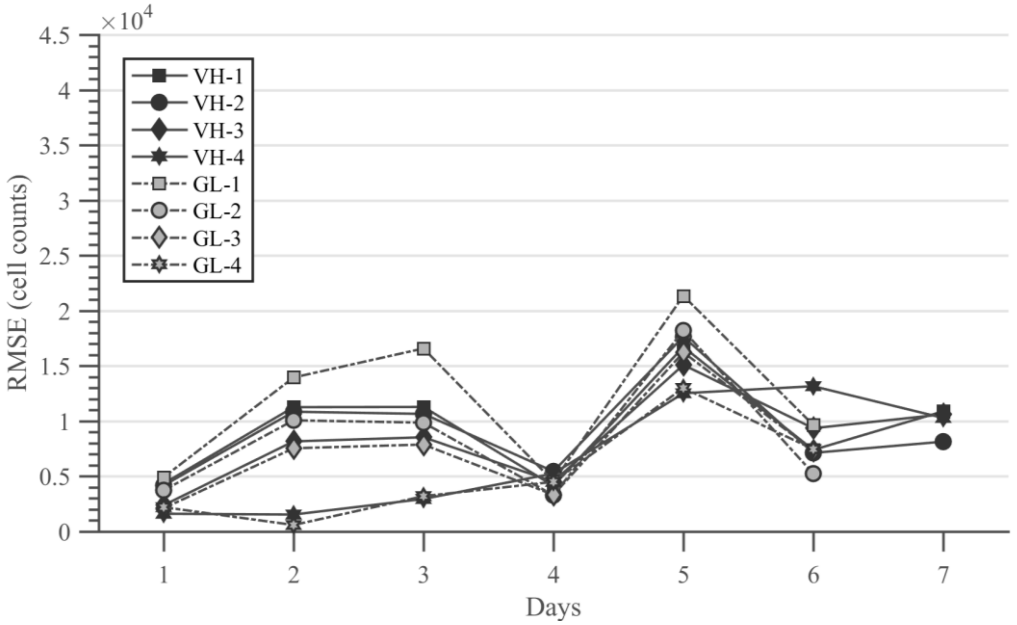

(b)

Figure 6.5. The RMSE per day after optimisation for (a) experimental group 3, and (b) experimental group 4. It should be noted that the vertical axis of (a) is logarithmic. The RMSE of the generalised logistic models were only calculated for days that spatial dispersion data were available.

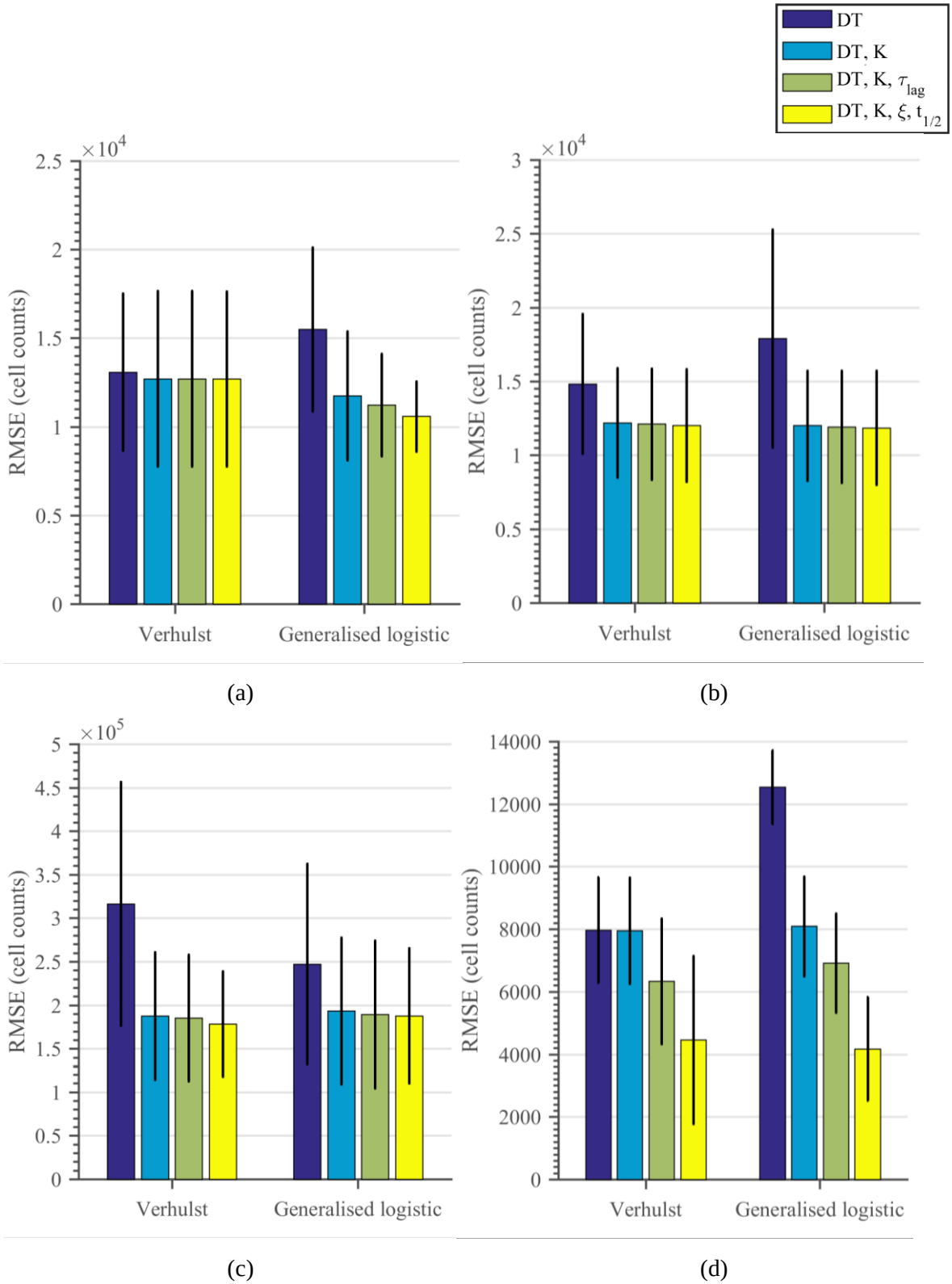

Figure 6.6. The RMSE after optimisation for (a) experimental group 1, (b) experimental group 2, (c) experimental group 3, and (d) experimental group 4.

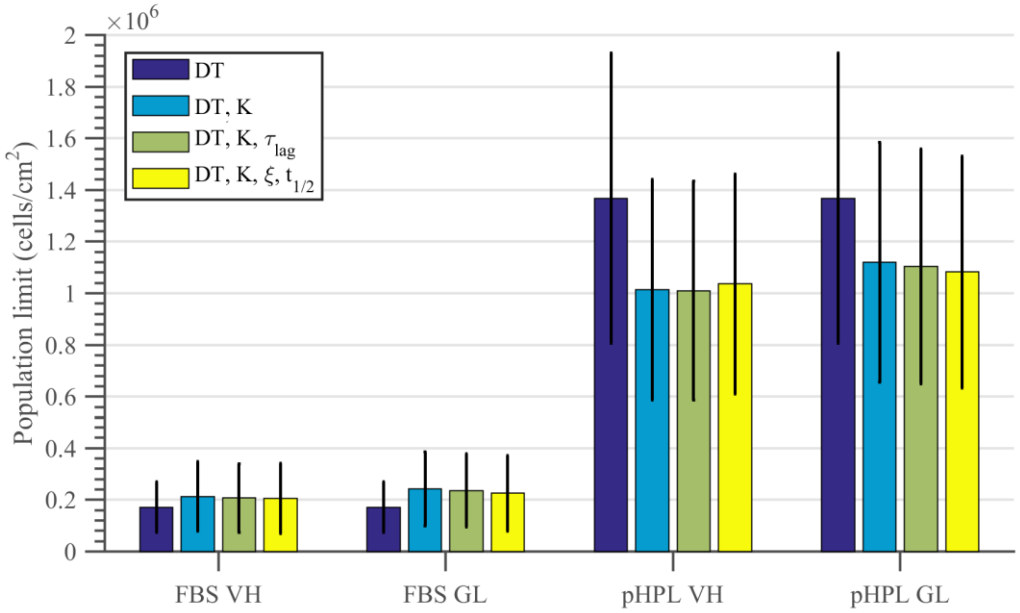

Figure 6.7. The optimised population limit (K) of experiments expanded in FBS (experimental groups 1,2, and 4) and pHPL (experimental group 3), for the Verhulst (VH) and generalised logistic (GL) models

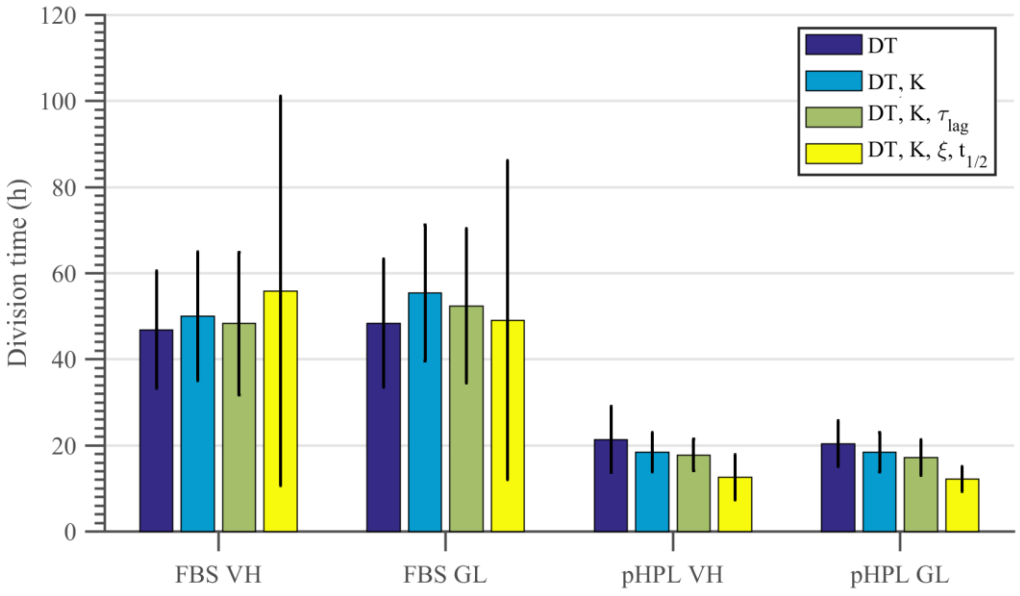

Figure 6.8. The optimised division time (DT) of experiments expanded in FBS (experimental groups 1,2, and 4) and pHPL (experimental group 3), for the Verhulst (VH) and generalised logistic (GL) models.

6.4 PREDICTIVE MODELLING

6.4.1 Assumptions

Models VH-2 and GL-2 were considered for their predictive capacity. It was again assumed that cells were seeded at a known density on a known substrate area, allowing N_0 to be calculated. However, instead of a full set of measurements, measurements are added in daily increments, e.g. $\{N_1\}, \{N_1, N_2\}, \{N_1, N_2, N_3\}$, etc.

6.4.2 Optimisation strategy

Parameters were again optimised by minimising the RMSE. Importantly, only the RMSE for the measured number of days is used for optimisation; however, the results listed in Addendum C list the *total* RMSE across all days.

6.4.3 Results

The complete optimisation results are listed in Addendum C2. Representative examples that visualise the resulting prediction intervals per day are shown in Figure 6.9. The prediction intervals represent the predicted cell counts for each of the optimised parameters within the lowest 5% of RMSE errors. Each prediction interval is indicated in greyscale; lighter grey indicates fewer days' measurements, while darker grey corresponds to additional days' measurements.

The RMSE per day for each experimental group is shown in Figure 6.10. The horizontal axes indicate the number of days' measurements that were used for optimisation prior to prediction. A lower RMSE corresponds to improved predictions. It should be noted that the vertical axis of Figure 6.10 (d) is an order of magnitude lower than the vertical axes of Figures 6.10 (a) to (c).

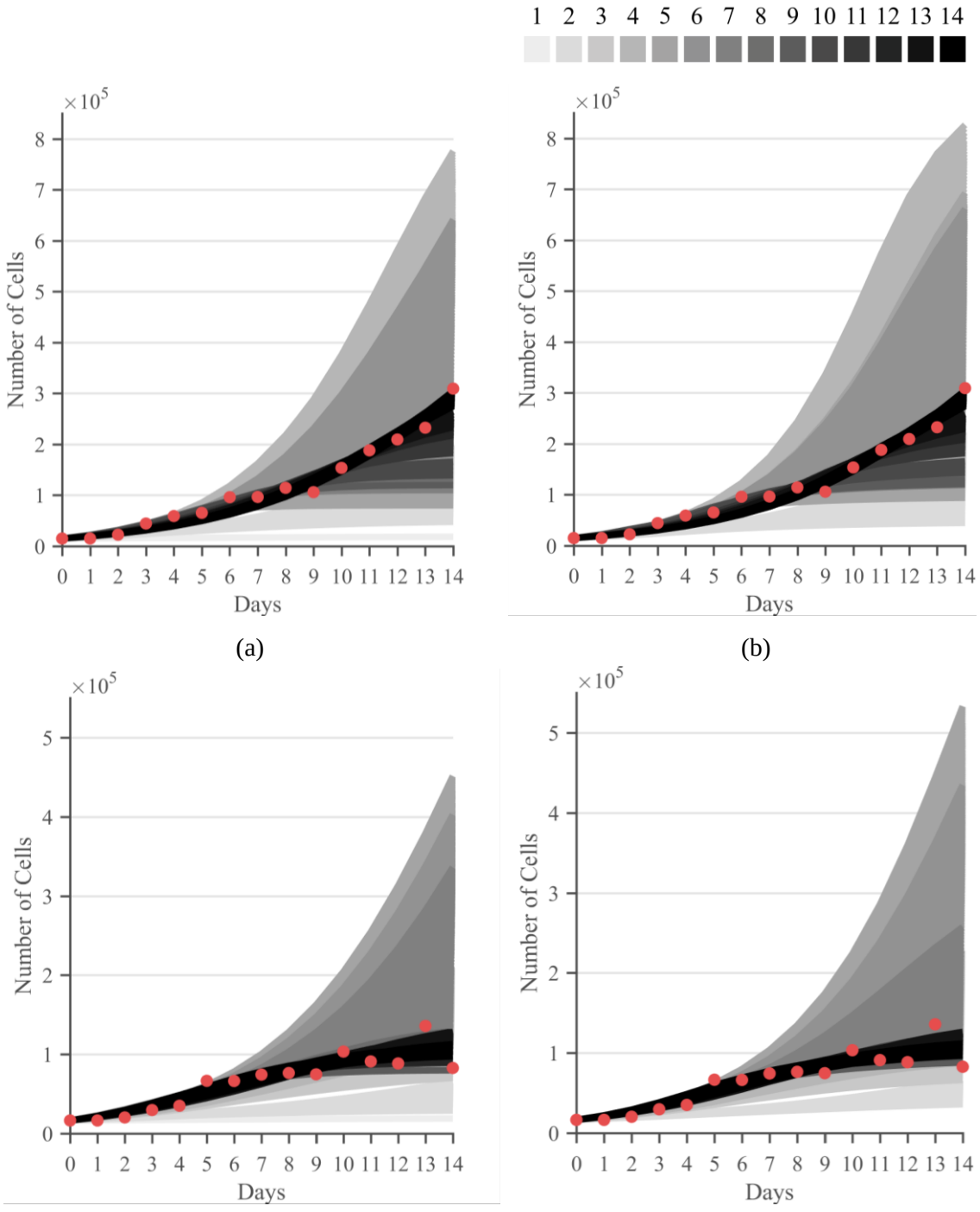

Figure 6.9. Prediction intervals of VH-2 (left) and GL-2 (right) for (a) – (b) experiment 3, and (c) – (d) experiment 5. Lighter grey corresponds to fewer days' measurements, while darker grey corresponds to more days' measurements (cell counts for VH-2 and GL-2, and indices of dispersion for GL-2). Experimental data are represented by red circles.

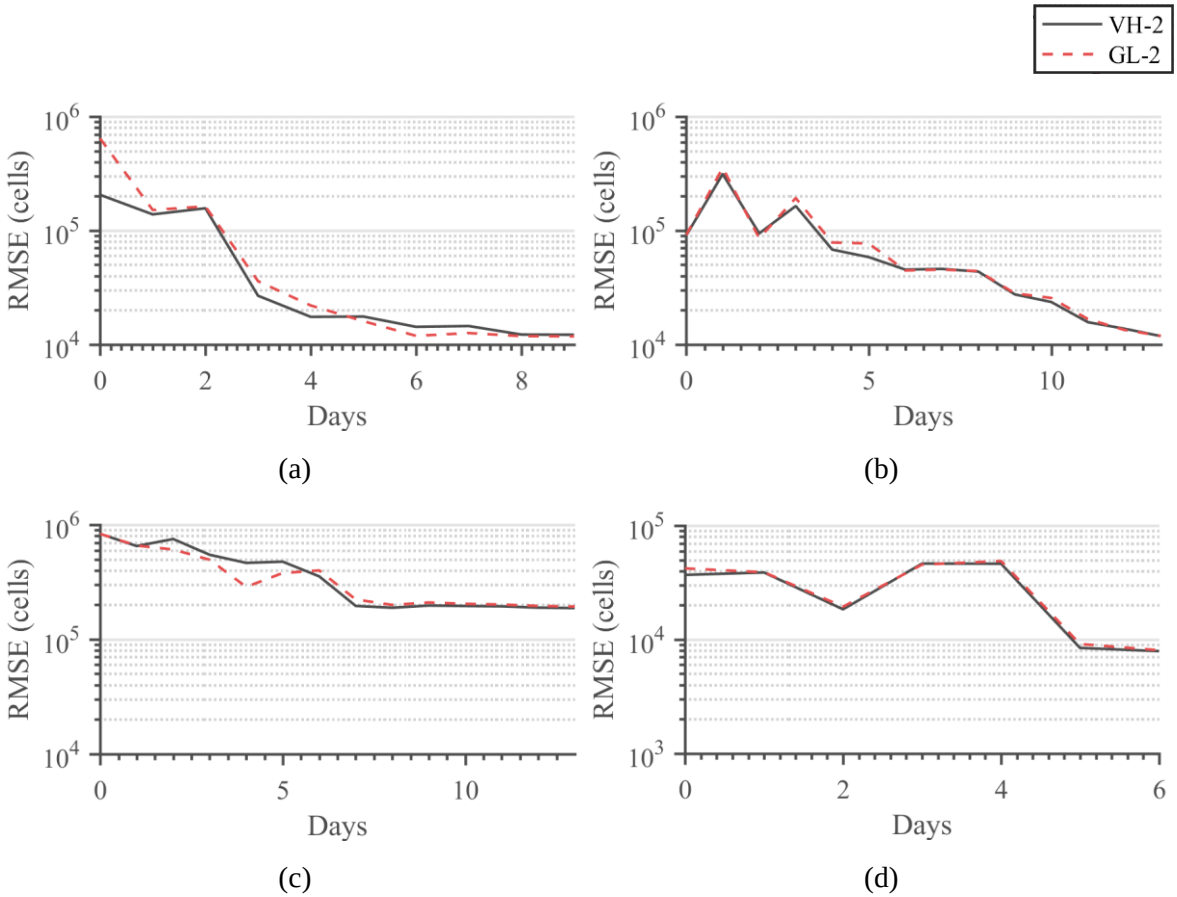

Figure 6.10. The RMSE per day of the VH-2 and GL-2 models, for (a) experimental group 1, (b) experimental group 2, (c) experimental group 3, and (d) experimental group 4. The horizontal axes indicate the number of days' measurements that were used for optimisation prior to prediction; typically, the highest error is associated with the fewest number of measurements, i.e. at day zero. No statistically significant difference was found between VH-2 and GL-2 for any of the number of days' measurements. The vertical axis in (d) is an order of magnitude lower than the axes in (a) - (c).

6.5 DISCUSSION

The error surfaces shown in Figures 6.1 and 6.2 indicate that approximately one optimal solution region exists for each experiment. However, in experiments 3 to 7, the error surface manifested in a "fold", with similarly low RMSE values at a certain DT for a range of K values. These experiments did not seem to reach a plateau, which indicates that the value of K is difficult to estimate without measurements that include a period of slowing growth.

Cells from the same patient, seeded at different seeding densities resulted in a similar DT estimate, but markedly different estimates of K. This could imply that certain effects not included in the models affect the population limit, such as direct cell-to-cell or paracrine interactions that are affected by the initial seeded concentration of cells.

The descriptive RMSE per error group showed no statistically significant difference between any of the models that were considered, nor between equivalent Verhulst or generalised logistic models. The generalised logistic models resulted in consistently higher RMSE when K was not included in optimisation. As expected, when K was optimised, the generalised logistic optimised population limit was higher compared to Verhulst, which illustrates the reduction in mitotic fraction owing to spatial dispersion in addition to confluency. The estimated population limit of pHPL-expanded ASCs was approximately four times greater than FBS-expanded ASCs, while division times were less than half.

The inclusion of additional daily measurements of cell counts (VH and GL models) and indices of dispersion (GL models) decreased the overall RMSE when predicting future cell counts, which provides an indication of the overall suitability of the models. In a few cases, the RMSE briefly increased when an additional measurement was added, which can be attributed to measurement inaccuracies and experimental variability. This highlights the sensitivity of the optimisation approach that was used, which does not compensate for measurement inaccuracies when including additional data points.

The generalised logistic GL-2 model performed similarly to the VH-2 model in all FBS experimental groups, but improved RMSE on days 2 – 5 in the pHPL group; however, this effect was not statistically significant. As discussed in Chapter 5, the indices of dispersion of pHPL-expanded ASCs were substantially higher than those for cells expanded in FBS, and the inclusion of these measurements is the likely reason for this improvement. GL-2 converged to within 10% of the minimum RMSE two days earlier than VH-2 in experiment 1. In experiment 3, VH-2 converged to within 10% of the minimum RMSE a day earlier than GL-2.

6.6 CHAPTER SUMMARY

The population model derived in Chapter 4 was compared to the intra-passage experimental data gathered in Chapter 5, for both the Verhulst and generalised logistic mitotic fractions. Initially, only division time was optimised to the experimental data, after which the population limit, exponential lag parameter, and sigmoidal lag parameters were incrementally added and optimised to minimise the RMSE.

In a descriptive sense, the models corresponded well to the data, and additional variables improved the RMSE. The GL-4 and VH-4 models resulted in the lowest RMSE; however, this effect was not statistically significant.

When employed to predict future cell counts, additional measurements reduced the RMSE; however, it was required that experimental data exhibit slowing of growth before the RMSE reduced to below 50% of the minimum RMSE.

CHAPTER 7 CONCLUSION

7.1 SUMMARY OF CONTRIBUTIONS

The following are the main contributions of this study.

- Individual ASCs were simulated in the form of contact-inhibited cellular automata, and a relationship between confluency, spatial dispersion, and the mitotic fraction was discovered. The cellular automata model was based on previously published models; however, the relationships that were discovered between confluency, spatial dispersion, and the mitotic fraction are new findings.
- A Markov population model was derived that describes ASC proliferation in terms of a time-varying mitotic fraction; a model that has not been previously described in the literature.
- Two models for the time-varying mitotic fraction were derived from existing population models; one from the Verhulst population model, and another from a generalised logistic equation. Both models are well-known and are not newly derived.
- A relationship between spatial dispersion and the parameters of the generalised logistic equation was found using the cellular automata simulation data, and this relationship was described mathematically. These parameters previously had no biological meaning, and their correspondence with biological measurements has not been previously described.
- The Markov population model, using both mitotic fraction models, was compared to measured experimental data from both a descriptive and a predictive perspective.

7.2 SUMMARY OF FINDINGS

A cellular automata model was developed to investigate the fundamental characteristics of contact-inhibited cell proliferation through simulations. It was found that confluency, seeding density, and migration have an important influence on the mitotic fraction. It was then found that this effect can be summarised by measuring the spatial dispersion of cells.

A discrete Markov population model was adapted from first principles as a function of cell cycles. The model was converted to a function of time to allow comparison to experimental measurements. A model for the mitotic fraction was derived from the Verhulst and generalised logistic equations. The Verhulst equation was found to describe the mitotic fraction as only a function of confluency, while the generalised logistic equation included several additional parameters with no biological meaning. A relationship between these unknown parameters and spatial dispersion was discovered and described mathematically. The generalised logistic mitotic fraction provided improved estimates for very low and high seeding densities when compared to cellular automata simulations.

Experimental data of ASCs expanded in FBS and pHPL were made available to this study. The experimental data was found to vary considerably between patients and between replicates of the same patient. Specifically, cell counts of ASCs expanded in pHPL experienced large periodic fluctuations at confluency. It is unclear whether these variations are observations of environmental phenomena, or if they are a result of intra-patient variability.

The experimental data included daily images of the plastic adherent ASCs. The locations of individual cells were labelled on each image, and the indices of dispersion at each day were calculated. Cell counts could also be estimated from the image counts, which allowed for the non-destructive measurement of cell counts and spatial dispersion simultaneously. Directly after seeding, the measured indices of dispersion were close to unity, which corresponded well with the cellular automata simulations. However, in contrast to the simulations, the measured indices of dispersion continued to rise as the cells approached

confluency and did not decrease to zero. This could be a consequence of simulating the cellular automata in an equidistant grid.

The experimental data included measurements of cell cycles; however, the measurements could not distinguish between G0 (non-mitotic) and G1 (mitotic) and could therefore not be used to validate the modelled mitotic fraction.

The population models were tested for validity using the experimental measurements. Cells from the same patient that were seeded at different seeding densities resulted in a similar DT estimate, but different estimates of K. This could imply that certain factors that affect the population limit were not included in the models, such as direct cell-to-cell or paracrine interactions that are influenced by the initial seeded concentration of cells.

The estimated division times corresponded well to population doubling times reported in the literature; specifically, ASCs expanded in pHPL were estimated to have division times of less than half of those expanded in FBS.

When including an estimate of the lag phase, an improved RMSE was achieved in both population models. Although it is expected that the inclusion of additional optimised parameters would reduce the RMSE, this provides evidence that a lag phase exists in ASCs. In a descriptive sense, the models described the data well, and additional variables improved the RMSE. The GL-4 and VH-4 models resulted in the lowest RMSE; however, this effect was not statistically significant.

Additional measurements reduced the RMSE when predicting future cell counts; however, each model required the experimental data to exhibit slowing of growth before the RMSE decreased below 50% of the minimum RMSE.

Prediction using the generalised logistic model requires indices of dispersion, though a predictive model for the indices of dispersion is not known. Using constant indices of dispersion likely limited the predictive capacity of the generalised logistic model.

7.3 CONCLUSIONS

The considerable variation between experimental measurements encumbered the modelling and prediction of ASC behaviour, especially when expanded beyond confluency. This was particularly evident in pHPL-expanded ASCs that reached confluency after a few days. Certain dynamical systems, known as chaotic systems, are highly sensitive to initial conditions. It is possible that ASCs could be sensitive to feedback loops or other cell-to-cell interactions that drastically affect cell counts.

A summary of the descriptive and predictive RMSEs of the VH-2 and GL-2 models are shown in Table 7.1. The Verhulst and generalised prediction models performed similarly when describing and predicting the experimental data, and no statistically significant difference was found between the RMSE of the models. This could indicate that spatial dispersion is not a causal predictor of cell proliferation. However, relatively low indices of dispersion were measured using the micrographs, and additional experimental data would be required to state this conclusively.

Prediction to within 10% of the descriptive RMSE required the inclusion of observations of slowing growth. When considering that slowing growth usually occurs when a population approaches confluency, this limits the utility of the models in a clinical setting. More practically, it appears that the rapid proliferation of ASCs in pHPL means that cells could be harvested in a few weeks, and that predictive models would be less important to patients.

Table 7.1 A summary of the descriptive and predictive RMSEs of the VH-2 and GL-2 models. In the case of predictive RMSE, the day number indicates the number of days' measurements that were used to train the model. Experimental group 4 consisted of only 7 days' measurements; therefore, prediction at 7 days is equivalent to the descriptive case.

Model	Experimental Group	Descriptive RMSE ($\mu \pm \sigma$)	Predictive RMSE Day 1 ($\mu \pm \sigma$)	Predictive RMSE Day 7 ($\mu \pm \sigma$)
VH-2	1	12715 ± 4964	205867 ± 137451	14265 ± 7033
	2	12195 ± 3707	90363 ± 40969	45389 ± 27528
	3	187495 ± 73418	834441 ± 360210	354814 ± 272956
	4	7952 ± 1697	36962 ± 12443	N/A
GL-2	1	11760 ± 3634	643748 ± 746751	11887 ± 3847
	2	12006 ± 3732	91146 ± 41148	44573 ± 27525
	3	193427 ± 84224	834036 ± 360110	400008 ± 232814
	4	8092 ± 1587	42153 ± 7639	N/A

7.4 SUGGESTIONS FOR FURTHER RESEARCH

It is suggested that future research includes additional technical replicates to account for the variability associated with the measurement of ASCs, especially when expanded in pHPL. Measurements of the cell cycle that discriminate between G0 and G1 phases would allow better validation of modelled mitotic fraction.

Live cell imaging could be used to determine the true division time distribution, which may provide further validation of the presented models. The effect of spatial dispersion could be investigated by seeding at various low densities.

The models should be applicable to any contact-inhibited cell, and measurements using endothelial or epithelial cell lines could provide further evidence to validate the models.

A drawback of calculating the index of dispersion using quadrats is that the magnitude is sensitive to different quadrat sizes. Other measures of spatial dispersion that are independent of quadrat sizes could provide more robust measurements.

The developed models can be analysed as a state-space system, and use of prior knowledge, such as through Bayesian methods, could improve the predictive accuracy when including noisy measurements. Prior knowledge near the beginning of culture could include estimation of the population limit using measured cell sizes or prior experimental results. Measurement models for images and flow cytometry that describe the uncertainty of measurement would also be required.

REFERENCES

[1] S. Gottlieb, “Statement from FDA Commissioner Scott Gottlieb, M.D. on FDA’s comprehensive new policy approach to facilitating the development of innovative regenerative medicine products to improve human health,” *U.S. Food and Drug Administration Web Page*, 2017. [Online]. Available: https://www.fda.gov/newsevents/newsroom/pressannouncements/ucm585345.htm. [Accessed: 14-Jul-2018].

[2] J.-P. Gillet, S. Varma, and M. M. Gottesman, “The Clinical Relevance of Cancer Cell Lines,” *JNCI J. Natl. Cancer Inst.*, vol. 105, no. 7, pp. 452–458, Apr. 2013.

[3] B. Deasy, R. Jankowski, and T. Payne, “Modeling stem cell population growth: incorporating terms for proliferative heterogeneity,” *Stem Cells*, vol. 21, pp. 536–545, 2003.

[4] L. Mancuso, M. Liuzzo, and S. Fadda, “Experimental analysis and modelling of in vitro proliferation of mesenchymal stem cells,” *... Prolif.*, 2009.

[5] A. Tsoularis and J. Wallace, “Analysis of logistic growth models,” *Math. Biosci.*, vol. 179, no. 1, pp. 21–55, 2002.

[6] M. A. Tabatabai, Z. Bursac, W. M. Eby, and K. P. Singh, “Mathematical modeling of stem cell proliferation.,” *Med. Biol. Eng. Comput.*, vol. 49, no. 3, pp. 253–62, Mar. 2011.

[7] N. Garijo, R. Manzano, R. Osta, and M. a Perez, “Stochastic cellular automata model of cell migration, proliferation and differentiation: validation with in vitro cultures of muscle satellite cells.,” *J. Theor. Biol.*, vol. 314, pp. 1–9, Dec. 2012.

[8] M. Hoffmann, H. H. Chang, S. Huang, D. E. Ingber, M. Loeffler, and J. Galle, “Noise-driven stem cell and progenitor population dynamics.,” *PLoS One*, vol. 3, no. 8, p. e2922, Jan. 2008.

[9] D. F. E. Ker, L. E. Weiss, S. N. Junkers, M. Chen, Z. Yin, M. F. Sandbothe, S. Huh, S. Eom, R. Bise, E. Osuna-Highley, T. Kanade, and P. G. Campbell, “An engineered approach to stem cell culture: automating the decision process for real-time adaptive subculture of stem cells.,” *PLoS One*, vol. 6, no. 11, p. e27672, Jan. 2011.

[10] T. Tronser, A. A. Popova, and P. A. Levkin, “Miniaturized platform for high-throughput screening of stem cells,” *Curr. Opin. Biotechnol.*, vol. 46, pp. 141–149, 2017.

[11] T. C. Srijaya, T. S. Ramasamy, and N. H. A. Kasim, “Advancing stem cell therapy from bench to bedside: Lessons from drug therapies,” *J. Transl. Med.*, vol. 12, no. 1, 2014.

[12] G. de Wert and C. Mummery, “Human embryonic stem cells: research, ethics and policy,” *Hum. Reprod.*, vol. 18, no. 4, pp. 672–682, Apr. 2003.

[13] A. Gratwohl, H. Baldomero, and J. Passweg, “Hematopoietic stem cell transplantation activity in Europe,” *Curr. Opin. Hematol.*, vol. 20, no. 6, pp. 485–493, 2013.

[14] J. R. Passweg, H. Baldomero, P. Bader, C. Bonini, R. F. Duarte, C. Dufour, A. Gennery, N. Kröger, J. Kuball, F. Lanza, S. Montoto, A. Nagler, J. A. Snowden, J. Styczynski, and M. Mohty, “Use of haploidentical stem cell transplantation continues to increase: the 2015 European Society for Blood and Marrow Transplant activity survey report,” *Bone Marrow Transplant.*, vol. 52, p. 811, Mar. 2017.

[15] J. M. Gimble, B. A. Bunnell, T. Frazier, B. Rowan, F. Shah, C. Thomas-Porch, and X. Wu, “Adipose-derived stromal/stem cells: A primer,” *Organogenesis*, vol. 9, no. 1, pp. 139–146, 2013.

[16] J. Gimble and F. Guilak, “Adipose-derived adult stem cells: isolation, characterization, and differentiation potential.,” *Cytotherapy*, vol. 5, no. 5, pp. 362–9, Jan. 2003.

[17] P. Bourin, M. Gadelorge, J.-A. Peyrafitte, S. Fleury-Cappellesso, M. Gomez, C. Rage, and L. Sensebé, “Mesenchymal Progenitor Cells: Tissue Origin, Isolation and Culture.,” *Transfus. Med. Hemother.*, vol. 35, no. 3, pp. 160–167, Jan. 2008.

[18] P. C. Baer and H. Geiger, “Adipose-derived mesenchymal stromal/stem cells: tissue localization, characterization, and heterogeneity.,” *Stem Cells Int.*, vol. 2012, p. 812693, Jan. 2012.

[19] E. Oberbauer, C. Steffenhagen, C. Wurzer, C. Gabriel, H. Redl, and S. Wolbank, “Enzymatic and non-enzymatic isolation systems for adipose tissue-derived cells: current state of the art,” *Cell Regen.*, vol. 4, p. 7, Sep. 2015.

[20] M. Coelho, T. Oliveira, and R. Fernandes, “State of the art paper Biochemistry of adipose tissue: an endocrine organ,” *Arch. Med. Sci.*, vol. 9, no. 2, pp. 191–200, 2013.

[21] E. Ottaviani, D. Malagoli, and C. Franceschi, “The evolution of the adipose tissue: A neglected enigma,” *Gen. Comp. Endocrinol.*, vol. 174, no. 1, pp. 1–4, 2011.

[22] P. Bourin, B. A. Bunnell, L. Casteilla, M. Dominici, A. J. Katz, K. L. March, H. Redl, J. P. Rubin, K. Yoshimura, and J. M. Gimble, "Stromal cells from the adipose tissue-derived stromal vascular fraction and culture expanded adipose tissue-derived stromal/stem cells: a joint statement of the International Federation for Adipose Therapeutics and Science (IFATS) and the International So," *Cytotherapy*, vol. 15, no. 6, pp. 641–8, Jun. 2013.

[23] M. Rodbell, "The metabolism of isolated fat cells. IV. Regulation of release of protein by lipolytic hormones and insulin.," *J. Biol. Chem.*, vol. 241, no. 17, pp. 3909–3917, 1966.

[24] P. a Zuk, M. Zhu, H. Mizuno, J. Huang, J. W. Futrell, a J. Katz, P. Benhaim, H. P. Lorenz, and M. H. Hedrick, "Multilineage cells from human adipose tissue: implications for cell-based therapies.," *Tissue Eng.*, vol. 7, no. 2, pp. 211–28, Apr. 2001.

[25] P. A. Zuk, M. Zhu, P. Ashjian, D. A. De Ugarte, J. I. Huang, H. Mizuno, Z. C. Alfonso, J. K. Fraser, P. Benhaim, and M. H. Hedrick, "Human adipose tissue is a source of multipotent stem cells," *Mol. Biol. Cell*, vol. 13, no. 12, pp. 4279–4295, 2002.

[26] M. F. Pittenger, A. M. Mackay, S. C. Beck, R. K. Jaiswal, R. Douglas, J. D. Mosca, M. A. Moorman, D. W. Simonetti, S. Craig, and D. R. Marshak, "Multilineage Potential of Adult Human Mesenchymal Stem Cells," *Science (80-.).*, vol. 284, no. 5411, p. 143 LP-147, Apr. 1999.

[27] M. Dominici, K. Le Blanc, I. Mueller, I. Slaper-Cortenbach, F. Marini, D. Krause, R. Deans, a Keating, D. Prockop, and E. Horwitz, "Minimal criteria for defining multipotent mesenchymal stromal cells. The International Society for Cellular Therapy position statement.," *Cytotherapy*, vol. 8, no. 4, pp. 315–7, Jan. 2006.

[28] P. Bianco, "'Mesenchymal' Stem Cells.," *Annu. Rev. Cell Dev. Biol.*, no. August, pp. 1–28, Aug. 2014.

[29] A. Schellenberg, T. Stiehl, P. Horn, S. Joussen, N. Pallua, A. D. Ho, and W. Wagner, "Population dynamics of mesenchymal stromal cells during culture expansion.," *Cytotherapy*, vol. 14, no. 4, pp. 401–11, Apr. 2012.

[30] M. Strioga, S. Viswanathan, A. Darinskas, O. Slaby, and J. Michalek, "Same or not the same? Comparison of adipose tissue-derived versus bone marrow-derived mesenchymal stem and stromal cells.," *Stem Cells Dev.*, vol. 21, no. 14, pp. 2724–2752, Sep. 2012.

[31] M. Dominici, K. Le Blanc, I. Mueller, I. Slaper-Cortenbach, F. Marini, D. Krause, R. Deans, a Keating, D. Prockop, and E. Horwitz, "Minimal criteria for defining multipotent mesenchymal stromal cells. The International Society for Cellular Therapy position statement.," *Cytotherapy*, vol. 8, no. 4, pp. 315–7, Jan. 2006.

[32] J. A. Aronowitz, R. A. Lockhart, and C. S. Hakakian, “Mechanical versus enzymatic isolation of stromal vascular fraction cells from adipose tissue,” *Springerplus*, vol. 4, p. 713, Nov. 2015.

[33] M. Haack-Sørensen, B. Follin, M. Juhl, S. K. Brorsen, R. H. Søndergaard, J. Kastrup, and A. Ekblond, “Culture expansion of adipose derived stromal cells. A closed automated Quantum Cell Expansion System compared with manual flask-based culture,” *J. Transl. Med.*, vol. 14, no. 1, p. 319, 2016.

[34] Y. Zhu, T. Liu, K. Song, X. Fan, X. Ma, and Z. Cui, “Adipose-derived stem cell: a better stem cell than BMSC.,” *Cell Biochem. Funct.*, vol. 26, no. 6, pp. 664–675, Aug. 2008.

[35] A. Schäffler and C. Büchler, “Concise review: adipose tissue-derived stromal cells--basic and clinical implications for novel cell-based therapies.,” *Stem Cells*, vol. 25, no. 4, pp. 818–27, Apr. 2007.

[36] M. Konno, A. Hamabe, S. Hasegawa, H. Ogawa, T. Fukusumi, S. Nishikawa, K. Ohta, Y. Kano, M. Ozaki, Y. Noguchi, D. Sakai, T. Kudoh, K. Kawamoto, H. Eguchi, T. Satoh, M. Tanemura, H. Nagano, Y. Doki, M. Mori, and H. Ishii, “Adipose-derived mesenchymal stem cells and regenerative medicine.,” *Dev. Growth Differ.*, vol. 55, no. 3, pp. 309–18, Apr. 2013.

[37] C. Maucksch, E. M. Vazey, R. J. Gordon, and B. Connor, “Stem cell-based therapy for Huntington’s disease.,” *J. Cell. Biochem.*, vol. 114, no. 4, pp. 754–63, Apr. 2013.

[38] L. Yildirimer, N. T. K. Thanh, and A. M. Seifalian, “Skin regeneration scaffolds: a multimodal bottom-up approach.,” *Trends Biotechnol.*, vol. 30, no. 12, pp. 638–48, Dec. 2012.

[39] W.-S. Kim, B.-S. Park, J.-H. Sung, J.-M. Yang, S.-B. Park, S.-J. Kwak, and J.-S. Park, “Wound healing effect of adipose-derived stem cells: a critical role of secretory factors on human dermal fibroblasts.,” *J. Dermatol. Sci.*, vol. 48, no. 1, pp. 15–24, Oct. 2007.

[40] G. R. Erickson, J. M. Gimble, D. M. Franklin, H. E. Rice, H. Awad, and F. Guilak, “Chondrogenic potential of adipose tissue-derived stromal cells in vitro and in vivo.,” *Biochem. Biophys. Res. Commun.*, vol. 290, no. 2, pp. 763–9, Jan. 2002.

[41] L. Wu, X. Cai, S. Zhang, M. Karperien, and Y. Lin, “Regeneration of articular cartilage by adipose tissue derived mesenchymal stem cells: perspectives from stem cell biology and molecular medicine.,” *J. Cell. Physiol.*, vol. 228, no. 5, pp. 938–44, May 2013.

[42] B. O. Diekman and F. Guilak, “Stem cell-based therapies for osteoarthritis: challenges and opportunities.,” *Curr. Opin. Rheumatol.*, vol. 25, no. 1, pp. 119–26, Jan. 2013.

[43] J. A. Dykstra, T. Facile, R. J. Patrick, K. R. Francis, S. Milanovich, J. M. Weimer, and D. J. Kota, "Concise Review: Fat and Furious: Harnessing the Full Potential of Adipose-Derived Stromal Vascular Fraction," *Stem Cells Transl. Med.*, vol. 6, no. 4, pp. 1096–1108, 2017.

[44] J. Pak, J. H. Lee, K. S. Park, M. Park, L.-W. Kang, and S. H. Lee, "Current use of autologous adipose tissue-derived stromal vascular fraction cells for orthopedic applications," *J. Biomed. Sci.*, vol. 24, no. 1, p. 9, 2017.

[45] J. M. Gimble, A. J. Katz, and B. a Bunnell, "Adipose-derived stem cells for regenerative medicine.," *Circ. Res.*, vol. 100, no. 9, pp. 1249–60, May 2007.

[46] R. I. Freshney, *Culture of Animal Cells*. Hoboken, NJ, USA: John Wiley & Sons, Inc., 2010.

[47] J. M. . Gimble, B. A. . Bunnell, and F. . Guilak, "Human adipose-derived cells: An update on the transition to clinical translation," *Regen. Med.*, vol. 7, no. 2, pp. 225–235, 2012.

[48] L. Frese, P. E. Dijkman, and S. P. Hoerstrup, "Adipose Tissue-Derived Stem Cells in Regenerative Medicine," *Transfus. Med. Hemotherapy*, vol. 43, no. 4, pp. 268–274, 2016.

[49] A. Bajek, N. Gurtowska, J. Olkowska, L. Kazmierski, M. Maj, and T. Drewa, "Adipose-Derived Stem Cells as a Tool in Cell-Based Therapies," *Arch. Immunol. Ther. Exp. (Warsz).*, vol. 64, no. 6, pp. 443–454, 2016.

[50] S.-F. T. Kølle, A. Fischer-Nielsen, A. B. Mathiasen, J. J. Elberg, R. S. Oliveri, P. V Glovinski, J. Kastrup, M. Kirchhoff, B. S. Rasmussen, M.-L. M. Talman, C. Thomsen, E. Dickmeiss, and K. T. Drzewiecki, "Enrichment of autologous fat grafts with ex-vivo expanded adipose tissue-derived stem cells for graft survival: a randomised placebo-controlled trial.," *Lancet*, vol. 382, no. 9898, pp. 1113–20, Sep. 2013.

[51] Y. Zhao and H. Zhang, "Update on the mechanisms of homing of adipose tissue–derived stem cells," *Cytotherapy*, vol. 18, no. 7, pp. 816–827, Jul. 2016.

[52] K. S. Johal, V. C. Lees, and A. J. Reid, "Adipose-derived stem cells: selecting for translational success.," *Regen. Med.*, vol. 10, no. 1, pp. 79–96, Jan. 2015.

[53] S. Riis, V. Zachar, S. Boucher, M. C. Vemuri, C. P. Pennisi, and T. Fink, "Critical steps in the isolation and expansion of adipose-derived stem cells for translational therapy," *Expert Rev. Mol. Med.*, vol. 17, no. e11, pp. 1–11, 2015.

[54] S. Trojahn Kølle, R. S. Oliveri, P. V Glovinski, M. Kirchhoff, A. B. Mathiasen, J. J. Elberg, P. S. Andersen, K. T. Drzewiecki, and A. Fischer-nielsen, "Pooled human lysate versus fetal bovine serum — Investigating the proliferation rate , chromosome stability and angiogenic potential of human adipose tissueederived stem cells

intended for clinical use," *Cytotherapy*, vol. 15, no. 9, pp. 1086–1097, 2013.

[55] S.-F. Trojahn Kølle, R. S. Oliveri, P. V Glovinski, M. Kirchhoff, A. B. Mathiasen, J. J. Elberg, P. S. Andersen, K. T. Drzewiecki, and A. Fischer-Nielsen, "Pooled human platelet lysate versus fetal bovine serum-investigating the proliferation rate, chromosome stability and angiogenic potential of human adipose tissue-derived stem cells intended for clinical use.," *Cytotherapy*, vol. 15, no. 9, pp. 1086–97, Sep. 2013.

[56] O. Rogulska, Y. Petrenko, and A. Petrenko, "DMSO-free cryopreservation of adipose-derived mesenchymal stromal cells: expansion medium affects post-thaw survival," *Cytotechnology*, vol. 69, no. 2, pp. 265–276, 2017.

[57] J. Folkman and A. Moscona, "Role of cell shape in growth control," *Nature*, vol. 273, p. 345, Jun. 1978.

[58] D. Cholewa, T. Stieh, A. Schellenberg, G. Bokermann, S. Joussen, C. Koch, T. Walenda, N. Pallua, A. Marciniak-Czochra, C. V Suschek, and W. Wagner, "Expansion of adipose mesenchymal stromal cells is affected by human platelet lysate and plating density," *Cell Transplant.*, vol. 20, no. 9, pp. 1409–1422, 2011.

[59] A. D. Dudakovic, E. Camilleri, S. M. Riester, E. A. Lewallen, S. Kvasha, X. Chen, D. J. Radel, J. M. Anderson, A. A. Nair, J. M. Evans, A. J. Krych, J. Smith, D. R. Deyle, J. L. Stein, G. S. Stein, H.-J. Im, S. M. Cool, J. J. Westendorf, S. Kakar, A. B. Dietz, and A. J. van Wijnen, "High-resolution molecular validation of self-renewal and spontaneous differentiation in adipose-tissue derived human mesenchymal stem cells cultured in human platelet lysate," *J. Cell. Biochem.*, vol. 115, no. 10, pp. 1816–1828, Oct. 2014.

[60] D. S. Kim, M. W. Lee, K. H. Yoo, T.-H. Lee, H. J. Kim, I. K. Jang, Y. H. Chun, H. J. Kim, S. J. Park, S. H. Lee, M. H. Son, H. L. Jung, K. W. Sung, and H. H. Koo, "Gene expression profiles of human adipose tissue-derived mesenchymal stem cells are modified by cell culture density.," *PLoS One*, vol. 9, no. 1, p. e83363, Jan. 2014.

[61] R. I. Freshney, "Basic Principles of Cell Culture," in *Culture of Cells for Tissue Engineering*, John Wiley & Sons, Inc., 2005, pp. 1–22.

[62] P. Bogdan, B. M. Deasy, B. Gharaibeh, T. Roehrs, and R. Marculescu, "Heterogeneous Structure of Stem Cells Dynamics: Statistical Models and Quantitative Predictions," *Sci. Rep.*, vol. 4, p. 4826, Apr. 2014.

[63] F. Agostini, J. Polesel, M. Battiston, E. Lombardi, S. Zanolin, A. Da Ponte, G. Astori, C. Durante, and M. Mazzucato, "Standardization of platelet releasate products for clinical applications in cell therapy: a mathematical approach," *J. Transl. Med.*, vol. 15, no. 1, p. 107, 2017.

[64] M. J. Oedayrajsingh-Varma, S. M. van Ham, M. Knippenberg, M. N. Helder, J. Klein-Nulend, T. E. Schouten, M. J. P. F. Ritt, and F. J. van Milligen, "Adipose

tissue-derived mesenchymal stem cell yield and growth characteristics are affected by the tissue-harvesting procedure.," *Cytotherapy*, vol. 8, no. 2, pp. 166–77, Jan. 2006.

[65] P. C. Baer, N. Griesche, W. Luttmann, R. Schubert, A. Luttmann, and H. Geiger, "Human adipose-derived mesenchymal stem cells in vitro: evaluation of an optimal expansion medium preserving stemness.," *Cytotherapy*, vol. 12, no. 1, pp. 96–106, Jan. 2010.

[66] P. Bourin, B. a Bunnell, L. Casteilla, M. Dominici, A. J. Katz, K. L. March, H. Redl, J. P. Rubin, K. Yoshimura, and J. M. Gimble, "Stromal cells from the adipose tissue-derived stromal vascular fraction and culture expanded adipose tissue-derived stromal/stem cells: a joint statement of the International Federation for Adipose Therapeutics and Science (IFATS) and the International So," *Cytotherapy*, vol. 15, no. 6, pp. 641–8, Jun. 2013.

[67] L. Aust, B. Devlin, S. J. Foster, Y. D. C. Halvorsen, K. Hicok, T. du Laney, A. Sen, G. D. Willingmyre, and J. M. Gimble, "Yield of human adipose-derived adult stem cells from liposuction aspirates.," *Cytotherapy*, vol. 6, no. 1, pp. 7–14, Jan. 2004.

[68] W. Wu, L. Niklason, and D. M. Steinbacher, "The effect of age on human adipose-derived stem cells.," *Plast. Reconstr. Surg.*, vol. 131, no. 1, pp. 27–37, Jan. 2013.

[69] G. Astori, F. Vignati, S. Bardelli, M. Tubio, M. Gola, V. Albertini, F. Bambi, G. Scali, D. Castelli, V. Rasini, G. Soldati, and T. Moccetti, "'In vitro' and multicolor phenotypic characterization of cell subpopulations identified in fresh human adipose tissue stromal vascular fraction and in the derived mesenchymal stem cells.," *J. Transl. Med.*, vol. 5, no. 1, p. 55, Jan. 2007.

[70] A. Miranville, C. Heeschen, C. Sengenès, C. A. Curat, R. Busse, and A. Bouloumié, "Improvement of postnatal neovascularization by human adipose tissue-derived stem cells.," *Circulation*, vol. 110, no. 3, pp. 349–55, Jul. 2004.

[71] K. Yoshimura, T. Shigeura, D. Matsumoto, T. Sato, Y. Takaki, E. Aiba-Kojima, K. Sato, K. Inoue, T. Nagase, I. Koshima, and K. Gonda, "Characterization of freshly isolated and cultured cells derived from the fatty and fluid portions of liposuction aspirates.," *J. Cell. Physiol.*, vol. 208, no. 1, pp. 64–76, Jul. 2006.

[72] M. Brzoska, H. Geiger, S. Gauer, and P. Baer, "Epithelial differentiation of human adipose tissue-derived adult stem cells.," *Biochem. Biophys. Res. Commun.*, vol. 330, no. 1, pp. 142–50, Apr. 2005.

[73] L. Mancuso, M. I. Liuzzo, S. Fadda, M. Pisu, a Cincotti, M. Arras, E. Desogus, F. Piras, G. Piga, G. La Nasa, a Concas, and G. Cao, "Experimental analysis and modelling of in vitro proliferation of mesenchymal stem cells.," *Cell Prolif.*, vol. 42, no. 5, pp. 602–616, 2009.

[74] M. Vogels, R. Zoeckler, D. M. Stasiw, and L. C. Cerny, "P. F. Verhulst's 'notice sur

la loi que la populations suit dans son accroissement' from correspondence mathematique et physique. Ghent, vol. X, 1838," *J. Biol. Phys.*, vol. 3, no. 4, pp. 183–192, Dec. 1975.

[75] I. Bianchini, M. B. Cunha-Santino, J. A. M. Milan, C. J. Rodrigues, and J. H. P. Dias, "Growth of Hydrilla verticillata (L.f.) Royle under controlled conditions," *Hydrobiologia*, vol. 644, no. 1, pp. 301–312, Mar. 2010.

[76] I. Bianchini, M. B. Cunha-Santino, J. A. M. Milan, C. J. Rodrigues, and J. H. P. Dias, "Model parameterization for the growth of three submerged aquatic macrophytes," *J. Aquat. Plant Manag.*, vol. 53, no. January, pp. 64–73, 2015.

[77] P.-M. Juneau, A. Garnier, and C. Duchesne, "Selection and tuning of a fast and simple phase-contrast microscopy image segmentation algorithm for measuring myoblast growth kinetics in an automated manner.," *Microsc. Microanal.*, vol. 19, no. 4, pp. 855–66, Aug. 2013.

[78] F. J. Richards, "A Flexible Growth Function for Empirical Use," *J. Exp. Bot.*, vol. 10, no. 2, pp. 290–301, 1959.

[79] A. Tsoularis and J. Wallace, "Analysis of logistic growth models," *Math. Biosci.*, vol. 179, pp. 21–55, 2002.

[80] J. Von Neumann, "The general and logical theory of automata," *Cereb. Mech. Behav.*, pp. 1–41, 1951.

[81] S. Wolfram, "Cellular automata as models of complexity," *Nature*, vol. 311, no. 5985, pp. 419–424, Oct. 1984.

[82] Y. Lee, S. Kouvroukoglou, L. V McIntire, and K. Zygourakis, "A cellular automaton model for the proliferation of migrating contact-inhibited cells," *Biophys. J.*, vol. 69, no. 4, pp. 1284–1298, 1995.

[83] H.-F. Chieh, F.-C. Su, S.-C. Lin, M.-R. Shen, and J.-D. Liao, "Migration patterns and cell functions of adipose-derived stromal cells on self-assembled monolayers with different functional groups.," *J. Biomater. Sci. Polym. Ed.*, vol. 24, no. 1, pp. 94–117, Jan. 2013.

[84] G. M. Cooper, *The Cell: A Molecular Approach*. ASM Press, 2000.

[85] M. Liu, H. Lei, P. Dong, X. Fu, Z. Yang, Y. Yang, J. Ma, X. Liu, Y. Cao, and R. Xiao, "Adipose-Derived Mesenchymal Stem Cells from the Elderly Exhibit Decreased Migration and Differentiation Abilities with Senescent Properties," *Cell Transplant.*, vol. 26, no. 9, pp. 1505–1519, Sep. 2017.

[86] S. J. Baek, S. K. Kang, and J. C. Ra, "In vitro migration capacity of human adipose tissue-derived mesenchymal stem cells reflects their expression of receptors for chemokines and growth factors," *Exp. Mol. Med.*, vol. 43, p. 596, Aug. 2011.

[87] A. Saraste, “Morphologic criteria and detection of apoptosis.,” *Herz*, vol. 24, no. 3, pp. 189–195, May 1999.

[88] J. L. Sherley, P. B. Stadler, and J. S. Stadler, “A quantitative method for the analysis of mammalian cell proliferation in culture in terms of dividing and non-dividing cells.,” *Cell Prolif.*, vol. 28, no. 3, pp. 137–144, Mar. 1995.

[89] J. Stewart, “Calculus: Early Transcendentals,” Thomson/Brooks/Cole, 2003, pp. 760–761.

[90] M. Rieseberg, C. Kasper, K. F. Reardon, and T. Scheper, “Flow cytometry in biotechnology,” *Appl. Microbiol. Biotechnol.*, vol. 56, no. 3, pp. 350–360, 2001.

[91] C. Dessels, “Expansion of human adipose-derived stem cells: Human alternatives to foetal bovine serum,” University of Pretoria, 2016.

[92] G. Topman, O. Sharabani-Yosef, and A. Gefen, “A method for quick, low-cost automated confluency measurements.,” *Microsc. Microanal.*, vol. 17, no. 6, pp. 915–922, Dec. 2011.

[93] K. P. Dempsey, J. B. Richardson, and K. P. Lam, “On measuring cell confluence in phase contrast microscopy,” 2014, vol. 8947, p. 89471I–8947–12.

[94] N. Jaccard, L. D. Griffin, A. Keser, R. J. Macown, A. Super, F. S. Veraitch, and N. Szita, “Automated method for the rapid and precise estimation of adherent cell culture characteristics from phase contrast microscopy images.,” *Biotechnol. Bioeng.*, vol. 111, no. 3, pp. 504–17, Mar. 2014.

[95] Z. Darzynkiewicz, G. Juan, and E. Bedner, “Determining Cell Cycle Stages by Flow Cytometry,” in *Current Protocols in Cell Biology*, John Wiley & Sons, Inc., 2001.

[96] M. E. Kandel, M. Fanous, C. Best-Popescu, and G. Popescu, “Real-time halo correction in phase contrast imaging,” *bioRxiv*, Jan. 2017.

[97] C. Dessels, C. Durandt, and M. Pepper, “Comparison of human platelet lysate alternatives using expired and freshly isolated platelet concentrates for adipose-derived stromal cell expansion.,” *Platelets*, 2018.

[98] E. C. Jensen, “Use of Fluorescent Probes: Their Effect on Cell Biology and Limitations,” *Anat. Rec. Adv. Integr. Anat. Evol. Biol.*, vol. 295, no. 12, pp. 2031–2036, Dec. 2012.

[99] C. A. Schneider, W. S. Rasband, and K. W. Eliceiri, “NIH Image to ImageJ: 25 years of image analysis,” *Nat. Methods*, vol. 9, p. 671, Jun. 2012.

ADDENDUM A LIVE CELL IMAGING

A.1 EXPERIMENTAL SETUP

Cells supplemented with FBS were incubated in a transparent incubator for 18 hours, and a phase-contract micrograph of a specific area was automatically captured every 5 minutes. The incubator regulated the temperature at 37 degrees Celsius; however, CO_2 was not regulated. Instead, a chemical buffering agent, 4-(2-hydroxyethyl)-1-piperazineethanesulfonic acid (HEPES), was added to maintain a physiological pH. A depiction of the experimental setup is shown in Figure A.1.

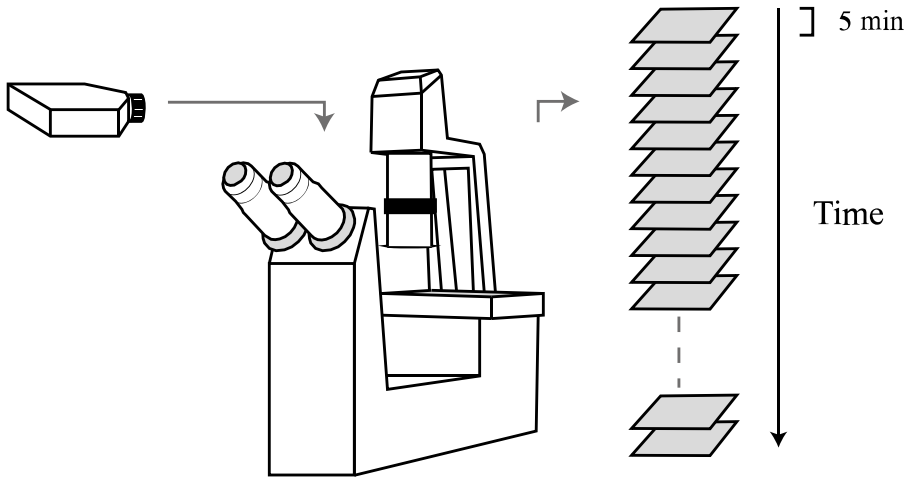

Figure A.1. A specific area in a flask was captured at 5-minute intervals, resulting in a set of time-domain micrographs for live cell imaging.

A.2 RESULTS

Individual cells were identified as described in Section 5.3.1.2. In the 18-hour observation period, some cells divided into daughter cells. The visible process of division was categorised as the progression of phases listed in Table A.1. It should be noted that these phases do not correspond to cell cycle phases; instead, the visible phases give an indication of whether a cell that presents a certain morphology is likely to divide.

Table A.1 The visible progression of phases of a dividing cell, when visualised using live cell imaging.

Phase	Exoskeleton	Halo
A	Fully adherent	None or dull
B	Partially retracted	Fully surrounding cell, brighter
C	Fully retracted into sphere	Round, brightest
D	Cytokinesis	Two spheres with surrounding halos

An example of the progression of the visible phases is shown in Figure A.2.
Using this approach, 12 different dividing cells were identified during the observation period, and the time at the start and end of each phase was noted. The mean time of the cells in each stage is shown in Figure A.3. Each cell was cropped, and representative images of the different phases are shown in Figure A.4.

A.3 DISCUSSION

Live cell imaging provided time-domain observations of proliferating ASCs, and distinct morphological phases of division were identified. The identified phases give an indication of the amount of time during which an imminently dividing cell can be distinguished from other cells. Imminently-dividing ASCs can be discerned approximately 25 minutes prior to division, and during division for approximately 15 minutes.

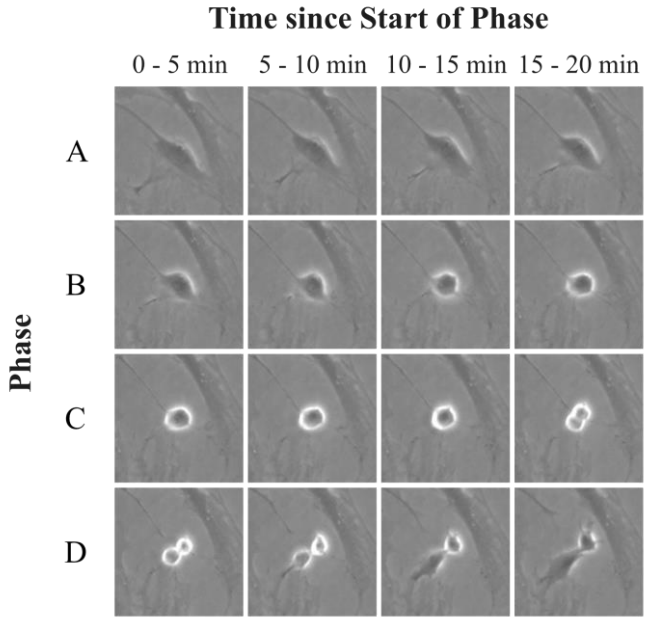

Figure A.2. A single cell is shown at 5-minute intervals, from when it is still fully adherent, until it divides and its daughter cells are both fully adherent.

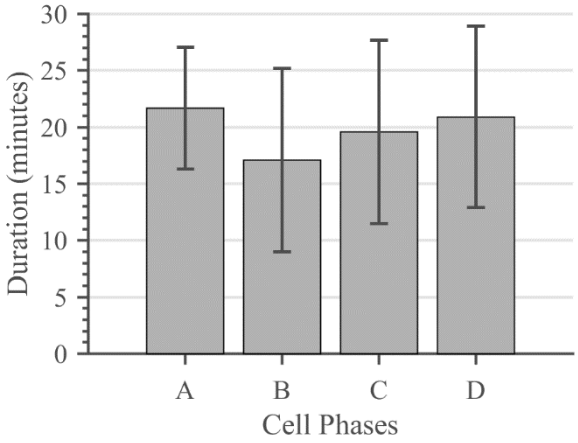

Figure A.3. The time duration in each stage of the cells that divided during the observation period. The error bars indicate the standard deviation of the sample.

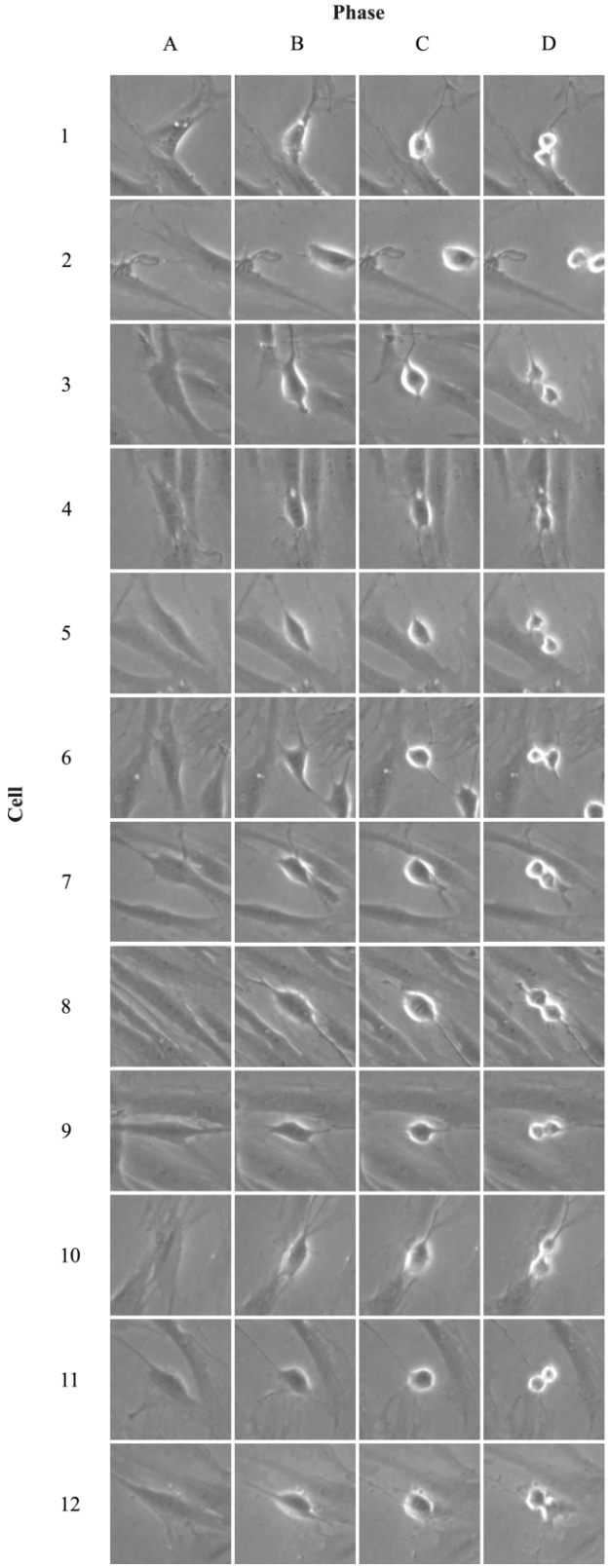

Figure A.4. Cropped images of the different visible phases of division of the 12 cells that divided during the period of observation.

ADDENDUM B INTER-PASSAGE CHARACTERISTICS

B.1 EXPERIMENTAL SETUP

SVF was isolated from the abdominal and gluteal fat of two patients, and the gluteal fat of a third patient. Each patient and extraction site are considered separately, for example A070415 A (abdominal) and A070415 G (gluteal). The SVF was plated and expanded in either FBS or pHPL at passage 0. Serial passaging was then performed: cells were expanded to 80% confluency, dissociated, and re-plated for each subsequent passage, until passage 5.

B.2 RESULTS

The SVF concentration, i.e. the number of SVF cells isolated per gram of fat, is shown in Figure B.1.

The cell yield per cm^2, and the number of days required to reach 80% confluency are shown in Figure B.2.

The cell yield per cm^2, and the days to confluency per passage, is shown in Figure B.3.

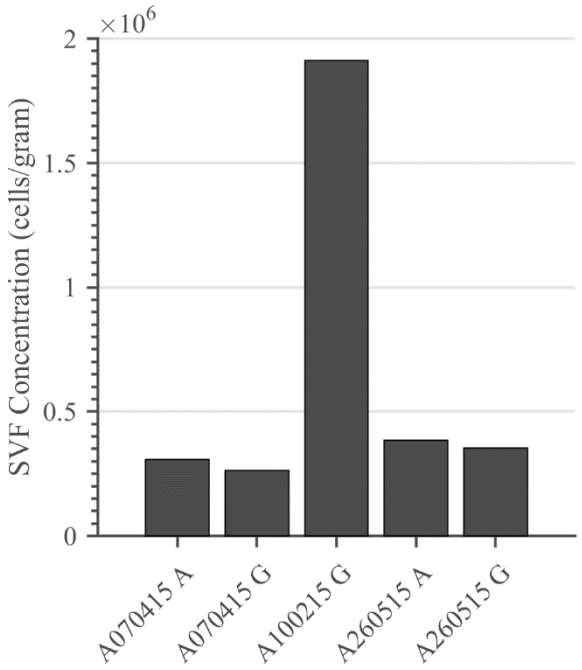

Figure B.1. The SVF concentration per gram of fat extracted from the abdominal and gluteal regions of two patients (A070415 and A260515), and the gluteal fat of a third patient (A100215).

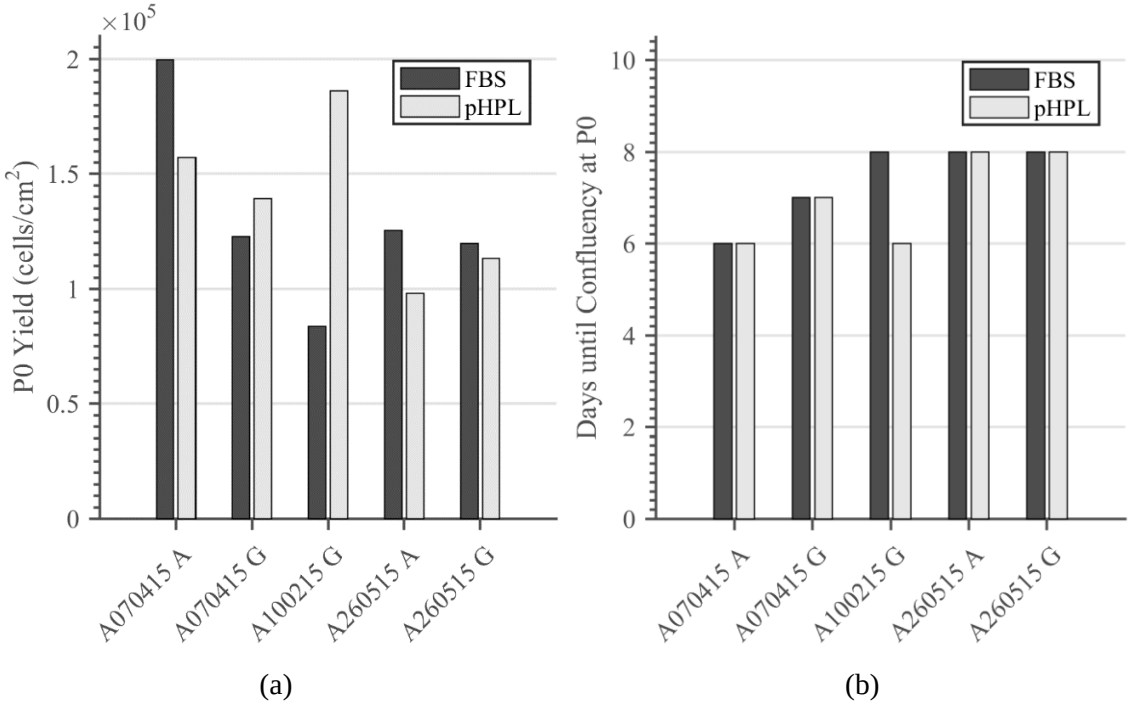

Figure B.2. Passage 0 yield (a) and days to confluency (b) for different patients and sites of extraction expanded in either FBS or pHPL.

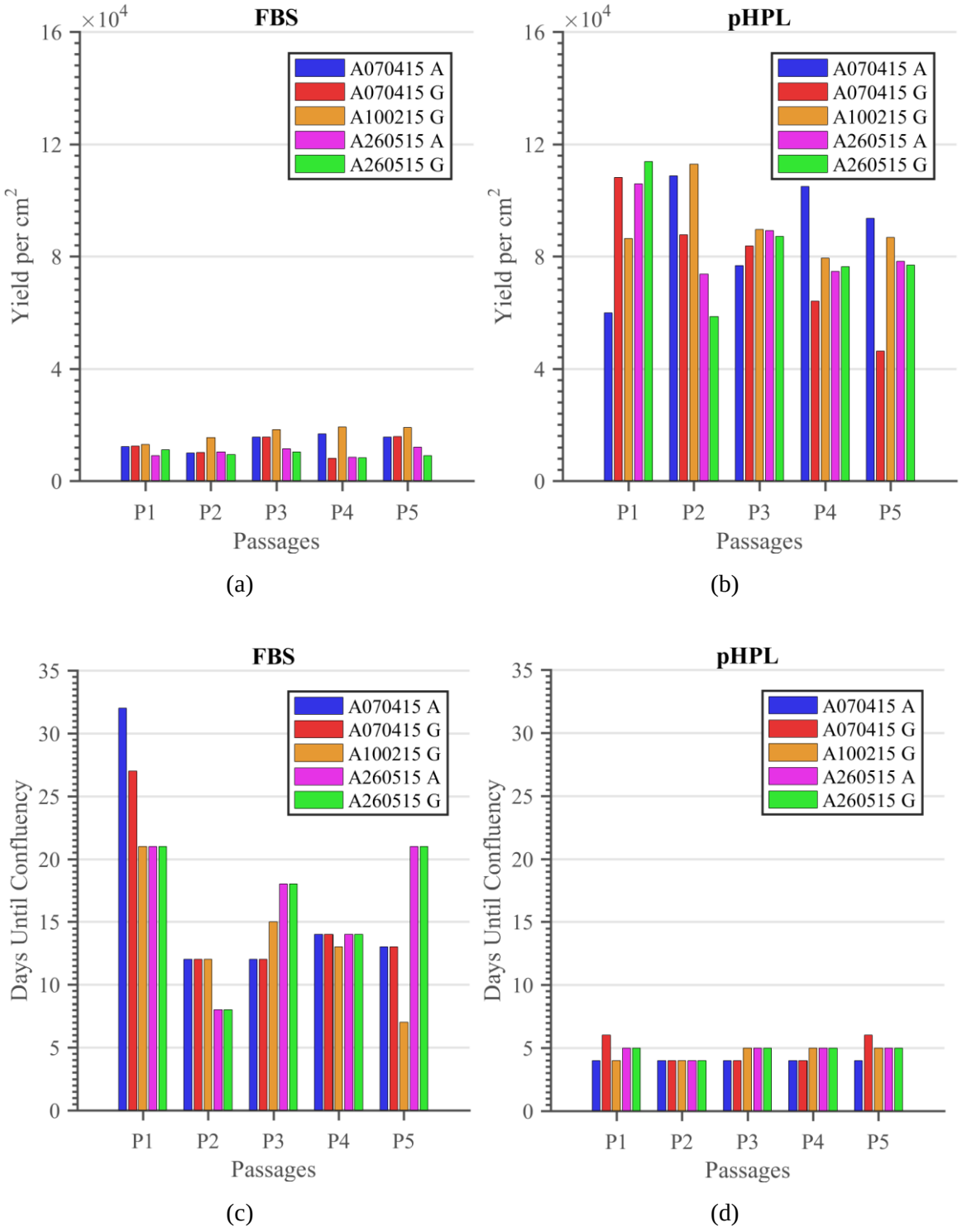

Figure B.3. The yield per cm^2 of cells expanded in FBS (a) and pHPL (b), and the number of days to reach 80% confluency for cells expanded in FBS (c) and pHPL (d), per passage.

B.3 DISCUSSION

The number of SVF cells isolated per gram of fat differed between patients. SVF at P0 is plated at a constant density, which implies that the number of flasks plated at P0 will vary between patients, based on the amount of fat extracted and the concentration of SVF.

The P0 cell yield and days to confluency were found to be similar between patients and between sera. This could be due to the high seeding density of the SVF. After seeding, P0 can reliably yield between 80000 and 200000 cells per cm^2 after 6 to 8 days.

Subsequent passages were more heterogeneous. When expanded in FBS, the number of days to reach 80% confluency differed substantially between patients, and was not consistent between passages. Although cell yield varied between patients in pHPL, the days to confluency remained consistently between 4 and 6 days. The cell yield for FBS was 4 to 6 times lower than pHPL and required a greater number of days to reach 80% confluency for every patient and passage.

ADDENDUM C POPULATION MODEL RESULTS

C.1 DESCRIPTIVE

Table C.1 The RMSE and optimised parameters for the case of descriptive evaluation.

Experiment	Model	N_0	K	DT	τ_{lag}	$\xi, t_{1/2}$	RMSE
1	VH-1	25000	112722.2	51			9955.881
1	VH-2	25000	132722.2	58			9205.223
1	VH-3	25000	132722.2	58	24		9205.223
1	VH-4	25000	132722.2	134		1, 2	9205.102
1	GL-1	25000	112722.2	54			12222.17
1	GL-2	25000	152722.2	70			9190.213
1	GL-3	25000	152722.2	70	24		9190.213
1	GL-4	25000	152722.2	87		0.9, 3	9190.392
2	VH-1	125000	339777.8	51			16224.69
2	VH-2	125000	339777.8	51			16224.69
2	VH-3	125000	339777.8	51	24		16224.69
2	VH-4	125000	339777.8	17		0.9, 5	16202.8
2	GL-1	125000	339777.8	46			18755.37
2	GL-2	125000	379777.8	57			14329.48
2	GL-3	125000	359777.8	45	39		13282.69
2	GL-4	125000	349777.8	33		0.2, 14	11975.15
3	VH-1	14950	309332	57			18942.62
3	VH-2	14950	449332	63			15549.41
3	VH-3	14950	449332	63	24		15549.41
3	VH-4	14950	469332	48		0.8, 4	15533.82
3	GL-1	14950	309332	59			22110.73
3	GL-2	14950	459332	67			15901.58
3	GL-3	14950	459332	67	24		15901.58
3	GL-4	14950	469332	105		0.7, 3	15888.81

4	VH-1	10919.77	274043.7	50			17965.6
4	VH-2	10919.77	364043.7	55			13294.58
4	VH-3	10919.77	364043.7	55	24		13294.58
4	VH-4	10919.77	364043.7	60		0.2, 4	13283.95
4	GL-1	10919.77	274043.7	51			26740.42
4	GL-2	10919.77	444043.7	59			14196.25
4	GL-3	10919.77	444043.7	59	24		14196.25
4	GL-4	10919.77	444043.7	32		0.7, 5	14196.1
5	VH-1	16414.55	135781.3	68			15108.48
5	VH-2	16414.55	135781.3	68			15108.48
5	VH-3	16414.55	135781.3	68	24		15108.48
5	VH-4	16414.55	135781.3	51		0.8, 4	15104.95
5	GL-1	16414.55	135781.3	71			13624.14
5	GL-2	16414.55	135781.3	71			13624.14
5	GL-3	16414.55	135781.3	71	24		13624.14
5	GL-4	16414.55	135781.3	111		0.7, 3	13624.15
6	VH-1	6515.451	160053.3	52			15279.67
6	VH-2	6515.451	300053.3	60			10365.83
6	VH-3	6515.451	250053.3	55	40		9974.59
6	VH-4	6515.451	220053.3	49		0.1, 35	9571.566
6	GL-1	6515.451	160053.3	56			19202.45
6	GL-2	6515.451	330053.3	64			9459.816
6	GL-3	6515.451	310053.3	60	40		9067.943
6	GL-4	6515.451	270053.3	42		0.2, 36	8751.559
7	VH-1	6652.695	96961.18	54			6915.923
7	VH-2	6652.695	106961.2	57			6657.835
7	VH-3	6652.695	106961.2	57	24		6657.835
7	VH-4	6652.695	106961.2	139		0.8, 2	6648.858
7	GL-1	6652.695	96961.18	60			7797.854
7	GL-2	6652.695	116961.2	66			6846.141
7	GL-3	6652.695	116961.2	66	24		6846.141
7	GL-4	6652.695	116961.2	27		0.8, 5	6833.642
8	VH-1	11244.62	974477	20			285618.2
8	VH-2	11244.62	697238.5	19			181366.7
8	VH-3	11244.62	697238.5	18	37		180847.8
8	VH-4	11244.62	777238.5	8		0.3, 36	173518.3
8	GL-1	11244.62	974477	22			234886.7
8	GL-2	11244.62	747238.5	19			189638.4
8	GL-3	11244.62	747238.5	18	35		189271.2
8	GL-4	11244.62	737238.5	10		0.3, 13	189221.2
9	VH-1	6256.034	704196.1	35			176903.8
9	VH-2	6256.034	472098.1	26			127317

9	VH-3	6256.034	472098.1	24	40		126783.8
9	VH-4	6256.034	472098.1	13		1, 20	126672.3
9	GL-1	6256.034	704196.1	29			139397.6
9	GL-2	6256.034	552098.1	26			126879
9	GL-3	6256.034	542098.1	24	40		115926.2
9	GL-4	6256.034	522098.1	17		0.2, 36	125398.4
10	VH-1	4624.349	2138787	18			552684.2
10	VH-2	4624.349	1519393	15			314223.4
10	VH-3	4624.349	1519393	15	28		310931.2
10	VH-4	4624.349	1569393	21		0.5, 22	282485.2
10	GL-1	4624.349	2138787	17			442923.4
10	GL-2	4624.349	1679393	15			337758.3
10	GL-3	4624.349	1659393	14	40		332451
10	GL-4	4624.349	1609393	10		0.2, 36	320486.4
11	VH-1	6004.739	1383717	17			274557.3
11	VH-2	6004.739	1091858	17			154435.5
11	VH-3	6004.739	1091858	17	26		154222.5
11	VH-4	6004.739	1091858	8		0.9, 5	154232.1
11	GL-1	6004.739	1383717	18			202100.2
11	GL-2	6004.739	1221858	17			169893.1
11	GL-3	6004.739	1201858	16	34		168126.1
11	GL-4	6004.739	1161858	11		0.2, 35	163469.3
12	VH-1	3092.233	1639455	17			292918.5
12	VH-2	3092.233	1289727	15			160130.8
12	VH-3	3092.233	1269727	15	27		154248.9
12	VH-4	3092.233	1269727	13		0.2, 9	154023.6
12	GL-1	3092.233	1639455	16			216877.3
12	GL-2	3092.233	1399727	15			142964.4
12	GL-3	3092.233	1369727	14	33		141071.8
12	GL-4	3092.233	1379727	13		0.2, 8	140988.6
13	VH-1	9500	106618.7	28			9862.997
13	VH-2	9500	106618.7	28			9862.997
13	VH-3	9500	106618.7	25	40		8518.952
13	VH-4	9500	106618.7	19		0.1, 36	7108.568
13	GL-1	9500	106618.7	29			13843.69
13	GL-2	9500	146618.7	33			9842.883
13	GL-3	9500	136618.7	28	40		8615.774
13	GL-4	9500	116618.7	20		0.1, 36	5931.125
14	VH-1	9500	92719.89	29			7438.289
14	VH-2	9500	102719.9	31			7371.227
14	VH-3	9500	92719.89	26	40		5893.583
14	VH-4	9500	92719.89	21		0.1, 33	4516.894

14	GL-1	9500	92719.89	29			12262.48
14	GL-2	9500	132719.9	34			7685.554
14	GL-3	9500	122719.9	29	40		6640.582
14	GL-4	9500	102719.9	17		0.2, 36	3953.626
15	VH-1	9500	90159.58	29			6621.397
15	VH-2	9500	90159.58	29			6621.397
15	VH-3	9500	90159.58	25	40		4598.033
15	VH-4	9500	90159.58	21		0.1, 31	1745.726
15	GL-1	9500	90159.58	29			11535.67
15	GL-2	9500	120159.6	33			6747.392
15	GL-3	9500	120159.6	29	40		5483.945
15	GL-4	9500	100159.6	17		0.2, 36	2647.787

C.2 PREDICTIVE

Table C.2 The RMSE and optimised parameters of the Verhulst model VH-2, for the case of predictive evaluation.

	Model	**Number of measurements**	***K***	***DT***	**RMSE**
1	VH-2	1	500000	25	303058.7
1	VH-2	2	50000	16	37512.92
1	VH-2	3	50000	17	37508.98
1	VH-2	4	50000	17	37508.98
1	VH-2	5	200000	63	16484.04
1	VH-2	6	90000	47	15895.27
1	VH-2	7	140000	60	9292.111
1	VH-2	8	150000	61	9765.082
1	VH-2	9	140000	60	9292.111
1	VH-2	10	130000	57	9201.899
2	VH-2	1	230000	122	108674.4
2	VH-2	2	2000000	73	239773.6
2	VH-2	3	1970000	69	276217.2
2	VH-2	4	330000	45	15996.95
2	VH-2	5	340000	46	18434.31
2	VH-2	6	300000	40	19237.67
2	VH-2	7	300000	40	19237.67
2	VH-2	8	300000	40	19237.67
2	VH-2	9	320000	45	15112.96
2	VH-2	10	320000	45	15112.96
3	VH-2	1	20000	155	133241.9
3	VH-2	2	2000000	94	65597.71

3	VH-2	3	2000000	50	281163.6
3	VH-2	4	1780000	48	315271.3
3	VH-2	5	110000	41	72804.79
3	VH-2	6	350000	49	46707.74
3	VH-2	7	120000	40	67302.25
3	VH-2	8	130000	41	62369.75
3	VH-2	9	120000	40	67302.25
3	VH-2	10	150000	45	53795.73
3	VH-2	11	240000	54	28196.5
3	VH-2	12	270000	56	23625.8
3	VH-2	13	290000	57	21218.56
3	VH-2	14	450000	63	15547.47
4	VH-2	1	10000	155	134641.1
4	VH-2	2	2000000	91	78059.38
4	VH-2	3	2000000	79	54798.64
4	VH-2	4	2000000	44	366808.8
4	VH-2	5	210000	45	30832.02
4	VH-2	6	80000	38	87883.33
4	VH-2	7	90000	40	82260.41
4	VH-2	8	100000	42	76980.18
4	VH-2	9	110000	44	72115.34
4	VH-2	10	1430000	61	39414.59
4	VH-2	11	2000000	61	47563.6
4	VH-2	12	400000	56	13612.87
4	VH-2	13	400000	56	13612.87
4	VH-2	14	360000	55	13323.95
5	VH-2	1	20000	155	59560.23
5	VH-2	2	90000	155	45097.73
5	VH-2	3	2000000	97	28017.98
5	VH-2	4	2000000	90	38115.95
5	VH-2	5	2000000	66	141623
5	VH-2	6	2000000	69	118937.6
5	VH-2	7	180000	61	30009.71
5	VH-2	8	100000	51	13277.92
5	VH-2	9	90000	49	14880.16
5	VH-2	10	110000	55	13238.86
5	VH-2	11	100000	52	13299.18
5	VH-2	12	100000	52	13299.18
5	VH-2	13	120000	59	13941.51
5	VH-2	14	110000	56	13207.27
6	VH-2	1	10000	155	75932.87
6	VH-2	2	2000000	38	505858.5

6	VH-2	3	20000	33	68234.4
6	VH-2	4	20000	31	68228.17
6	VH-2	5	30000	42	62072.08
6	VH-2	6	180000	59	17830.41
6	VH-2	7	880000	62	21130.84
6	VH-2	8	50000	48	51289.51
6	VH-2	9	70000	53	43029.88
6	VH-2	10	460000	67	14775.38
6	VH-2	11	2000000	66	15173.6
6	VH-2	12	2000000	64	21143.56
6	VH-2	13	710000	64	13148.7
6	VH-2	14	300000	60	10365.65
7	VH-2	1	10000	155	48438.87
7	VH-2	2	2000000	32	870644.2
7	VH-2	3	20000	22	39544.47
7	VH-2	4	30000	30	32527.81
7	VH-2	5	30000	30	32527.81
7	VH-2	6	50000	39	20697.62
7	VH-2	7	40000	35	26242.68
7	VH-2	8	40000	35	26242.68
7	VH-2	9	50000	42	20824.36
7	VH-2	10	60000	46	16214.77
7	VH-2	11	210000	64	13593.5
7	VH-2	12	110000	57	6683.49
7	VH-2	13	100000	55	6772.502
7	VH-2	14	110000	57	6683.49
8	VH-2	1	10000	155	599390.7
8	VH-2	2	2000000	27	829923.5
8	VH-2	3	2000000	18	1049503
8	VH-2	4	360000	17	327751.1
8	VH-2	5	400000	17	301745.7
8	VH-2	6	1410000	21	573628.5
8	VH-2	7	850000	20	219879.4
8	VH-2	8	750000	19	186956.7
8	VH-2	9	650000	19	184710.8
8	VH-2	10	680000	19	181667.3
8	VH-2	11	710000	19	181829.4
8	VH-2	12	710000	19	181829.4
8	VH-2	13	740000	19	185166.9
8	VH-2	14	690000	19	181363.2
9	VH-2	1	10000	155	361236.3
9	VH-2	2	2000000	51	229032.2

9	VH-2	3	2000000	27	867608.9
9	VH-2	4	90000	25	301535.3
9	VH-2	5	1010000	27	351212.3
9	VH-2	6	130000	23	273889.7
9	VH-2	7	2000000	28	824312.9
9	VH-2	8	480000	26	127417
9	VH-2	9	480000	26	127417
9	VH-2	10	650000	28	166732.5
9	VH-2	11	460000	26	127593.5
9	VH-2	12	410000	25	133698.6
9	VH-2	13	460000	26	127593.5
9	VH-2	14	470000	26	127327.6
10	VH-2	1	10000	155	1275219
10	VH-2	2	2000000	26	692717.7
10	VH-2	3	2000000	21	539767.3
10	VH-2	4	780000	17	683208.2
10	VH-2	5	980000	16	534712.1
10	VH-2	6	2000000	16	526028.3
10	VH-2	7	1290000	15	364592.3
10	VH-2	8	1480000	15	315754.6
10	VH-2	9	1490000	15	315061.4
10	VH-2	10	1490000	15	315061.4
10	VH-2	11	1620000	15	324796
10	VH-2	12	1600000	15	321082.3
10	VH-2	13	1570000	15	316983
10	VH-2	14	1520000	15	314225
11	VH-2	1	10000	155	898256.1
11	VH-2	2	2000000	21	674389.5
11	VH-2	3	2000000	17	716545.3
11	VH-2	4	2000000	17	716545.3
11	VH-2	5	550000	16	461087.6
11	VH-2	6	1950000	18	666463.6
11	VH-2	7	1220000	17	183539.3
11	VH-2	8	1150000	17	160624
11	VH-2	9	1070000	17	155583.3
11	VH-2	10	1040000	17	160215.3
11	VH-2	11	1000000	17	171409
11	VH-2	12	1020000	17	165144.5
11	VH-2	13	1070000	17	155583.3
11	VH-2	14	1090000	17	154458.3
12	VH-2	1	10000	155	1038101
12	VH-2	2	250000	17	836950.5

12	VH-2	3	2000000	15	583815.6
12	VH-2	4	450000	14	706855
12	VH-2	5	490000	14	677087.7
12	VH-2	6	910000	15	343868.1
12	VH-2	7	1180000	16	181746.8
12	VH-2	8	1440000	17	188740.3
12	VH-2	9	1270000	15	160780.1
12	VH-2	10	1250000	15	163133.5
12	VH-2	11	1210000	15	172583.5
12	VH-2	12	1220000	15	169669.1
12	VH-2	13	1290000	15	160133.7
12	VH-2	14	1290000	15	160133.7
13	VH-2	1	860000	96	51075.61
13	VH-2	2	2000000	68	41227.59
13	VH-2	3	2000000	44	18989.22
13	VH-2	4	2000000	36	49528.03
13	VH-2	5	2000000	35	58200.11
13	VH-2	6	110000	29	9817.307
13	VH-2	7	110000	29	9817.307
14	VH-2	1	750000	60	27571.51
14	VH-2	2	20000	36	46581.04
14	VH-2	3	2000000	46	15227.15
14	VH-2	4	2000000	38	41027.89
14	VH-2	5	2000000	38	41027.89
14	VH-2	6	100000	31	7263.011
14	VH-2	7	100000	31	7263.011
15	VH-2	1	830000	66	32239.26
15	VH-2	2	1090000	61	28592.86
15	VH-2	3	2000000	43	21050.17
15	VH-2	4	2000000	37	48756.2
15	VH-2	5	720000	37	39739.23
15	VH-2	6	110000	31	8231.821
15	VH-2	7	90000	29	6644.445

Table C.3 The RMSE and optimised parameters of the generalised logistic model GL-2, for the case of predictive evaluation.

Experiment	Model	Number of measurements	K	DT	RMSE
1	GL-2	1	2000000	26	1171781
1	GL-2	2	60000	22	31936.27
1	GL-2	3	40000	18	42331.18

1	GL-2	4	50000	20	38150.17
1	GL-2	5	180000	70	12830.72
1	GL-2	6	100000	58	17542.7
1	GL-2	7	150000	70	9167.335
1	GL-2	8	170000	73	9513.355
1	GL-2	9	160000	71	9287.011
1	GL-2	10	150000	69	9181.799
2	GL-2	1	210000	143	115715.5
2	GL-2	2	2000000	78	271175.3
2	GL-2	3	2000000	74	283646.2
2	GL-2	4	470000	65	33703.39
2	GL-2	5	460000	65	31113.75
2	GL-2	6	370000	55	14460.18
2	GL-2	7	370000	55	14607.88
2	GL-2	8	360000	53	15627
2	GL-2	9	380000	57	14351.97
2	GL-2	10	380000	58	14334.38
3	GL-2	1	10000	6	135747.4
3	GL-2	2	2000000	95	63680.14
3	GL-2	3	2000000	50	242678.3
3	GL-2	4	2000000	49	393600.2
3	GL-2	5	120000	45	72334.2
3	GL-2	6	870000	53	151811.8
3	GL-2	7	140000	45	64267.35
3	GL-2	8	150000	46	60711.72
3	GL-2	9	140000	45	63396.44
3	GL-2	10	170000	49	52780.17
3	GL-2	11	240000	57	33702.68
3	GL-2	12	300000	61	25716.07
3	GL-2	13	340000	63	21037.53
3	GL-2	14	460000	67	15899.86
4	GL-2	1	10000	6	134131.5
4	GL-2	2	2000000	92	77234.35
4	GL-2	3	2000000	80	53493.72
4	GL-2	4	2000000	45	426578.1
4	GL-2	5	130000	47	65418.16
4	GL-2	6	80000	43	91263.56
4	GL-2	7	100000	46	82550.1
4	GL-2	8	110000	48	77309.18
4	GL-2	9	130000	51	73491.7
4	GL-2	10	1970000	62	45406.98
4	GL-2	11	2000000	62	48321.25

4	GL-2	12	450000	59	15498.57
4	GL-2	13	450000	59	14372.73
4	GL-2	14	440000	59	14213.62
5	GL-2	1	10000	6	61448.69
5	GL-2	2	50000	155	48084.97
5	GL-2	3	2000000	98	29917.42
5	GL-2	4	2000000	91	41119.8
5	GL-2	5	2000000	67	158129.3
5	GL-2	6	580000	69	96693.46
5	GL-2	7	150000	66	17782.83
5	GL-2	8	120000	63	13083.54
5	GL-2	9	100000	58	15241.48
5	GL-2	10	130000	66	13543.78
5	GL-2	11	120000	64	12989.08
5	GL-2	12	110000	60	13363.43
5	GL-2	13	140000	70	14170.91
5	GL-2	14	120000	64	12946.37
6	GL-2	1	10000	155	75946.82
6	GL-2	2	2000000	38	655507.9
6	GL-2	3	20000	39	68709.83
6	GL-2	4	20000	37	68648.19
6	GL-2	5	30000	50	63165.44
6	GL-2	6	120000	62	27273.78
6	GL-2	7	2000000	63	30861.89
6	GL-2	8	50000	54	53081.4
6	GL-2	9	70000	60	45731.36
6	GL-2	10	290000	69	14057.96
6	GL-2	11	2000000	67	15233.65
6	GL-2	12	2000000	65	22100.76
6	GL-2	13	480000	65	10424.8
6	GL-2	14	330000	64	9459.937
7	GL-2	1	10000	155	48454.99
7	GL-2	2	2000000	32	932981.9
7	GL-2	3	30000	34	33255.62
7	GL-2	4	30000	34	33226.91
7	GL-2	5	30000	34	33416
7	GL-2	6	60000	48	18037.86
7	GL-2	7	40000	39	27404.57
7	GL-2	8	50000	47	22600.44
7	GL-2	9	50000	45	22422.73
7	GL-2	10	70000	56	14550.84
7	GL-2	11	240000	70	17606.63

7	GL-2	12	110000	64	6886.122
7	GL-2	13	110000	64	6969.453
7	GL-2	14	110000	64	6860.15
8	GL-2	1	10000	6	598683.1
8	GL-2	2	2000000	27	861810.9
8	GL-2	3	2000000	18	1038262
8	GL-2	4	390000	18	315565
8	GL-2	5	520000	19	248221.1
8	GL-2	6	1560000	21	560529.1
8	GL-2	7	1050000	20	273567.7
8	GL-2	8	900000	20	212701.2
8	GL-2	9	720000	19	190811.2
8	GL-2	10	750000	19	189631.2
8	GL-2	11	780000	19	190871.1
8	GL-2	12	780000	19	190871.1
8	GL-2	13	830000	20	196310.9
8	GL-2	14	750000	19	189631.2
9	GL-2	1	10000	155	361177.4
9	GL-2	2	2000000	51	222774.3
9	GL-2	3	2000000	27	893088.8
9	GL-2	4	160000	27	276596.1
9	GL-2	5	720000	27	181053
9	GL-2	6	160000	24	262644.3
9	GL-2	7	2000000	28	769859.6
9	GL-2	8	640000	27	132309.6
9	GL-2	9	650000	27	133764
9	GL-2	10	950000	29	201249
9	GL-2	11	550000	26	126885.6
9	GL-2	12	460000	25	134786.5
9	GL-2	13	550000	26	126885.6
9	GL-2	14	550000	26	126885.6
10	GL-2	1	10000	155	1274793
10	GL-2	2	2000000	26	650144.1
10	GL-2	3	2000000	21	492051
10	GL-2	4	1330000	17	473944.3
10	GL-2	5	1480000	16	370993.4
10	GL-2	6	2000000	15	405532.1
10	GL-2	7	1510000	15	358263.6
10	GL-2	8	1900000	15	371511.1
10	GL-2	9	1760000	15	342489.4
10	GL-2	10	1760000	15	342489.4
10	GL-2	11	1860000	15	360766.1

10	GL-2	12	1830000	15	353936.8
10	GL-2	13	1750000	15	341397.1
10	GL-2	14	1680000	15	337758.7
11	GL-2	1	10000	155	898126
11	GL-2	2	2000000	21	653326
11	GL-2	3	1670000	17	422832.1
11	GL-2	4	2000000	17	634777.6
11	GL-2	5	740000	17	342848.9
11	GL-2	6	2000000	18	513608.6
11	GL-2	7	1880000	18	444009.3
11	GL-2	8	1390000	17	205597.7
11	GL-2	9	1260000	17	172198.1
11	GL-2	10	1180000	17	171863.1
11	GL-2	11	1070000	16	192479.2
11	GL-2	12	1140000	17	178029.5
11	GL-2	13	1200000	17	170334.1
11	GL-2	14	1220000	17	169880.3
12	GL-2	1	10000	155	1037402
12	GL-2	2	170000	17	904239
12	GL-2	3	1150000	15	198368.8
12	GL-2	4	330000	14	775163.3
12	GL-2	5	1960000	15	291837.1
12	GL-2	6	1480000	15	154339.6
12	GL-2	7	1480000	15	154339.6
12	GL-2	8	1580000	15	192294
12	GL-2	9	1500000	15	160189.8
12	GL-2	10	1420000	15	143827.4
12	GL-2	11	1310000	14	150843.6
12	GL-2	12	1320000	14	149215.7
12	GL-2	13	1420000	15	143827.4
12	GL-2	14	1400000	15	142966.5
13	GL-2	1	2000000	97	50960.52
13	GL-2	2	190000	68	41095.48
13	GL-2	3	2000000	44	19485.43
13	GL-2	4	2000000	37	46022.7
13	GL-2	5	2000000	35	61970.76
13	GL-2	6	140000	32	9767.264
13	GL-2	7	140000	32	9762.647
14	GL-2	1	40000	58	38166.12
14	GL-2	2	20000	45	47345.04
14	GL-2	3	2000000	46	15831.46
14	GL-2	4	2000000	39	37522.16

14	GL-2	5	2000000	38	42734.77
14	GL-2	6	150000	35	8654.509
14	GL-2	7	130000	34	7657.255
15	GL-2	1	50000	65	37330.87
15	GL-2	2	2000000	62	28584.11
15	GL-2	3	2000000	43	22947.49
15	GL-2	4	2000000	37	52936.28
15	GL-2	5	1110000	38	41939.6
15	GL-2	6	160000	35	8987.056
15	GL-2	7	120000	33	6753.678